



UNIVERSIDAD DE CONCEPCIÓN

DIRECCIÓN DE POSTGRADO

FACULTAD DE INGENIERÍA – PROGRAMA DE DOCTORADO EN CIENCIAS DE
LA INGENIERÍA CON MENCIÓN EN INGENIERÍA ELÉCTRICA

Submersible Permanent-Magnet Synchronous Machine with a Stainless Core and Unequal Teeth Widths

(Máquina Síncrona de Imán Permanente Sumergible
con Núcleo de Acero Inoxidable y Anchos de
Dientes Desiguales)

Tesis para optar al grado de Doctor en Ciencias de la Ingeniería con
mención en Ingeniería Eléctrica

The thesis was written under a double doctoral degree agreement between Lappeenranta–
Lahti University of Technology LUT, Finland and University of Concepción, Chile and
jointly supervised by supervisors from both universities.

ALVARO ERNESTO HOFFER GARCÉS
CONCEPCIÓN–CHILE
2021

- Supervisors Professor Juha Pyrhönen
LUT School of Energy Systems
Lappeenranta–Lahti University of Technology LUT
Finland
- Professor Juan Tapia Ladino
Department of Electrical Engineering
University of Concepción
Chile
- Reviewers Professor Ayman EL-Refai
Department of Electrical and Computer Engineering
Marquette University
the United States of America
- Associate Professor Michele Degano
Department of Electrical and Electronic Engineering
University of Nottingham
the United Kingdom
- Opponents Professor Ayman EL-Refai
Department of Electrical and Computer Engineering
Marquette University
the United States of America
- Associate Professor Michele Degano
Department of Electrical and Electronic Engineering
University of Nottingham
the United Kingdom

Abstract

Alvaro Ernesto Hoffer Garcés

Submersible Permanent-Magnet Synchronous Machine with a Stainless Core and Unequal Teeth Widths

In recent years, permanent magnet synchronous machines (PMSM) have gained popularity owing to their excellent performance compared with other kinds of electrical machines in numerous applications. Furthermore, advances in power electronics, digital signal processing, control schemes, and the development of electrical materials have contributed to the rapid development of PMSMs. Nowadays, designers of electrical machines investigate the PMSM to improve its performance and reliability by reducing the amount of materials while minimizing its cost. In this doctoral dissertation, a study is presented to improve the performance of a PMSM using asymmetric characteristics. The study aims to employ unequal teeth widths without changing the size of the machine to increase the winding factor and thus be able to increase the value of the induced voltage and the electromagnetic torque. The exploitation of this asymmetry is possible because of the tooth-coil winding (TCW), which has multiple advantages from both the electromagnetic and the manufacturing point of view.

A submersible application consists of a scenario where the devices are operated in underwater environments, such as harvesting marine energy or a water pumping system. These applications require an electrical machine to be corrosion resistant, which makes its design and manufacture challenging. Currently, there are various submersible machines. The best known is the canned PMSM, whose stator and rotor are protected with cans, and whose active parts are made of traditional electrical materials, enabling water to flow through the air gap. However, a completely encapsulated traditional stator is a complex structure and has low heat transfer characteristics. In this doctoral dissertation, a stainless core submersible PMSM is presented as an alternative to the conventional submersible machine. The machine under study consists of a fully stainless stator, and a rotor-surface permanent magnet rotor, protected by a fiberglass cover. Ferritic stainless steel is used as stator core material, and the winding is made of polyvinyl chloride (PVC) insulated solid-conductor wire.

To test the asymmetric characteristic of the stator and verify the functionality of the proposed submersible machine, a 1.7 kW, 80 r/min, 24-slot 20-pole fully submersible PMSM was simulated, constructed, and verified in a water tank and in a lake with fresh water. The analytical and the finite element method (FEM) results showed that it was possible to improve the machine performance by employing unequal teeth. This improvement was reflected in an 8% increase in the value of the induced voltage compared with the symmetric machine. However, the use of ferritic stainless steel showed that the stator core losses correspond to 40% of the total losses of the machine, indicating that the efficiency was 74% at the rated load. Despite this, the machine turned

out to be functional.

Keywords: Analytical analysis, asymmetrical stator, canned machine, finite element analysis, hysteresis torque, permanent magnet, permanent magnet machine, submersible machine, tooth-coil winding



Resumen

Alvaro Ernesto Hoffer Garcés

Máquina Síncrona de Imán Permanente Sumergible con Núcleo de Acero Inoxidable y Anchos de Dientes Desiguales

En los últimos años, las máquinas síncronas de imanes permanentes (MSIP) han ganado popularidad debido a su excelente rendimiento en comparación con otros tipos de máquinas eléctricas en numerosas aplicaciones. Además, los avances en la electrónica de potencia, el procesamiento de señales digitales, los esquemas de control y el desarrollo de materiales eléctricos han contribuido al rápido desarrollo de las MSIP. Hoy en día, los diseñadores de máquinas eléctricas investigan la MSIP para mejorar su rendimiento y confiabilidad al reducir la cantidad de materiales y minimizar su costo. En esta tesis doctoral se presenta un estudio para mejorar el desempeño de una MSIP utilizando características asimétricas. El estudio tiene como objetivo emplear anchos de dientes desiguales sin cambiar el tamaño de la máquina para aumentar el factor de bobinado y así poder aumentar el valor de la tensión inducida y el torque electromagnético. La explotación de esta asimetría es posible gracias al devanado concentrado que tiene múltiples ventajas tanto desde el punto de vista electromagnético como de fabricación.

Una aplicación sumergible consiste en un escenario en el que los dispositivos funcionan en entornos subacuáticos, como la recolección de energía marina o un sistema de bombeo de agua. Estas aplicaciones requieren que la máquina eléctrica sea resistente a la corrosión, lo que dificulta su diseño y fabricación. Actualmente, existen varias máquinas sumergibles. La más conocida es la MSIP encapsulada, cuyo estator y rotor están protegidos con cubiertas, y cuyas partes activas están fabricadas con materiales eléctricos tradicionales, lo que permite que el agua fluya a través del entrehierro. Sin embargo, un estator tradicional completamente encapsulado es una estructura compleja y tiene características de baja transferencia de calor. En esta tesis doctoral se presenta una MSIP sumergible de núcleo inoxidable como alternativa a la máquina sumergible convencional. La máquina en estudio consta de un estator totalmente inoxidable y un rotor con imanes permanentes montados en su superficie, protegido por una cubierta de fibra de vidrio. El acero inoxidable ferrítico se utiliza como material del núcleo del estator y el devanado está hecho de alambre conductor sólido aislado con cloruro de polivinilo (PVC).

Para probar la característica asimétrica del estator y verificar la funcionalidad de la máquina sumergible propuesta, se simuló, construyó, y verificó una MSIP completamente sumergible de 1.7 kW, 80 r/min, 24 ranuras y 20 polos en un tanque de agua y en un lago de agua dulce. Los resultados analíticos y del método de elementos finitos (MEF) mostraron que era posible mejorar el rendimiento de la máquina empleando dientes desiguales. Esta mejora se reflejó en un aumento del 8% en el valor de la tensión inducida en comparación con la máquina simétrica. Sin embargo, el uso de

acero inoxidable ferrítico mostró que las pérdidas del núcleo del estator corresponden al 40% de las pérdidas totales de la máquina, lo que indica que la eficiencia fue del 74% a carga nominal. A pesar de esto, la máquina resultó ser funcional.

Palabras clave: Análisis analítico, estator asimétrico, máquina encapsulada, análisis por elementos finitos, torque de histéresis, imán permanente, máquina de imán permanente, máquina sumergible, devanado concentrado



Acknowledgments

This work was carried out at the Department of Electrical Engineering, University of Concepción, Chile, between 2016 and 2019 and at the Department of Electrical Engineering, Lappeenranta–Lahti University of Technology LUT, Finland, between 2020 and 2021. The research was founded by the Agencia Nacional de Investigación y Desarrollo (ANID) through the project FONDECYT Regular 1201667 and through the scholarship 2016-21161485, the Lappeenranta–Lahti University of Technology LUT, and the University of Concepción through the internationalization project.

I would like to express my gratitude to my supervisors Professor Juan Tapia and Professor Juha Pyrhönen for their support, patience, and guidance during this research. I would also like to thank my unofficial supervisor Dr. Ilya Petrov for his advice and willingness to resolve my doubts and concerns at critical moments during this research. I am honored to have been able to meet you and work with you.

I thank my honored pre-examiners and opponents Professor Ayman EL-Refaie and Associate Professor Michele Degano for their valuable comments and suggestions on this dissertation.

I want to thank the members of the Laboratory of Electrical Drives Technology at LUT: Minhaj Zaheer, Valerii Abramenko, and Dr. Chong Di for the stimulating discussions and for all the fun we have had in the last few years. My special thanks to Associate Professor Pia Lindh for her support during my doctoral studies at LUT.

I want to express my gratitude to Associate Professor Hanna Niemelä for the English language review of my publications and this dissertation.

I want to thank everyone I have met at LUT, especially to Natalia Araya and Óscar Marín for making this stay very enjoyable.

My sincere thanks to my former professors at the Universidad de La Frontera, Chile, Dr. Roberto Moncada, Dr. Cristián Pesce, Dr. Millaray Curilem, Dr. Héctor Young, Nelson Aros, and Manuel Villarroel for motivating me to start my doctoral studies.

I would like to extend my gratitude to Marcela Hernández for her timely support in administrative matters at the University of Concepción.

I would like to express my sincere thanks to my friends and colleagues that I have met at the Laboratory of Electrical Machine Testing of the University of Concepción: Nicolás Reyes, Mario Tapia, Pablo Araya, Erwin Cortés, and Matías Jiménez for making this work more bearable and enjoyable. I also would like to express my special thanks to Dr. Werner Jara for his advice and help during my doctoral studies.

I want to thank my friends Sergio, Jaime, Gustavo, Mauricio, Abraham, Diego, Vanessa, and Karen for their encouragement and support throughout this journey.

I sincerely and genuinely thank my dear parents Ana María and Juan, and my sister Paula for their unconditional support in this challenge.

Finally, I would like to thank God, my good Father, for letting me through all the difficulties and never leaving me.



Alvaro Ernesto Hoffer Garcés
June 2021
Lappeenranta, Finland

Contents

Abstract	v
Resumen	vii
Acknowledgments	ix
List of publications	xi
List of Figures	xii
List of Tables	xv
Nomenclature	xvi
1 Introduction	1
1.1 Tidal energy	2
1.2 Water pumping system	4
1.3 Brief discussion of applications	5
1.4 Submersible machines	5
1.5 Device materials for a submersible machine	6
1.5.1 Stainless steel materials	6
1.5.2 Cover materials	8
1.5.3 Permanent magnet materials	9
1.5.4 Winding materials	10
1.6 Tooth-coil winding	11
1.7 Asymmetric features in the PMSM	12
1.8 Discussion	14
1.9 Overview of the submersible PMSM under study	14
1.10 Outline of the doctoral dissertation	18
1.11 Scientific contributions	20
1.12 Engineering contribution	20
2 Tooth-coil winding with unequal teeth widths	21
2.1 Introduction	21
2.2 Unequal teeth widths in the TCW	22
2.3 Permeance distribution in the air gap	24
2.4 Permanent magnet magnetic field	32
2.5 Induced voltage	36
2.6 Armature reaction field	42
2.7 Current linkage and inductance analysis	47
2.8 Torque analysis	53
2.9 Summary	55

3	Loss analysis	57
3.1	Winding Joule losses	57
3.2	Stator core losses	58
3.3	Rotor losses	61
3.4	Machine performance	62
3.5	Summary	66
4	Prototype and measurements	67
4.1	Prototype manufacture description	67
4.2	Description of the test bench	69
4.3	Prototype measurements	70
4.4	Summary	72
5	Conclusion	73
	References	75



List of publications

This doctoral dissertation is based on the following papers. The rights have been granted by publishers to include the material in the dissertation.

- I. A. E. Hoffer, J. A. Tapia, I. Petrov, and J. Pyrhönen, “Design of a Stainless Core Submersible Permanent Magnet Generator for Tidal Energy,” in *IECON 2019 - 45th Annual Conference of the IEEE Industrial Electronics Society*, Lisbon, Portugal, Oct. 14–17, 2019, pp. 1010–1015.
- II. A. E. Hoffer, I. Petrov, J. J. Pyrhönen, J. A. Tapia, and G. Bramerdorfer, “Analysis of a Tooth-Coil Winding Permanent-Magnet Synchronous Machine With an Unequal Teeth Width,” *IEEE Access*, vol. 8, pp. 71512–71524.
- III. I. Petrov, A. E. Hoffer, and J. Pyrhönen, “Reduction of torque ripple in synchronous machines by quasi-skew-asymmetric rotor,” in *2020 International Conference on Electrical Machines (ICEM)*, Gothenburg, Sweden, Aug. 23–26, 2020, pp. 298–304.
- IV. A. E. Hoffer, I. Petrov, J. J. Pyrhönen, and J. A. Tapia, “Stainless-Core Submersible Permanent Magnet Synchronous Machine,” *IEEE Access*, vol. 9, pp. 28089–28100.

Author’s contribution

Alvaro Hoffer is the principal author and investigator in **Publications I, II, and IV**. Dr. Petrov conducted the experimental measurements presented in **Publications II and IV**. In **Publication I**, the author of this doctoral dissertation proposed a straightforward electromagnetic design of a permanent magnet machine for tidal energy harvesting. In **Publication II**, the author analyzed the machine shown in **Publication I**. This analysis evaluated the main parameters (flux density, induced voltage, electromagnetic torque, and briefly the losses) of the permanent magnet machine by using analytical and finite element methods when considering the stator asymmetric. In **Publication III**, Dr. Petrov was the corresponding author, and Alvaro Hoffer participated in the research and writing processes by presenting a novel alternative for reducing cogging torque by using a quasi-skew asymmetric rotor structure. **Publication IV** is a continuation of the investigation of **Publication II**, where the machine losses were analyzed in depth.

List of Figures

1.1	Configuration of the direct-driven PMSG tidal energy conversion system. The electrical power is defined by $P_{\text{elec}} = \eta_g P_{\text{mech}}$, where η_g is the generator efficiency.	3
1.2	Schematic diagram of a water pumping system. The mechanical power is defined by $P_{\text{mech}} = \eta_m P_{\text{elec}}$, where η_m is the motor efficiency.	4
1.3	Magnetization curves of traditional electrical steels used in the manufacture of electrical machines and stainless steels.	7
1.4	Cover arrangement alternatives in a rotor surface PMSM: (a) canned machine, (b) canned rotor, and (c) canned stator.	9
1.5	Possible wires for use in submersible environments: (a) standard enameled wire, (b) enameled wire encapsulated with a protective material, and (c) wire with proper protection.	10
1.6	Examples of the step skewing: (a) three-step skewing of the 12 pole rotor with the skew angle of 1.67° between the layers and (b) quasi-three-step skewing of the 12 pole rotor with the quasi-skew angle of 1.67°	13
1.7	Cross-sectional view of the submersible core PMSM.	15
2.1	Stator slot geometry and teeth reluctances: (a) trapezoidal and (b) rectangular slot.	22
2.2	Flux density distributions under no-load condition when using (a) trapezoidal and (b) rectangular slot.	23
2.3	Adjustment procedure of the stator tooth inner width b_{ds}	23
2.4	Simplified geometry of the machine used to obtain the permeance distribution.	26
2.5	Permeance distribution in the air gap of the symmetric stator at different slot opening widths: (a) $b_0 = 4$ mm, (b) $b_0 = 8$ mm, and (c) $b_0 = 12$ mm.	29
2.6	Sequence of the estimation of the permeance distribution in the air gap of a TCW PMSM with unequal teeth widths. The angle $\iota = 2\pi / (Q_s/2) - W$ corresponds to the angular displacement between two neighboring slots that carry different phase coils.	30
2.7	Diagram to obtain the permeance distribution in the air gap of a TCW PMSM with unequal teeth widths.	31
2.8	Permeance distribution in the air gap at different stator tooth inner widths: (a) $b_{\text{ds}} = b_{\text{ds}1}$, (b) $b_{\text{ds}} = 19$ mm, (c) $b_{\text{ds}} = 23$ mm, (d) $b_{\text{ds}} = 28$ mm, and (e) their spectra.	33
2.8	Permeance distribution in the air gap at different stator tooth inner widths: (a) $b_{\text{ds}} = b_{\text{ds}1}$, (b) $b_{\text{ds}} = 19$ mm, (c) $b_{\text{ds}} = 23$ mm, (d) $b_{\text{ds}} = 28$ mm, and (e) their spectra. (cont.)	34
2.9	Air gap flux density distribution caused by PMs at different stator tooth inner widths: (a) $b_{\text{ds}} = b_{\text{ds}1}$, (b) $b_{\text{ds}} = 19$ mm, (c) $b_{\text{ds}} = 23$ mm, and (d) $b_{\text{ds}} = 28$ mm, and (e) their spectra.	37

2.9	Air gap flux density distribution caused by PMs at different stator tooth inner widths: (a) $b_{ds} = b_{ds1}$, (b) $b_{ds} = 19$ mm, (c) $b_{ds} = 23$ mm, (d) $b_{ds} = 28$ mm, and (e) their spectra. (cont.)	38
2.10	No-load normal air gap flux density waveform over the base machine with a scaled air gap flux density distribution over the stator tooth containing the coil at different teeth widths: (a) $b_{ds} = b_{ds1}$, (b) $b_{ds} = 19$ mm, (c) $b_{ds} = 23$ mm, and (d) $b_{ds} = 28$ mm.	40
2.11	RMS back-EMF value at the rated speed calculated by the analytical and FEA models as a function of the stator tooth inner width b_{ds}	41
2.12	(a) Induced voltage waveforms at the rated speed for different stator tooth inner widths b_{ds} and (b) their spectra.	41
2.13	Stars of slots of a three-phase 24-slot 20-pole machine for (a) $b_{ds} = b_{ds1}$ and (b) $b_{ds} > b_{ds1}$	42
2.14	Three-phase induced voltage phasor diagram for (a) $b_{ds} = b_{ds1}$ and (b) $b_{ds} > b_{ds1}$	42
2.15	Linear current density model of a single conductor in a slot.	43
2.16	Air gap flux density distribution caused by the armature reaction at different stator tooth inner widths: (a) $b_{ds} = b_{ds1}$, (b) $b_{ds} = 19$ mm, (c) $b_{ds} = 23$ mm, (d) $b_{ds} = 28$ mm, and (e) their spectra.	45
2.16	Air gap flux density distribution caused by the armature reaction at different stator tooth inner widths: (a) $b_{ds} = b_{ds1}$, (b) $b_{ds} = 19$ mm, (c) $b_{ds} = 23$ mm, (d) $b_{ds} = 28$ mm, and (e) their spectra. (cont.)	46
2.17	(a) Winding function ($b_0 \approx 0$ mm) at the rated speed for different stator tooth inner widths b_{ds} and (b) their spectra.	47
2.18	Flux plot when only phase U is supplied at different stator inner teeth widths: (a) $b_{ds} = b_{ds1}$, (b) $b_{ds} = 19$ mm, (c) $b_{ds} = 23$ mm, and (d) $b_{ds} = 28$ mm.	49
2.19	(a) Current linkage waveforms ($b_0 \approx 0$ mm) at different stator tooth inner widths b_{ds} and (b) their spectra.	50
2.20	Current linkage working harmonic ($v = 5$) and subharmonic ($v = 1$) amplitude ($b_0 \approx 0$ mm) as a function of the stator tooth inner width b_{ds}	50
2.21	Spectra of the winding factors at different stator inner teeth widths: (a) $b_{ds} = b_{ds1}$, (b) $b_{ds} = 19$ mm, (c) $b_{ds} = 20$ mm, (d) $b_{ds} = 23$ mm, and (e) $b_{ds} = 28$ mm.	51
2.22	Air gap harmonic leakage ($b_0 \approx 0$ mm) as a function of the stator tooth inner width b_{ds}	52
2.23	Torque performance of the nonskewed PMSM: (a) electromagnetic torque map and (b) cogging torque and torque ripple (peak-to-peak) as a function of the stator tooth inner width b_{ds}	54
2.24	(a) Cogging torque variation over one electrical period at different stator tooth inner widths b_{ds} and (b) their spectra (nonskewed rotor).	54

2.25	Torque performance of the skewed PMSM: (a) electromagnetic torque map and (b) cogging torque and torque ripple (peak-to-peak) as a function of the stator tooth inner width b_{ds}	55
2.26	(a) Cogging torque variation over one electrical period at a different stator tooth inner width b_{ds} and (b) its spectra (skewed rotor).	56
3.1	Flowchart of the procedure for calculating hysteresis torque and losses.	59
3.2	Mesh of the 24-slot 20-pole TCW PMSM for (a) $b_{ds} = b_{ds1}$ and (b) $b_{ds} = 19$ mm. The stator mesh adjusts for each value of b_{ds}	60
3.3	Hysteresis phenomenon. The flux density of the PM is fixed and the flux density in the tooth changes as the PMs rotate.	61
3.4	RMS back-EMF at the rated speed ($n_N = 80$ r/min) and RMS stator current value at the rated load ($T_N = 202$ Nm, $n_N = 80$ r/min) as a function of the stator tooth inner width b_{ds}	63
3.5	(a) Losses and (b) efficiency at the rated load as a function of the stator tooth inner width b_{ds} , where P_{Cu} are the copper losses, P_{Fe} are the laminated stator iron losses, and P_{rot} are the eddy-current losses in the solid rotor.	63
3.6	Magnetization curves of (a) 430SS and (b) M400-50A.	64
3.7	Core loss density distribution at the rated load for (a) $b_{ds} = b_{ds1}$ and (b) $b_{ds} = 19$ mm.	65
4.1	Exploded view of the rotor assembly: (1) tube, (2) PM, (3) cover, (4) drive end ring, (5) non-drive rotor end ring, (6) ring attachment screw bolts, and (7) wedge to center the fiberglass tube.	67
4.2	Canned rotor of the prototype.	68
4.3	Stator stack laminations of the prototype.	68
4.4	(a) Cable positions of one complete coil in the stator slots and (b) 3D printed model of part of the stator core with the coil inserted.	69
4.5	Prototype stator assembled. Glass-fibre slot keys guarantee the fixing of the coils. No impregnation was used for the winding.	69
4.6	(a) Schematic and (b) photograph of the experimental setup. The numbers shown in the photograph denote the component indicated in the schematic.	70
4.7	Comparison of the simulated and measured line-to-line back-EMF waveforms at the rated speed.	71
4.8	Simulated and measured mechanical torque at the rated speed as a function of RMS stator current.	71
4.9	(a) Simulated and (b) measured efficiency maps.	72

List of Tables

1.1	Comparison of the magnetic properties of different stainless steels [1]. . .	8
1.2	Parameters of the PMSM.	17
2.1	Possible slot–pole combinations to employ unequal teeth widths in the TCW.	25
3.1	Manufacturer data of the stator core materials.	64
3.2	No-load and rated load electromagnetic losses for $b_{ds} = b_{ds1}$ and $b_{ds} = 19$ mm.	65
3.3	Stator hysteresis torque for $b_{ds} = b_{ds1}$ and $b_{ds} = 19$ mm.	65
4.1	Machine losses at the rated point.	72



Nomenclature

Latin alphabet

A	area	m^2
a	number of parallel paths	–
B	flux density	T
B_n	normal component of the flux distribution	T
B_r	remanent flux density	T
B_s	saturation flux density	T
B_t	tangential component of the flux distribution	T
b_{ds}	stator tooth inner width that carries a coil	m
b_{ds1}	stator tooth inner width that does not carry a coil	m
b_s	stator slot width	m
b_0	slot opening width	m
C_p	turbine power coefficient	–
D_r	rotor outer diameter	m
D_{rye}	rotor yoke outer diameter	m
D_{ryi}	rotor yoke inner diameter	m
D_s	stator inner diameter	m
D_{se}	stator outer diameter	m
D_t	turbine diameter	m
d	diameter, lamination thickness	m
E	energy density	J/m^3
E_{ph}	RMS induced voltage	V_{rms}
e_{ph}	instantaneous induced voltage	V
f	frequency	Hz
f_N	rated frequency	Hz
H	field strength	A/m
H_c	coercive force	A/m
h_{PM}	permanent magnet height	m
h_{RC}	rotor cover thickness	m
h_{ys}	stator yoke depth	m
I_s	RMS stator current	A_{rms}
I_{sN}	rated stator current	A_{rms}
i	instantaneous current	A
i_s	instantaneous stator current	A
i_{sd}	direct-axis stator current	A
i_{sq}	quadrature-axis stator current	A
J	current density, magnetic polarization	$\text{A}/\text{m}^2, \text{T}$
j	imaginary unit	–
k_{Cu}	copper space factor	–
k_d	distribution factor	–

k_{ec}	classic eddy-current loss coefficient	$Ws/(T/s)^2/m^3$
k_{exc}	excess loss coefficient	$Ws/(T/s)^{1.5}/m^3$
k_{Fe}	iron space factor	–
k_h	hysteresis loss coefficient	$Ws/T^2/m^3$
k_p	pitch factor, proportionality constant of the pump	–, $Nm/(rad/s)^2$
k_R	resistance factor	–
k_{sq}	skewing factor	–
k_w	winding factor	–
L_h	air gap harmonic leakage inductance	H
L_m	magnetizing inductance	H
L_s	synchronous inductance	H
L_{sq}	skew leakage inductance	H
L_{tt}	tooth tip leakage inductance	H
L_u	slot leakage inductance	H
L_w	end winding leakage inductance	H
L_σ	leakage inductance	H
l	stator stack length	m
l_w	end winding length	m
M_{PM}	magnetization of the permanent magnet	A/m
m	number of phases	–
m_c	mutual coupling factor	–
N_{ph}	number of turns per phase	–
n	mechanical speed	r/min
n_N	rated mechanical speed	r/min
P_{Cu}	stator winding losses	W
P_d	drag losses	W
P_{elec}	electrical power	W
P_{Fe}	stator core losses	W
P_{hyst}	static hysteresis loss	W
P_{mech}	mechanical power	W
P_N	rated power	W
P_{rot}	rotor eddy-current losses	W
p	number of pole pairs	–
Q_s	number of stator slots	–
q_v	water flow	m^3/s
R_{ph}	stator winding resistance	Ω
r	radius	m
S_r	rotor wetted area	m^2
S_t	turbine sweep area	m^2
T	torque	Nm
T_c	cogging torque	Nm
T_d	drag torque	Nm
T_{em}	electromagnetic torque	Nm

T_{exc}	excitation torque	Nm
T_{hyst}	static hysteresis torque	Nm
T_{mech}	mechanical torque	Nm
T_N	rated torque	Nm
T_{p2p}	peak-to-peak torque	Nm
T_{rel}	reluctance torque	Nm
t	time	s
v	rotor surface linear speed, harmonic order	m/s, –
v_{sw}	seawater speed	m/s
W	coil pitch	°, rad, m
W_c	coenergy stored in the air gap	J
W_f	field energy	J
w_{PM}	permanent magnet width	m
z_q	number of conductors in one slot	–

Greek alphabet

α	mechanical position	°, rad
α_{PM}	relative permanent magnet width	–
β	blade pitch angle, electrical position	°, rad
β_0	slot opening angle	°, rad
Δp	total pressure difference of the pumping system	Pa
δ	air gap length	m
δ_{ef}	effective air gap length	m
δ_{phys}	physical air gap length	m
η_g	efficiency of the generator	–
η_m	efficiency of the motor	–
η_p	efficiency of the pump	–
γ	continuous skewing angle	°, rad
λ	tip ratio, relative permeance	–
λ_a	real part of the complex permeance distribution	–
λ_b	imaginary part of the complex permeance distribution	–
μ_r	relative permeability	–
μ_w	dynamic viscosity of water	Pa · s
μ_0	permeability of vacuum	Vs/Am, H/m
Ω	mechanical angular speed	rad/s
Ω_p	mechanical angular velocity of the pump	rad/s
Ω_t	mechanical angular velocity of the turbine	rad/s
ω	electrical angular velocity	rad/s
Φ_{PM}	permanent magnet flux	Vs, Wb
ψ_{PM}	permanent magnet flux linkage	Vs
ρ	resistivity, density	Ωm , kg/m^3
ρ_{Cu}	copper resistivity	Ωm

ρ_{sw}	mass density of seawater	kg/m ³
σ	conductivity	S/m
σ_{Fe}	stator core conductivity	S/m
σ_{δ}	air gap harmonic leakage factor	–
Θ	current linkage	A
τ_p	pole pitch	°, rad, m
τ_s	slot pitch	°, rad, m

Abbreviations

2D	two-dimensional
3D	three-dimensional
420SS	420 stainless steel
430SS	430 stainless steel
AC	alternating current
AR	armature reaction
BLDC	brushless DC
CP	complex permeance
CW	concentrated winding
DC	direct current
EMF	electromotive force
FEA	finite element analysis
FEM	finite element method
GCD	greatest common divisor
GFRP	glass-fiber-reinforced plastic
IM	induction machine
JA	Jiles–Atherton
LCM	least common multiple
NdBF _e	neodymium–iron–boron
PM	permanent magnet
PMSG	permanent magnet synchronous generator
PMSM	permanent magnet synchronous machine
PVC	polyvinyl chloride
RMS	root mean square
RP	relative permeance
SL	single-layer
SmCo	samarium–cobalt
SynRM	synchronous reluctance machine
TC	tooth-coil
TCW	tooth-coil winding
WPS	water pumping system



1 Introduction

Electricity is the main commodity of future energy systems. A vast amount of electricity generation will be needed to move away from the fossil energy system toward a totally carbon neutral energy system. At the moment, a high share of electricity is both produced and consumed by rotating electrical machines. In the late 2010s, electrical machines accounted for 45% of the global electricity consumption [2]. Currently, traditional electricity generation is mainly arranged in electric power plants that use steam or gas turbines [3]. Therefore, it is evident that rotating electrical machines are a fundamental part of development processes in countries around the world. In the future, however, all reasonable carbon-neutral means of generation have to be employed. Hydro, wind, and tidal power are means of power generation that use rotating machines. These forms of electricity generation can have a significant share of increased production in the future. Strong competition is, however, created by solar cells, which may surpass the share of rotating machines in the future. Rotating machines will, in all cases, maintain their position in the use of electricity as electrification is penetrating all areas of societies. One of the most important fields is mobility, where a hundred million electric propulsion motors will be needed annually if all vehicles are to be electrified.

Nowadays, there are various electrical machines, but alternating current (AC) machines have a very strong foothold. The most common AC machine type is still the induction machine (IM) [4]. It is a reliable and low-cost machine. Furthermore, its self-starting property and ability to work directly connected to the grid explain its wide use in the industrial sector in the 20th century [5], [6]. However, the advances in machine manufacture, power electronics and drives, and digital signal processor technologies have contributed to the development of alternative electrical machines, e.g., the synchronous reluctance machine (SynRM) and the permanent magnet synchronous machine (PMSM) [5], [7].

The operating principle of the PMSM is based on the use of permanent magnets (PMs) in machine excitation [8]. Although PMSMs emerged already in the middle of the 20th century, the poor characteristics of the early magnets limited their progress. However, from the 1980s onward, the appearance of rare earth PMs promoted the development of the PMSM [9]. This was due to the high energy density of neodymium–boron–iron (NdBFe) magnets compared with existing magnets. Today, the market offers a variety of permanent magnets. However, because of the price volatility and the long-term availability of rare earth magnets, replacing them with other alternatives has been investigated [10], or improved machine designs have been proposed that permit the use of magnets that provide a low magnetic field strength [11]–[13]. PMSM are widely used in various applications including, e.g., renewable energy devices as well as pumping and transportation machinery [14]–[18]. The growing interest in the PMSM is due to its following exceptional advantages [19]–[24]:

- high efficiency;
- high torque density;
- low maintenance cost;
- compact structure;
- wide-speed-range operation;
- good potential for high-overload characteristics;
- high power factor;
- working in low-speed/frequency applications without a significant penalty in efficiency (as in IMs);
- possibility to apply a high number of poles to reduce the machine size without an efficiency penalty (as in IMs and SynRMs).

These advantages allow the PMSM to be an acceptable alternative for direct-drive low-speed applications. The main idea about employing a direct-drive configuration is to avoid mechanical transmission elements, such as a gearbox, thereby increasing the system reliability and efficiency and reducing maintenance costs [21], [25]–[27]. Therefore, the machine must have a large number of poles, which indicates that the size of the machine will be larger, and also, a power converter is required. The cost of the system would thus increase [28]. For this reason, the machine must be properly designed to avoid a further increase in cost and poor performance.

1.1 Tidal energy

Tidal energy is an energy source caused by gravitational interaction between the Sun, the Moon, and the Earth that generates water movement of the oceans, creating the rise and fall in the sea level every 12.5 h. Therefore, tidal energy can be considered a sustainable energy source even though it consumes kinetic energy of celestial bodies. There are two ways to harvest the energy from tides: barrage and tidal stream systems [29]. The barrage system depends on the potential energy based on the height difference between high and low tides. The tidal stream system depends on the kinetic energy generated from seawater current to drive the turbine propellers.

The main component of a tidal current system is a turbine coupled to a generator converting mechanical energy into electrical energy. According to the turbine hydrodynamic model, the mechanical power that can be extracted is expressed as [30]

$$P_{\text{mech}} = \frac{1}{2} \rho_{\text{sw}} C_p (\lambda, \beta) S_t v_{\text{sw}}^3, \quad (1.1)$$

where ρ_{sw} is the mass density of seawater, C_p is the turbine power coefficient, β is the blade pitch angle, S_t is the turbine sweep area, v_{sw} is the seawater speed, and λ is the tip

ratio given by

$$\lambda = \frac{D_t \Omega_t}{2 v_{sw}}, \quad (1.2)$$

where D_t is the turbine diameter, and Ω_t is the mechanical angular velocity of the turbine. The turbine power coefficient C_p is the extractable power divided by the stream kinetic power. It is determined by the geometric characteristics of the turbine and the fluid properties [31]. The turbine power coefficient C_p ranges from 0.35 to 0.50 [32]. The mass density of seawater ρ_{sw} is around 1000 kg/m³. Variations in salinity and temperature influence the density of seawater on the surface [33]. The seawater speed v_{sw} , on average at specific locations, varies between 1 and 3 m/s [34]. The mechanical torque of the turbine is provided by

$$T_{mech} = \frac{P_{mech}}{\Omega_t}. \quad (1.3)$$

Based on the above, tidal energy has a high power density and a low speed, where the average turbine speed is around 14 to 25 r/min [29], [32]. Therefore, the mechanical torque T_{mech} is expected to be high. The application scenario indicates that a high-torque low-speed generator must be designed.

Figure 1.1 shows the tidal power energy conversion scheme for a direct-drive low-speed permanent magnet synchronous generator (PMSG); the machine is directly coupled to the turbine and entirely submerged. The generator is connected to a power converter, which is required because of the variability of the tidal current speed.

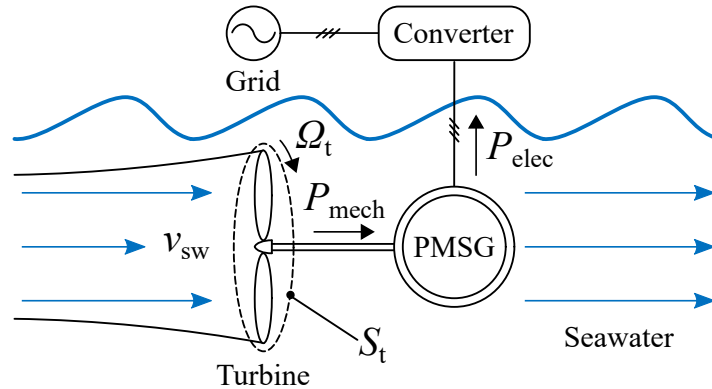


Figure 1.1: Configuration of the direct-driven PMSG tidal energy conversion system. The electrical power is defined by $P_{elec} = \eta_g P_{mech}$, where η_g is the generator efficiency.

1.2 Water pumping system

A water pumping system (WPS) consists of several fundamental elements: a power source, a power converter, a motor, and a pump [35]. The components of the system are selected and built according to the scenario application. The primary function of the system is to transport water from one point to another by employing the pump driven by a motor.

The widely preferred electrical machines in this type of application are IMs. This is due to their robustness and ease of speed control [36]. However, PMSMs have gained popularity in this application because of their high performance characteristics [37], [38]. Furthermore, the PMSM offers a better performance in the low-speed region than the IM [39], [40]; thus, it is more suitable for low-speed water pumping systems.

The schematic diagram of a typical WPS is presented in Figure 1.2; the motor is directly coupled to the pump. Therefore, the input power of the pump is theoretically equal to the mechanical power of the motor and can be determined as

$$P_{\text{mech}} = \frac{\Delta p \cdot q_v}{\eta_p}, \quad (1.4)$$

where η_p is the efficiency of the pump, Δp is the total pressure difference of the pumping system, and q_v is the water flow. Therefore, the mechanical torque can be expressed in the same way as Equation (1.3). Assuming that both the impeller diameter and the pump efficiency are kept constant, the affinity law can be employed in such a way to simplify the calculations [36]. Therefore, the pump torque can be modeled as a function of the rotational speed of the pump Ω_p by the following expression [41]

$$T_{\text{mech}} = k_p \Omega_p^2, \quad (1.5)$$

where k_p is the proportionality constant of the pump.

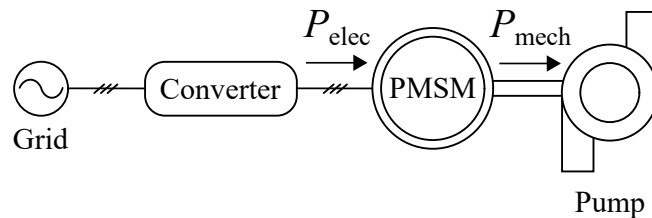


Figure 1.2: Schematic diagram of a water pumping system. The mechanical power is defined by $P_{\text{mech}} = \eta_m P_{\text{elec}}$, where η_m is the motor efficiency.

1.3 Brief discussion of applications

The brief overview of the applications presented in Sections 1.1 and 1.2 shows a similarity: the electrical machine under study is submerged in water. Therefore, the machine must meet a particular specification directly related to its design and manufacture, which must be waterproof. This indicates that the machine must be resistant to corrosion to avoid degradation of its components. There are several ways to achieve this, and they will be discussed in more detail in the next section.

1.4 Submersible machines

Numerous studies have investigated submersible machines [42]–[44]. They are characterized by operating submerged in a fluid (preferably water) and used in application scenarios such as tidal energy or a water pumping system. It is possible to find at least three types of submersible machines: fully enclosed, canned, and wet.

The completely enclosed machine is hermetically sealed, meaning that water cannot fill the air gap. For example, in [42], a ferrite magnet spoke-type submersible brushless DC (BLDC) motor with 15 slots and 10 poles is proposed. It has a large axial length and a small diameter. The motor is insulated from water by a nonmagnetic stainless steel flanges and frame.

In the second type, the stator and rotor parts are protected by covers or cans so that water can penetrate into the air gap. Examples of canned machines are presented in [43], [44]. In [43], it was studied a canned rotor surface magnet PMSM with 12 slots and 10 poles. In this motor both rotor and stator are canned by a nonmagnetic steel can (Hastelloy C material). The fluid flows within the air gap between the cans, and therefore, the liquid does not have contact with the sensitive parts of the machine. However, the eddy currents induced in the cans increase the machine losses and reduce the air gap flux density. Despite this, the can eddy currents also suppress higher order harmonics of the air gap flux density, which reduces the PM eddy current losses. In [44], it was investigated a flooded surface magnet PMSG. In their study, it was shown how large extra losses the electrically conductive cans create and how the temperature of the motor active parts is increased. However, with nonconductive materials, e.g., glass-fiber-reinforced plastic (GFRP), the inside temperature of the stator slots and the PMs was lower than in the case with nonmagnetic metallic cans.

The wet machine is entirely filled with water, which means that the machine components must be protected by waterproof insulation materials. In contrast to the other types of submersible machines, some parts of the machine are exposed to water even when adequately protected. For example, a submersible water pump was presented in [45]. This device consists of a wet stator winding in permanent contact with water, which acts as a cooling medium. Therefore, in this type of machine the water flow

influences heat transfer.

1.5 Device materials for a submersible machine

The main problem in an underwater environment is that water is a corrosive medium. Therefore, traditional materials used in the manufacture of machines can be affected by corrosive environments that deteriorate their properties over time. In the case of electrical steels, iron (Fe) alloys are the most commonly used materials in electrical machines [46], but iron is susceptible to corrosion if it is not combined with suitable elements or it is not in a stable state. Rare-earth-based magnets, in turn, are prone to rapid disintegration in corrosive environments if not adequately protected [10]. Moreover, the winding of the machine can be exposed to early interruptions caused by corrosion [47]. Hence, it is necessary to investigate materials suitable for submersible applications, e.g., corrosion resistant magnetic materials or protective coatings to ensure high durability and corrosion resistance. The materials of the device can be grouped into four categories: stainless steel materials, cover materials, permanent magnet materials, and winding materials. Each category will be discussed in a section of its own below.

1.5.1 Stainless steel materials

Stainless steel materials are typically iron-based alloys that are characterized by being resistant to corrosion. In addition to iron (Fe), their composition includes chromium (Cr) and carbon (C). Other alloy elements can also be incorporated to improve specific characteristics (machineability, low- and high-temperature resistance, electrical resistivity). Because of their particular properties, stainless steels are widely used in various applications, ranging from medicine and engineering to domestic uses [48], [49].

There are three types of stainless steels: austenitic, martensitic, and ferritic [50]. There are also other stainless steel types (duplex and precipitation hardened), which are combinations of the basic stainless steel types [49]. The selection of stainless steel for an electrical machine depends on the use: the manufacture of machine cores or coatings. However, there is always some uncertainty related to the selection of stainless steel. The reason for this is that detailed magnetic properties of stainless steel are not generally available, and therefore, measurements are required. As reported by [1], martensitic steel exhibits a higher corrosion resistance than austenitic and ferritic steels. However, ferritic steels have lower coercive force values than martensitic steels, and austenitic steels are nonmagnetic materials. Therefore, when choosing a stainless steel material for magnetic core manufacture, the following items should be taken into account [51]:

1. High magnetic saturation;
2. Low coercivity;
3. High relative permeability;
4. Low magnetic losses:
 - (a) small-area BH loop;
 - (b) high electrical resistivity.

Figure 1.3 shows BH curves of electrical steels used in the manufacture of electrical machines and stainless steels. The BH curve of stainless steel was obtained by measurements with a hysteresisgraph. The 420 stainless steel (420SS) corresponds to martensitic steel and the 430 stainless steel (430SS) to ferritic steel. As can be seen, their saturation flux densities are higher than those of traditional magnetic materials except for cobalt–iron (Co–Fe) material. It should be noted that martensitic steel (420SS) has a higher saturation flux density than ferritic steel (430SS). Considering magnetic saturation, 420SS is better than 430SS. However, a more detailed analysis of their magnetic characteristics is needed along with their chemical composition to investigate their applicability to electrical machine cores.

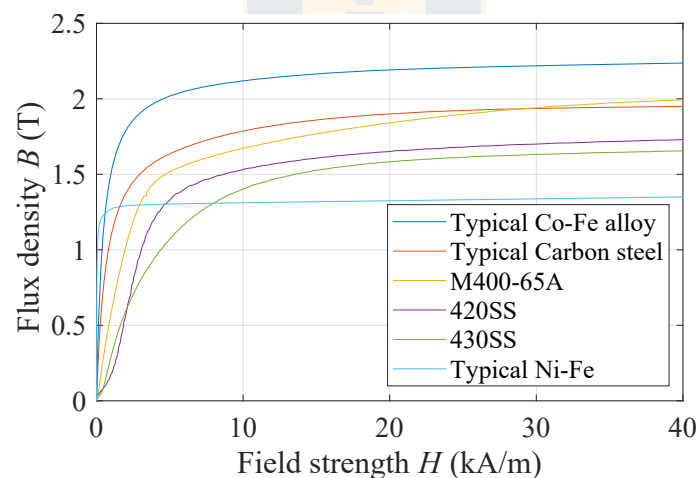


Figure 1.3: Magnetization curves of traditional electrical steels used in the manufacture of electrical machines and stainless steels.

Table 1.1 shows the magnetic properties of various stainless steels. It is evident that the type of steel and the chemical composition relates to the magnetic properties. The corrosion resistance of the stainless steel is provided by its Cr content. This is because Cr bonded with oxygen (O) forms a tight transparent layer over the steel surface that does not allow oxidation [52].

Table 1.1: Comparison of the magnetic properties of different stainless steels [1].

Steel	Type	Content (% weight)		Maximum permeability μ_{\max}	Coercive force H_c (A/m)	Saturation flux density B_s (T)	Residual flux density B_r (T)
		Cr	C				
410	Martensitic	11.7	0.13	360	770	1.50	0.61
416	Martensitic	12.2	0.12	490	900	1.42	0.82
420*	Martensitic	11.7	0.34	257	1200	1.73	0.72
430*	Ferritic	16.4	0.017	250	708	1.66	0.40
430F	Ferritic	17.5	0.027	530	560	1.41	0.75
430FR	Ferritic	17.6	0.029	960	270	1.35	0.50
446	Ferritic	25.8	0.063	450	670	1.20	0.62

*Measurements of magnetic properties carried out with a hysteresisgraph.

According to [1], there is an approximately linear dependence (directly proportional) between the carbon (C) content and the coercive force H_c . The relative permeability μ_r decreases with an increasing C content. The saturation flux density B_s is inversely proportional to the Cr content. The residual flux density B_r remains unchanged as the C content varies.

Ferritic and martensitic stainless steels have a high electrical resistivity, which indicates a potential for low eddy current losses. It is explained by incorporation of elements that decrease electrical conductivity, e.g., silicon (Si) [1]. The lamination thickness is a characteristic to consider when choosing the stainless steel material. The eddy current losses can be effectively reduced by decreasing the sheet thickness. Typical thicknesses of electrical steels are between 0.65 to 1 mm [53]. Therefore, the lamination thickness of stainless steel must be within that range.

1.5.2 Cover materials

Some of the traditional materials used in electrical machines are not resistant to corrosion, but they can be protected against water penetration, e.g., by using a can or cover. Different cover arrangement alternatives in a PMSM are shown in Figure 1.4. As mentioned in [44], [54], [55], the covers can be made of metallic or nonconductive materials. Considering metallic materials there are austenitic stainless steels or Hastelloy C (based on nickel and alloys of other elements). They are characterized by being nonmagnetic and resistant to corrosion. However, they are conductive, which can produce additional losses in the machine. In the case of nonconductive materials, there is, e.g., GFRP (also known as fiberglass). It is resistant to corrosion and nonmagnetic, and it has an ultrahigh electrical resistivity. The thickness of the GFRP should, however, be larger than the thickness of stainless steel to achieve similar mechanical stiffness. In [54], it is reported that the thickness of the fiberglass should be three times the thickness of stainless steel. This means that when using plastic covers the length of

the effective air gap will be greater than when using metallic cans.

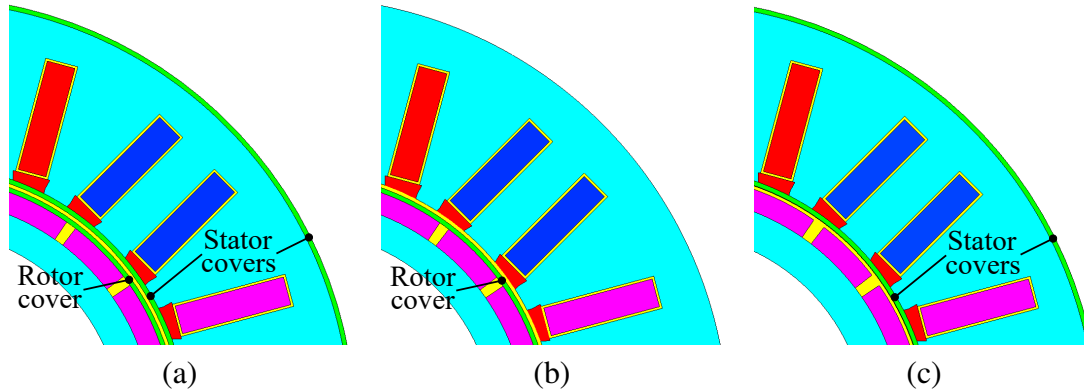


Figure 1.4: Cover arrangement alternatives in a rotor surface PMSM: (a) canned machine, (b) canned rotor, and (c) canned stator.

1.5.3 Permanent magnet materials

The magnets mostly used for the design and manufacture of electrical machines are alnico, ferrite, samarium–cobalt (SmCo), and NdFeB [10], [11], [56].

At present, the most powerful PMs used in electrical machines are NdFeB magnets. However, they are vulnerable to corrosion, which can manifest itself in two ways [57]–[59]:

- Oxygen (O_2) diffuses into the surface layer of the magnet causing a metallurgical change in the layer, and as a result, the coercive force will decrease, increasing the risk of demagnetization.
- Hydrogen (H) in the environment reacts with neodymium (Nd), which destroys the original grain structure leading to porosity in the material and causing a loss of the PM magnetic properties.

Therefore, to prevent corrosion from moisture in the atmosphere, a thin protective layer is added to the magnet surface.

Ferrite, alnico, and SmCo magnets are resistant to corrosion, but they do not provide the same magnetic properties as NdFeB magnets. However, SmCo magnets can strongly compete with the NdFeB magnet properties, especially at higher temperatures, but they are usually much more expensive. Ferrite and alnico magnets contain iron that can be oxidized by a reaction with water and oxygen. However, in ferrite magnets, the iron content is in a stable oxidized state, which means that it cannot be oxidized. In alnico magnets, there is iron, and the magnets can thus be susceptible to oxidation by humidity. They can be provided with a protective layer to avoid oxidation. SmCo magnets do not contain iron; therefore, they are resistant to corrosion [60]–[63].

1.5.4 Winding materials

In submersible machines, the winding requires a high waterproof insulation quality. Different types of wires, depending on their type of insulation, can be classified as [47]:

- 1) Standard enameled wire (no extra protection);
- 2) Enameled wire encapsulated with a protective material;
- 3) Wire with proper protection.

Figure 1.5 shows the different alternatives of wires for submersible applications.

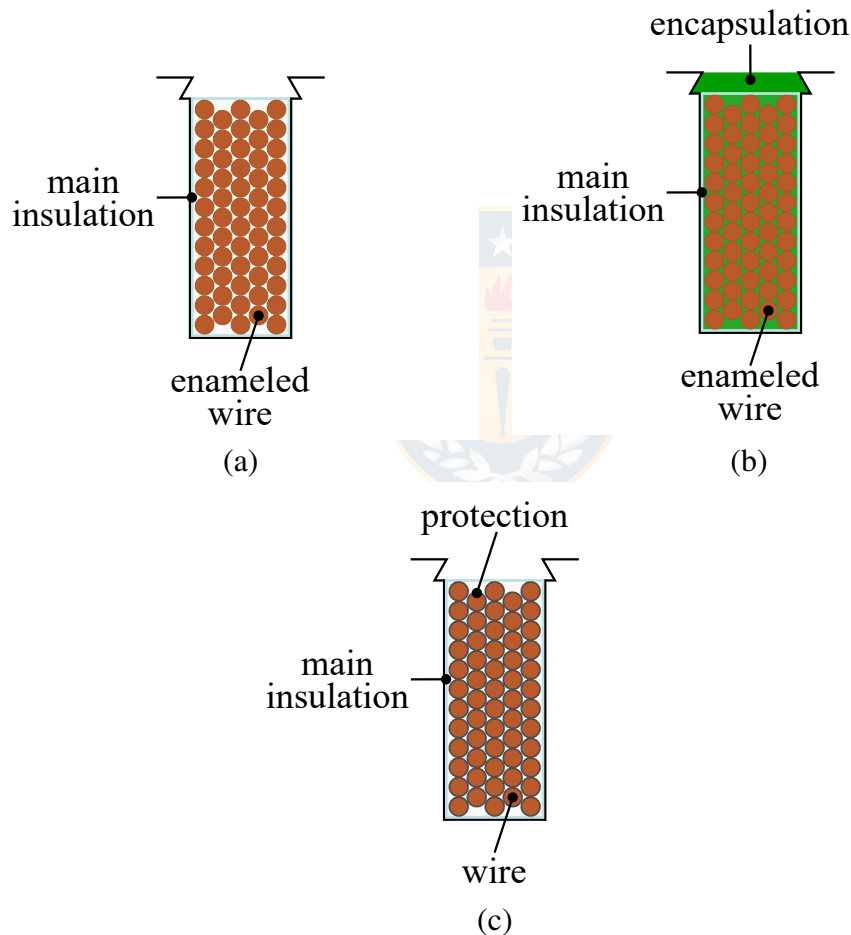


Figure 1.5: Possible wires for use in submersible environments: (a) standard enameled wire, (b) enameled wire encapsulated with a protective material, and (c) wire with proper protection.

The enameled copper wire is the most commonly used material for the manufacture of electrical machines. It is characterized by low resistivity, good ductility, high strength, and corrosion resistance. If water is circulated in the stator (as in a wet machine), there can be an advantage in the heat transfer between the winding and the fluid. However, to

avoid early interruptions caused by a winding contact with water, it is advisable to use enameled with extra insulation protection wire (case 2 and 3). However, any insulation reduces the thermal conductivity. For case 2, there are suitable materials for encapsulation (standard enameled wire can be used), such as epoxy resin and silicone encapsulant. They offer acceptable thermal conductivity and good protection against water [64], [65]; however, convection heat dissipation could be ineffective because of encapsulation blocks [47].

For case 3, there is a low-cost alternative, PVC-insulated solid-conductor wire. PVC insulation reduces the risk of both phase-to-phase and turn-to-turn short-circuits (this is also an advantage for case 2). However, PVC is characterized by a low thermal conductivity [66]. Furthermore, because of the significant PVC jacket thickness required, the space factor in the machine slot is reduced, contrary to the other cases, where it is possible to employ standard enameled wire. Despite this, the PVC-insulated wire being surrounded by water, its heat dissipation is typically better compared with a total encapsulation with epoxy resin. Moreover, its simple assembly and versatility make it a suitable candidate for submersible applications.

1.6 Tooth-coil winding

The concentrated non-overlapping winding is also known as the tooth-coil winding (TCW). It is a configuration that has been investigated for several years [25], [67], [68]. The main characteristic of the TCW is that each coil is wound around a single stator tooth, which means that the coils are non-overlapping.

TCW technology provides numerous advantages over other winding configurations, such as

- Easy manufacture and assembly [25]. By selecting open slots, the machine assembly process can be significantly simplified as shown in **Publications II and IV**.
- A high slot space factor, which could improve the thermal conductivity of the winding and reduce winding Joule losses [69].
- Short end turns, which mean cost savings and mass reduction of the winding material and also reduction in the winding Joule losses [70].
- Possibility of using the technology in modular and segmented stator structures, thereby achieving physical decoupling [13], [71]–[73].
- Fault tolerance (reduction or even elimination of the contact between conductors of different phases) [67], [68].
- Low cogging torque and torque ripple. These characteristics increase the service life of the mechanical machine parts and potential reduction of the noise level [74].

Despite these advantages, one of the main problems of the TCW is the wide spectrum of space harmonics in the current linkage waveform [75], [76]. In addition, the slotting effect influences the current linkage waveform [72]. These aspects affect the rotor losses, typically generating more rotor losses in the slot–pole combinations of TCWs, which contain more low-order current linkage harmonics. Moreover, harmonics have been reported to cause additional saturation and high torque ripple. However, it is possible to limit them by selecting a proper slot–pole combination or applying a multilayer structure [77], [78]. There are other alternatives to exclusively limit rotor losses, such as rotor lamination and magnet segmentation, among others [79].

1.7 Asymmetric features in the PMSM

Asymmetric features have been the interest of researchers in recent years. The main objective here is to improve the performance of the machine by changing its structure without modifying its size compared with its symmetrical version. The machine performance improvements include: an increase in induced voltage and electromagnetic torque and minimization of torque ripple and cogging torque.

A novel procedure to maximize the machine performance by deploying unequal teeth widths in nonoverlapping concentrated winding (CW) PM brushless machines was investigated in [80]. In the procedure, the width of the tooth tips of the teeth that carry coils is increased while keeping the slot area constant. Therefore, by increasing the tooth tip width, the magnetic flux per tooth is increased, and thus, the electromagnetic torque can be improved and the torque ripple reduced.

In [81], a new method to reduce the torque ripple in PMSMs was presented. It was shown that low-order torque ripple harmonics are produced because of the asymmetrical flux density distribution of the stator teeth. It was also found out that it is possible to minimize these harmonics by using unequal teeth widths. The method is, however, restricted to a particular working point.

In [82], it was shown that in TCW PMSMs strong armature reaction and PM flux together saturate the magnetic circuit, which causes a nonsymmetric flux distribution and significantly reduces torque quality. Therefore, to limit these problems, asymmetries in the stator and rotor were studied.

A method for minimizing the cogging torque with a quasi-skew asymmetric rotor structure was introduced in **Publication III**. The main idea of the method is to build a rotor geometry based on the relative positions of the poles per layer of a conventional skewed rotor. For example, by applying a three-step skewed rotor to a 72-slot 12-pole PMSM (see Figure 1.6a), each layer is offset by 1.67° from the next layer (to reduce the lowest harmonic order component of the cogging torque). Then, by applying a quasi-skewed rotor, the rotor of the machine is divided into four groups (12 poles divided

by three layers), where each group is made of three poles, where the first pole is positioned according to the pole position of the first layer of the three-step skewed rotor, and then, the second pole is positioned according to the pole position of the second layer, and so on, as shown in Figure 1.6b. This method makes it possible to avoid rotor skewing, which facilitates its manufacture. Moreover, it was found that the performance of the machine is similar to that of the machine with conventional rotor skewing, and with the proposed configuration, it was possible to minimize the cogging torque.

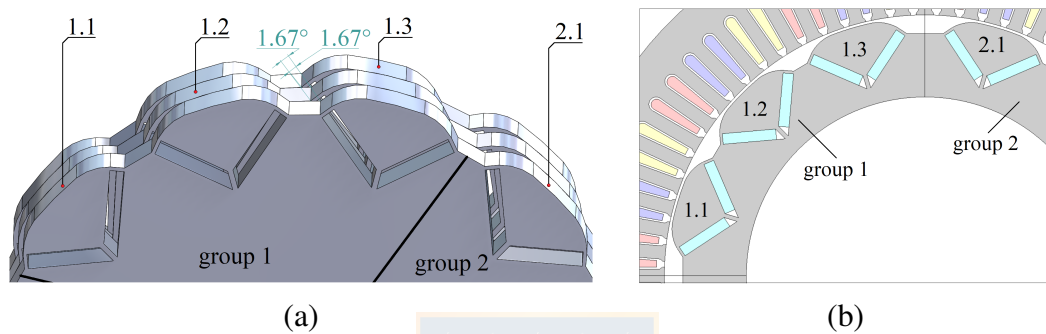


Figure 1.6: Examples of the step skewing: (a) three-step skewing of the 12 pole rotor with the skew angle of 1.67° between the layers and (b) quasi-three-step skewing of the 12 pole rotor with the quasi-skew angle of 1.67° .

In [83], an asymmetrical rotor hybrid TCW PMSM with improved torque performance was exhibited. The proposed approach was to modify the rotor structure of a conventional symmetrical rotor hybrid spoke-type PM machine by asymmetric positioning of the upper part of the PMs to enhance torque generation. The idea was to adjust the reluctance torque component to reach the maximum value at the same current phase angle at which the excitation torque is at the maximum.

A four-layer PMSM with 12 slots and 10 poles having coils with different numbers of turns was presented in [84]. The total number of conductors per slot was kept constant to have an invariant slot space factor. In this case, the asymmetry allows canceling lowest-order subharmonics of the air gap flux density waveform, which could improve the machine performance.

A modular PMSM with unequal teeth widths was introduced in [85]. Such a machine employs TCW, and it consists of independent modules with a single-layer (SL) winding. It was shown that the air gaps between the modules (also known as stator gap) and unequal teeth widths enhance the winding factor. However, the average torque can be improved or degraded according to the slot–pole combination by applying different stator gap widths.

1.8 Discussion

Based on the research, it was found that for the PMSM to operate underwater, its parts must be resistant to corrosion. Therefore, it is necessary to use protective elements to seal the active part of the machine from direct contact with water. However, these protective elements are prone to failure over time, reducing the machine lifetime. Hence, it is necessary to search for alternative materials to manufacture electrical machines resistant to permanent water contact. One way to enhance the reliability of the machine is to use ferritic stainless steels, which are corrosion resistant and have good magnetic properties. They also make it possible to avoid the use of protective covers, e.g., in the stator, where a complete encapsulation is a complex structure as it includes waterproof protection on both inner and outer sides. However, it is essential to use extra winding protection to prevent early interruptions caused by winding contact with water. From a thermal point of view, it is advisable to avoid enameled wire encapsulated with a protective material because the heat transfer in that case is low. For example, the PVC-insulated wire is a good alternative because of its low cost and availability in the market and because it offers appropriate heat transfer. In the case of the rotor part, it is also possible to make the rotor core of stainless steel, but some kind of encapsulation of the PMs is required to avoid their corrosion caused by permanent contact with water unless more expensive samarium cobalt magnets are applied. Therefore, the rotor core can be made of traditional electric steel.

It is well known that PMs can be demagnetized mainly as a result of faults or the effect of temperature [86]. However, if the machine is submerged in water, the maximum rotor temperature will remain low, which means that the risk of demagnetization will be low even for low-grade magnets.

The use of the TCW is a good alternative owing to its significant advantages, such as easy manufacture and assembly and good fault tolerance. The problems of the TCW related to the high harmonic content of the current linkage waveform and its effects on the rotor losses can be addressed in several ways. Furthermore, the use of the TCW technology allows enhancing the machine performance by using asymmetries in the stator.

1.9 Overview of the submersible PMSM under study

The machine studied in this doctoral dissertation is a radial flux PMSM designed to operate underwater. The application for which it was designed was to operate as a pump motor. However, it can also be used as a generator to harvest tidal energy.

An interior PMSM has certain advantages such as a low cogging torque and a good torque capacity over a wide speed range—especially in field weakening—compared with a rotor surface magnet PMSM [87]. Such a rotor configuration exhibits magnetic saliency, which makes it possible to generate some reluctance torque. However, a TCW

arrangement has been shown to reduce the magnetic saliency of any interior PMSM [87], [88]. Therefore, in the case of a TCW machine, the advantage of using embedded magnets to achieve some additional torque is, to a large extent, lost. In addition, when using this rotor configuration, it is necessary to use laminations in the rotor. In this very case, the high losses in the stator-side steel material should not encourage the use of the same material on the rotor side but some electrical steel material should be used instead. Using a laminated rotor in this case would also make it difficult to manufacture. Instead, it is possible to employ a solid rotor core by selecting rotor surface magnets. Because of all these reasons, a rotor surface magnet PMSM is chosen.

The geometry of the machine is shown in Figure 1.7. The main parameters of the PMSM are given in Table 1.2. The geometric parameters are determined from the design algorithm provided in [8]. More details on the design guidelines of the machine under study can be found in **Publication IV**. The value of the stator inner tooth width b_{ds} is chosen to increase the induced voltage and electromagnetic torque over the symmetric machine without adjusting the external dimensions of the machine and keeping the machine losses at a fair value. This will be studied in the following chapters.

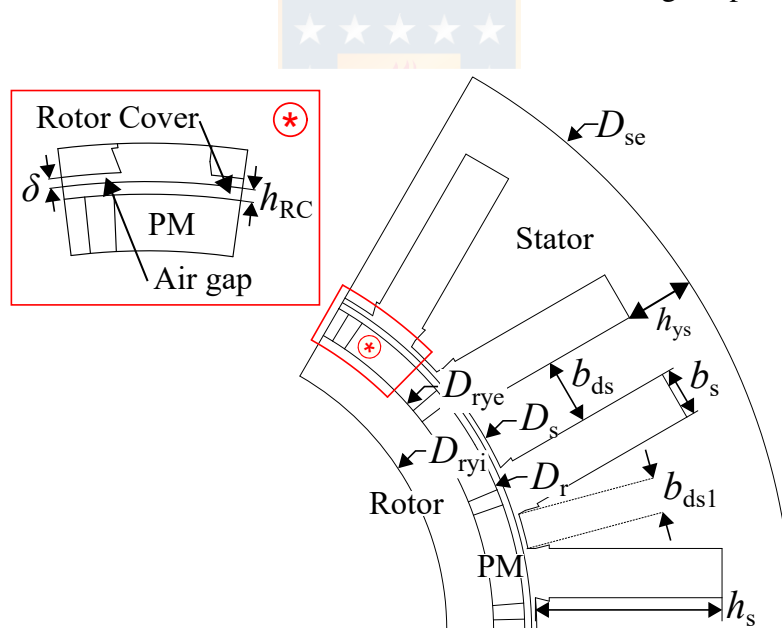


Figure 1.7: Cross-sectional view of the submersible core PMSM.

The structure consists of an outer stator and an inner rotor. The PMs are mounted on the rotor core surface as such a construction can be used with a rotor yoke made of a simple solid core tube. PMs have a curved shape to align the PM surface with the rotor surface. To simplify the assembly with the reduced risk of PM cracking, each magnet block is divided into four segments. The rotor is protected against the water environment by a cover to avoid direct contact of the water with the magnets.

The PM material selected is N45SH Neodymium Magnet. It has a remanent flux density of 1.35 T, coercive force of 1015 kA/m, and a relative permeability of 1.05. The isotropic resistivity of the PM is $180 \times 10^{-8} \Omega\text{m}$ at 20 °C.

The rotor core is made of S355 structural steel (also known as Fe52) as it presents fair mechanical and magnetic properties [89]. Its isotropic resistivity of $25.7 \times 10^{-8} \Omega\text{m}$ at 20 °C is acceptable to limit the rotor losses caused by the winding configuration used. The material selected for the rotor cover is GFRP because it has a low electrical conductivity and it is nonmagnetic.

There is no cover to protect the stator because the chosen stator materials are corrosion resistant. The stator core is made of 430SS, which is a ferritic stainless steel with exceptional corrosion resistance and favorable magnetic properties, and it is available in the market. The isotropic resistivity of 430SS is $60 \times 10^{-8} \Omega\text{m}$ at room temperature. PVC-insulated solid-conductor wires are chosen as the winding material, because they are entirely water-resistant and a low-cost alternative and provide high-quality insulation.



Table 1.2: Parameters of the PMSM.

Parameter	Value
Rated power P_N (W)	1700
Rated torque T_N (Nm)	202
Rated frequency f_N (Hz)	13 $\frac{1}{3}$
Rated stator current I_{sN} (A _{rms})	9.4
Rated mechanical speed n_N (r/min)	80
Number of stator slots Q_s	24
Number of poles $2p$	20
Stator stack length l (mm)	300
Stator outer diameter D_{se} (mm)	369.9
Stator inner diameter D_s (mm)	222.1
Stator yoke depth h_{ys} (mm)	19.9
Stator slot width b_s (mm)	14.25
Stator tooth inner width that carries a coil b_{ds} (mm)	19.0
Stator tooth inner width that does not carry a coil b_{ds1} (mm)	10.27
Physical air gap length δ (mm)	3.5
Rotor outer diameter D_r (mm)	197.1
Rotor yoke outer diameter D_{rye} (mm)	179.1
Rotor yoke inner diameter D_{ryi} (mm)	170.0
Rotor cover thickness h_{RC} (mm)	2.0
Permanent magnet width w_{PM} (mm)	27.9
Permanent magnet height h_{PM} (mm)	9.0
Number of turns per phase N_{ph}	232
Stator winding resistance R_{ph} (Ω)	1.1
Resistance factor k_R @ f_{sN}	~ 1.0
Synchronous inductance L_s (H)	0.027
Winding connection	star

*Symmetric stator: $b_{ds} = b_{ds1} = 14.68$ mm

1.10 Outline of the doctoral dissertation

This doctoral dissertation focuses on the modeling and analysis of a TCW PMSM with unequal teeth widths for submersible environments. The dissertation is based on four scientific publications, and it is divided into five chapters.

In **Publication I**, a straightforward design of the PMSG for harvesting tidal current energy is presented. The paper provides a review of the application scenario and electromagnetic design guidelines of the PMSG based on the application. The performance analysis of the machine is carried out by the finite element analysis (FEA). The use of stator asymmetries to improve the machine performance and hysteresis torque are investigated in brief.

In **Publication II**, an analysis of the stator asymmetry (unequal teeth widths) of the machine under study is presented. In this paper, an analytical method that incorporates the stator asymmetry to calculate the induced voltage is proposed. The method is validated with the finite element method (FEM). The performance of the machine (torque and losses) is carried out by the FEA.

In **Publication III**, an alternative method to minimize the cogging torque in a PMSM is exhibited. The method is based on the traditional skewed rotor, and it avoids the step skew, thereby facilitating its manufacture. From an electromagnetic point of view, the performance of the machine is similar to that of using the traditional skewing method, and it reduces the cogging torque.

In **Publication IV**, a loss analysis of the machine under study is presented. The stator iron losses are computed by employing the proposed nonconventional method. It is found that the stator core losses are dominant (45% of the total losses at the rated point) because of the magnetic properties of the chosen core material. This also results in the fact that there is a strong torque contrary to the movement of the machine (detent torque).

The structure of the doctoral dissertation is the following:

- Chapter 1 presents a literature review of the principal issues related to submersible machines. The chapter begins by presenting the role and importance of electrical machines worldwide. Next, the advantages of PMSMs are studied in brief, and their potential as candidates for direct-drive applications is discussed. Then, possible application scenarios in which submersible machines are used are introduced. Furthermore, submersible machines are investigated according to their sealing arrangement. After that, device materials resistant to corrosion for wet and canned machines are described. TCW technology and asymmetrical geometries in electrical machines are introduced in brief. Finally, an overview of the submersible TCW PMSM studied in this doctoral dissertation is given. This chapter is based on **Publications I–IV**.

- Chapter 2 provides an in-depth study of the TCW PMSM through an analytical approach and the FEM, focusing on the asymmetric stator structure of the machine, that is, the deployment of unequal teeth widths. The chapter begins by studying the PMSM modeling equations, illustrating how it is possible to improve the performance of the machine (induced voltage and electromagnetic torque) by varying the tooth width. It is then explained how the induced voltage and the air gap flux density are calculated by using an analytical method. To determine these characteristics of the machine, it is necessary to calculate the air gap permeance distribution. In this doctoral dissertation, the permeance distribution models most commonly used in the field of electrical machine design are deployed and compared. The analytical results are compared with the finite element analysis results. The main parameters of the machine (e.g., air gap flux density, induced voltage, electromagnetic torque, and current linkage) and the effect of unequal teeth widths on them are discussed. This chapter is based on **Publication II**.
- Chapter 3 investigates the calculation of the losses of the submersible TCW PMSM. The calculation is focused on employing unequal teeth widths. The calculation of the stator iron losses is carried out in a nonconventional way. The reason for this is that the iron loss coefficients are not available because the core material used is not traditional in the manufacture of machines. The winding losses, eddy-current losses, and mechanical losses are calculated using well-known conventional methods. This chapter is based on **Publication IV**.
- Chapter 4 describes the manufacture of the submersible TCW PMSM. A comparison between the experimental and FEA results of the machine is made. This chapter is based on **Publications II and IV**.
- Chapter 5 presents the conclusions and future work of this doctoral dissertation.

1.11 Scientific contributions

The main objective of this doctoral dissertation is to develop and experimentally validate a stainless-core submersible PMSM with unequal teeth widths. The research hypothesis is to verify whether it is possible to develop a submersible PMSM that is (i) functional, (ii) resistant to underwater environments, and (iii) easy to manufacture.

This doctoral dissertation presents the following scientific contributions:

- Development of a 2D analytical model to determine the air gap flux density distribution of a TCW PMSM with unequal teeth widths.
- Comparison of permeance distribution models most commonly used in the field of electrical machine design in the air gap of a TCW PMSM with unequal teeth widths.
- Extensive research on the influence of the unequal teeth widths in the TCW PMSM.
- Development of a nonconventional method to estimate the stator iron losses.
- Analysis and verification of the behavior of the manufactured submersible TCW PMSM.

1.12 Engineering contribution

A functional submersible PMSM was manufactured. The process provided important details (a practical approach) about its assembly. The machine was tested in a water tank to verify its operation and behavior when it is in contact with water at room temperature. The machine has also been operating in a pump system for water quality enhancement in a Finnish lake for three years, and it has so far proven reliable and capable of operating satisfactorily.

2 Tooth-coil winding with unequal teeth widths

2.1 Introduction

Based on the classical dq theory, the electromagnetic torque when considering saturation produced by the three-phase PMSM is given by [90]

$$T_{\text{em}} = \frac{3}{2}p \left[\underbrace{\psi_{\text{PM}}(i_{\text{sd}}, i_{\text{sq}}) i_{\text{sq}}}_{T_{\text{exc}}} + \underbrace{(L_{\text{sd}}(i_{\text{sd}}, i_{\text{sq}}) - L_{\text{sq}}(i_{\text{sd}}, i_{\text{sq}})) i_{\text{sd}} i_{\text{sq}}}_{T_{\text{rel}}} \right], \quad (2.1)$$

where p is the number of pole pairs, ψ_{PM} is the PM flux linkage, $i_{\text{sd}}, i_{\text{sq}}$ are the d- and q-axis components of the stator currents, and $L_{\text{sd}}, L_{\text{sq}}$ are the d- and q-axis components of the synchronous inductance. As it can be seen in Equation (2.1), torque production is divided into the excitation torque T_{exc} and the reluctance torque T_{rel} . In the case of the rotor surface PMSM, $L_{\text{sd}} \approx L_{\text{sq}} \approx L_s$; thus, $T_{\text{rel}} \approx 0$. It indicates that the electromagnetic torque depends on the q-axis component of the stator current i_{sq} and the PM flux linkage ψ_{PM} . Another way of writing (2.1) is given in [91]

$$T_{\text{em}} = \frac{e_{\text{ph,U}} i_{\text{s,U}} + e_{\text{ph,V}} i_{\text{s,V}} + e_{\text{ph,W}} i_{\text{s,W}}}{\Omega}, \quad (2.2)$$

where $e_{\text{ph,U}}, e_{\text{ph,V}}, e_{\text{ph,W}}$ are the instantaneous back-EMF, $i_{\text{s,U}}, i_{\text{s,V}}, i_{\text{s,W}}$ are the stator currents in phases U, V, and W, respectively, and Ω is the mechanical angular speed. The effective value of the back-EMF phase voltage can be calculated as [17]

$$E_{\text{ph}} = \frac{k_w \omega N_{\text{ph}} \Phi_{\text{PM}}}{\sqrt{2}}, \quad (2.3)$$

where k_w is the winding factor, N_{ph} is the number of turns in series of the stator phase, Φ_{PM} is the PM flux, and ω is the electrical angular velocity. At first glance, Equation (2.2) provides more information than Equation (2.1) on the parameters involved in the calculation of electromagnetic torque. As can be seen in Equation (2.2), it is possible to increase the machine torque capability by adjusting the stator current or the back-EMF. The stator current adjustment has certain limitations because its significant rise would increase machine losses, while the back-EMF adjustment may be an alternative within a reasonable range (keeping a constant peak flux density value in the stator core and a constant number of turns in the slot). The PM flux Φ_{PM} is constant (neglecting the temperature effect) when a certain PM grade is used in the rotor surface PM structure. Therefore, to increase the back-EMF and torque it is possible to adjust the number of turns N_{ph} and the winding factor k_w as indicated in Equation (2.3). However, ideally, these modifications should not reduce the single conductor cross section to avoid extra winding Joule losses. In this case, the first option can make the machine more expensive, in addition to increasing its mass. Additionally, it can be challenging to implement as the conductor space factor needs to be increased when extra turns are

added within the limited slot area. In the case of the winding factor k_w , it is possible to increase the back-EMF in tooth-coil (TC) SL winding machines and improve the machine performance by adopting asymmetric features in the machine [80], [81]. Furthermore, if the winding factor increases, it is possible to reduce the RMS stator supply current to achieve the same electromagnetic torque because the torque is proportional to the product $E_{ph}I_s$. This can bring considerable savings in the winding material, especially when the machine is large. Finally, this method does not dramatically change the magnetizing inductance of the machine, which helps to keep the same load and overload characteristics of the machine, which is not the case when the number of turns is increased.

2.2 Unequal teeth widths in the TCW

The machine under study consists of a stator with open slots. It enables easier manufacture and assembly of preformed coils. Figure 2.1 shows the slot type alternatives (trapezoidal and rectangular geometries) to employ unequal teeth widths and the equivalent magnetic reluctance in the stator core. The rectangular slot arises from the trapezoidal slot, where the empty triangle-shaped space (in yellow, next to the coil in Figure 2.1) is filled with iron core. When the stator slot is trapezoidal, the magnetic reluctance of the rectangular tooth is higher than the magnetic reluctance of the trapezoidal tooth. Figure 2.2 shows a decrease in the magnetic saturation on the stator teeth when a rectangular slot is selected compared with the trapezoidal slot. Therefore, to avoid a large cogging torque and to reduce core losses, the rectangular slot is chosen.

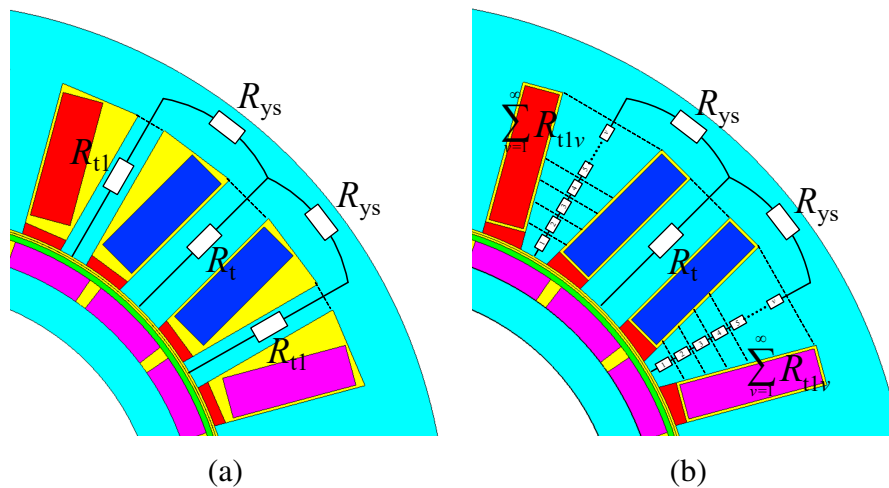


Figure 2.1: Stator slot geometry and teeth reluctances: (a) trapezoidal and (b) rectangular slot.

The coil pitch W in the SL TCW is the distance between the two sides of a coil that coincides with the distance of the stator tooth width that carries a coil b_{ds} and the stator

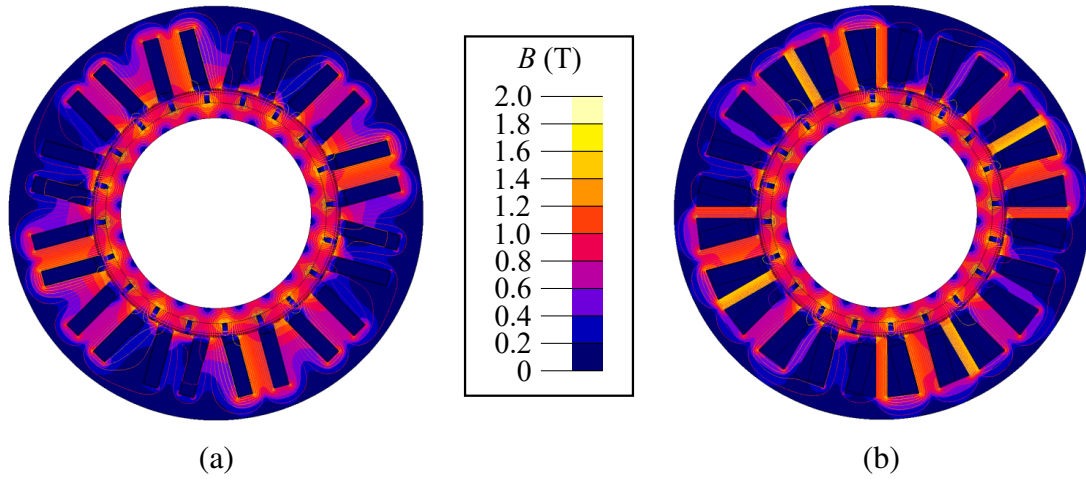


Figure 2.2: Flux density distributions under no-load condition when using (a) trapezoidal and (b) rectangular slot.

slot width b_s as indicated in Figure 2.3. Therefore, by increasing the stator tooth width b_{ds} that carries a coil (the stator slot width b_s is kept constant), increases the coil pitch W .

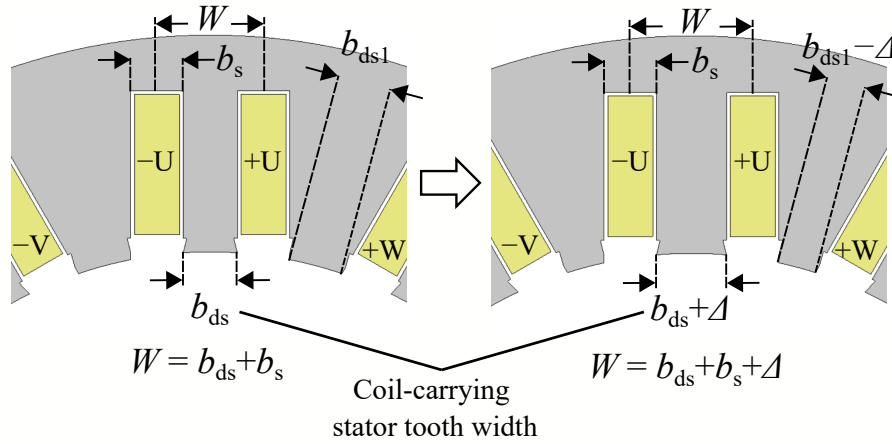


Figure 2.3: Adjustment procedure of the stator tooth inner width b_{ds} .

The winding factor in the SL TCW for the v^{th} harmonic is defined as [8]

$$k_{wv} = k_{pv} k_{dv} k_{sqv}, \quad (2.4)$$

where k_{pv} is the v^{th} harmonic pitch factor, k_{dv} is the v^{th} harmonic distribution factor, and k_{sqv} is the v^{th} harmonic skewing factor. The harmonic pitch factor k_{pv} and the harmonic skewing factor k_{sqv} are expressed as [8]

$$k_{pv} = \sin \left(v \frac{W \pi}{\tau_p 2} \right), \quad (2.5)$$

$$k_{sqv} = \frac{\sin\left(vp\frac{\gamma}{2}\right)}{vp\frac{\gamma}{2}}, \quad (2.6)$$

where τ_p is the pole pitch and γ is the continuous skewing angle. The harmonic distribution factor k_{dv} for $q \leq 0.5$ is 1 if v is odd, and if v is even, $k_{dv} = 0$.

Equation (2.5) reveals that if the coil pitch W is increased (up to $W = \tau_p$), the working harmonic pitch factor k_{pp} can be optimized. Consequently, the winding factor k_{wv} is also improved (keeping the other factors constant). Therefore, by employing this asymmetry it is possible to increase the flux linkage and, thus, improve the torque capability and the induced voltage. To maximize the working harmonic pitch factor k_{pp} , the number of slots must be equal to the number of poles so that $W = \tau_p$; however, this is not possible [8]. Therefore, it is advisable to choose a slot–pole combination where $2p \approx Q_s$. To avoid unbalanced magnetic pull, the greatest common divisor $\text{GCD}(Q_s, 2p)$ should have a high and even value. To reduce the cogging torque, the least common multiple $\text{LCM}(Q_s, 2p)$ should have a high value [92], [93]. The slot–pole combinations that avoid unbalanced magnetic pull and achieve a low cogging torque are those that satisfy $2p = Q_s \pm 2$ [80], [94]. The slot–pole combinations for TCWs where unequal teeth widths can be employed are presented in Table 2.1. This asymmetric feature can also be used in machines with closed or semiclosed slots.


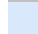

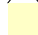
2.3 Permeance distribution in the air gap

The permeance distribution in the air gap is required to calculate important parameters of the PMSM, such as the induced voltage, the cogging torque, and the electromagnetic torque. Furthermore, when employing unequal teeth widths with semiclosed and open slots, the permeance distribution is affected by the slotting effect, and this significantly influences the calculation of the PMSM parameters.

There are several methods to obtain an analytic expression for the permeance. The best-known method is proposed in [95]. This method is relatively simple and easy to implement, and thus, it is widely used in various investigations [96]–[98]. However, this method does not accurately model the slotting effect. Another improved method is also proposed in [99]. This method is more complex to implement but more accurate. These methods involve the use of conformal transformation and numerical analysis and require knowledge of the following parameters of the machine: the stator inner and rotor outer diameters, the slot opening width, and the number of slots. A toolbox software package is available for MATLAB (or OCTAVE), which performs the conformal transformation providing the stator geometry vertices to obtain the complex relative permeance [100]. The key functions used are described in [101], [102]. The latter allows obtaining the permeance distribution quickly with high precision.

Table 2.1: Possible slot–pole combinations to employ unequal teeth widths in the TCW.

$Q_s \backslash 2p$		4	6	8	10	12	14	16	18	20
		q	q	q	q	q	q	q	q	q
6	k_{wp}	0.866		0.866	0.5		0.5	0.866		0.866
	k_{wp}									
9	k_{wp}									
	k_{wp}									
12	k_{wp}			0.866	0.966		0.966	0.866		0.5
	k_{wp}									
15	k_{wp}									
	k_{wp}									
18	k_{wp}					0.866	0.902	0.945		0.945
	k_{wp}									
21	k_{wp}									
	k_{wp}									
24	k_{wp}							0.866		0.966
	k_{wp}									
27	k_{wp}									
	k_{wp}									

-  Invalid configuration.
-  Unbalanced magnetic pull.
-  SL is not feasible.
-  Slot–pole combinations that satisfy $2p = Q_s \pm 2$.

In this doctoral dissertation, the methods presented in [95] and [99] are studied because they are the most commonly used ones in the electrical machine design [103]. The assumptions applied are the following:

- The permeability of the core is infinite.
- The stator slots have an infinite depth.
- The outer diameter of the stator is infinite.

Figure 2.4 shows the 24-slot 20-pole geometry machine used to obtain the permeance distribution with both the methods.

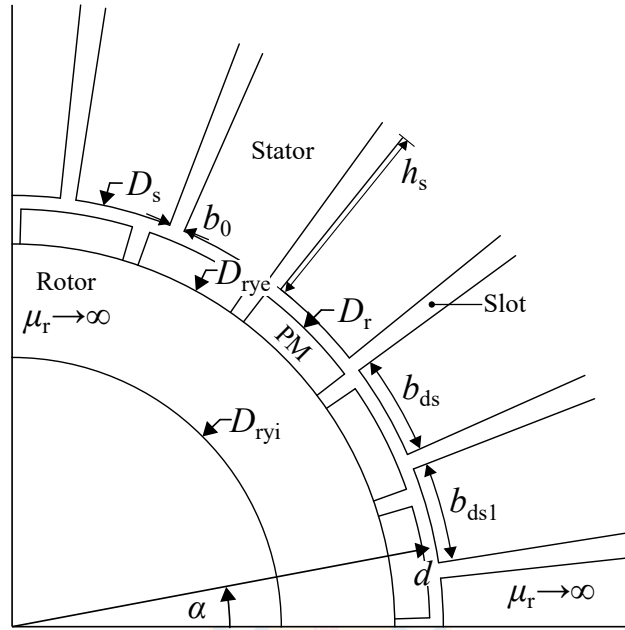


Figure 2.4: Simplified geometry of the machine used to obtain the permeance distribution.

The relative permeance (RP) function is given by [95]

$$\lambda(d, \alpha) = \begin{cases} 1 - \beta(d) - \beta(d) \cos\left(\frac{\pi}{0.8\beta_0}\alpha\right) & 0 \leq \alpha < 0.8\beta_0 \\ 1 & 0.8\alpha_0 \leq \alpha \leq \frac{\tau_s}{2} \end{cases}, \quad (2.7)$$

where d is an arbitrary diameter between the rotor yoke outer diameter D_{rye} and the stator inner diameter D_s , α is the mechanical position, β_0 is the slot opening angle, τ_s is the slot pitch, and β is a function defined as

$$\beta(d) = \frac{1}{2} \left(1 - \frac{1}{\sqrt{1 + \left(\frac{b_0}{2\delta_{ef}}\right)^2 (1 + u^2)}} \right), \quad (2.8)$$

where b_0 is the slot opening width, δ_{ef} is the effective air gap length expressed as

$$\delta_{ef} = \delta + \frac{h_{PM}}{\mu_{r,PM}}, \quad (2.9)$$

where $\mu_{r,PM}$ is the relative permeability of the PM, h_{PM} is the PM height, δ is the air gap

length, and u is a solution of the implicit equation

$$\frac{d}{2} \frac{\pi}{b_0} = \frac{1}{2} \ln \left(\frac{\sqrt{a^2 + u^2} + u}{\sqrt{a^2 + u^2} - u} \right) + \frac{2\delta_{ef}}{b_0} \tan^{-1} \left(\frac{2\delta_{ef}}{b_0} \frac{u}{\sqrt{a^2 + u^2}} \right), \quad (2.10)$$

$$a^2 = 1 + \left(\frac{2\delta_{ef}}{b_0} \right)^2. \quad (2.11)$$

The relative permeance distribution in the air gap of the symmetric machine with a number of slots Q_s obtained from Equation (2.7) can be written in the form of a Fourier series as

$$\lambda(d, \alpha, \alpha_0) = \sum_{v=0}^{N_\lambda} \lambda_v(d) \cos(vQ_s(\alpha - \alpha_0)), \quad (2.12)$$

where α_0 is the reference angle, N_λ is the maximum order of the Fourier coefficients, and λ_v is the Fourier coefficients of the permeance function in the air gap.

The complex permeance (CP) function is given by [99]

$$\lambda(d, \alpha) = \frac{k}{s} \frac{w - 1}{(w - a)^{\frac{1}{2}}(w - b)^{\frac{1}{2}}} = \lambda_a(r, \alpha) + j\lambda_b(r, \alpha), \quad (2.13)$$

where λ_a and λ_b are the real and imaginary parts of the permeance distribution, respectively,

$$k = \frac{D_s}{2} \exp \left[j \left(\frac{\delta'}{\pi} \ln w + \frac{\tau_s}{2} \right) \right], \quad (2.14)$$

$$\delta' = \ln \left(\frac{D_s}{D_{rfe}} \right), \quad (2.15)$$

and

$$s = \frac{d}{2} \exp(j\alpha). \quad (2.16)$$

The value of w is determined from

$$z = \ln(s) = j \frac{\delta'}{\pi} \left(\ln \left| \frac{1+c}{1-c} \right| - \ln \left| \frac{b+c}{b-c} \right| - 2 \frac{b-1}{\sqrt{b}} \tan^{-1} \left(\frac{c}{\sqrt{b}} \right) \right) + C, \quad (2.17)$$

where

$$c = \sqrt{\frac{w-b}{w-a}}, \quad (2.18)$$

$$b = \sqrt{\frac{a}{2\delta'} + \sqrt{\left(\frac{a}{2\delta'}\right)^2 + 1}}, \quad (2.19)$$

$$a = \frac{1}{b}, \quad (2.20)$$

and

$$C = \ln \left(\frac{D_s}{2} + j \left(\frac{\tau_s}{2} + \frac{\alpha_0}{2} \right) \right). \quad (2.21)$$

Equation (2.17) is a nonlinear function, whose solution requires numerical methods. Therefore, it is necessary to find the value of w for a given z for each mechanical position α . The complex relative permeance distribution in the air gap of a symmetric machine with a number of slots Q_s obtained from Equation (2.13) can be expressed in the form of a Fourier series as

$$\lambda_a(d, \alpha, \alpha_0) = \sum_{v=0}^{N_\lambda} \lambda_{av}(d) \cos(vQ_s(\alpha - \alpha_0)), \quad (2.22)$$

$$\lambda_b(d, \alpha, \alpha_0) = \sum_{v=0}^{N_\lambda} \lambda_{bv}(d) \sin(vQ_s(\alpha - \alpha_0)). \quad (2.23)$$

Figure 2.5 shows a comparison of the permeance distributions in the air gap ($d = D_s - \delta$) calculated analytically and by the FEA at different slot opening widths b_0 in a symmetric stator. As can be seen from the figure, there is a good agreement between the FEA and the CP model. However, the RP model neglects the slot edge effect and the imaginary part. On the other hand, it can be seen that the peak-to-peak value of the air gap permeances increases as the value of b_0 increases. Furthermore, as the value of b_0 decreases, the permeance of the real part λ_a will tend to one, and the imaginary part λ_b will approach zero. This means that the RP model can be used when applied in machines with small slot opening widths b_0 .

In the case of an asymmetric stator structure (see Figure 2.3), the permeance distribution in the air gap can be determined from the methods presented above. However, it is not possible to directly calculate the permeance distribution, including unequal teeth widths with Equations (2.12) and (2.22)–(2.23). Therefore, a way to estimate the new permeance is proposed. The sequence of the estimation and a diagram to obtain the new permeance in the air gap are depicted in Figures 2.6 and 2.7, respectively.

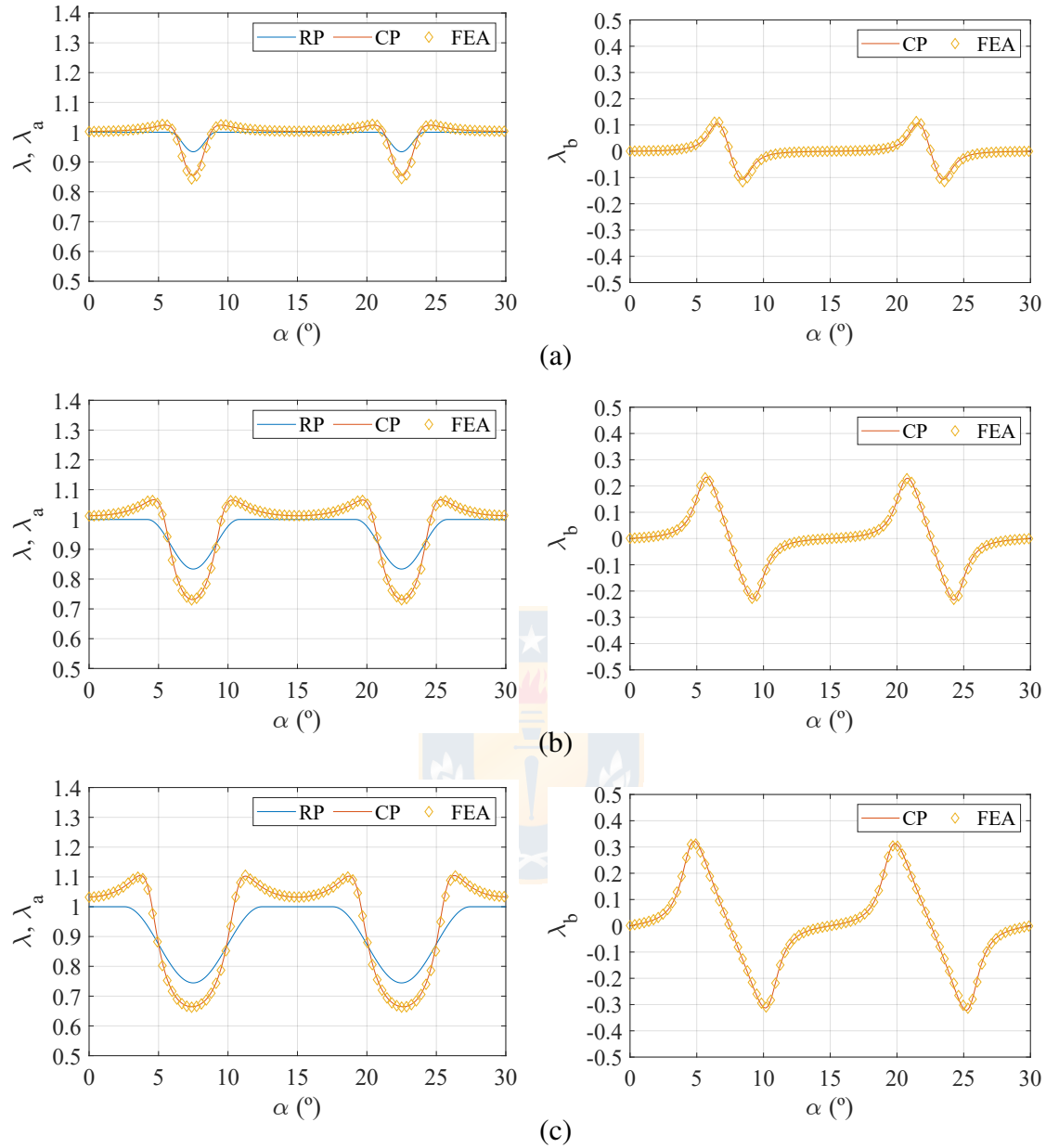


Figure 2.5: Permeance distribution in the air gap of the symmetric stator at different slot opening widths: (a) $b_0 = 4$ mm, (b) $b_0 = 8$ mm, and (c) $b_0 = 12$ mm.

The algorithm to obtain the new permeance distribution is arranged as follows:

- 1) First, obtain the permeance distribution waveforms for a symmetric stator with half of the slots $Q_s/2$ shown in Figure 2.6a.
- 2) Calculate the Fourier coefficients of the permeance distribution in the air gap (λ_{av} and λ_{bv}) obtained for the case of Figure 2.6a.
- 3) With the calculated coefficients, obtain the complex permeance distribution

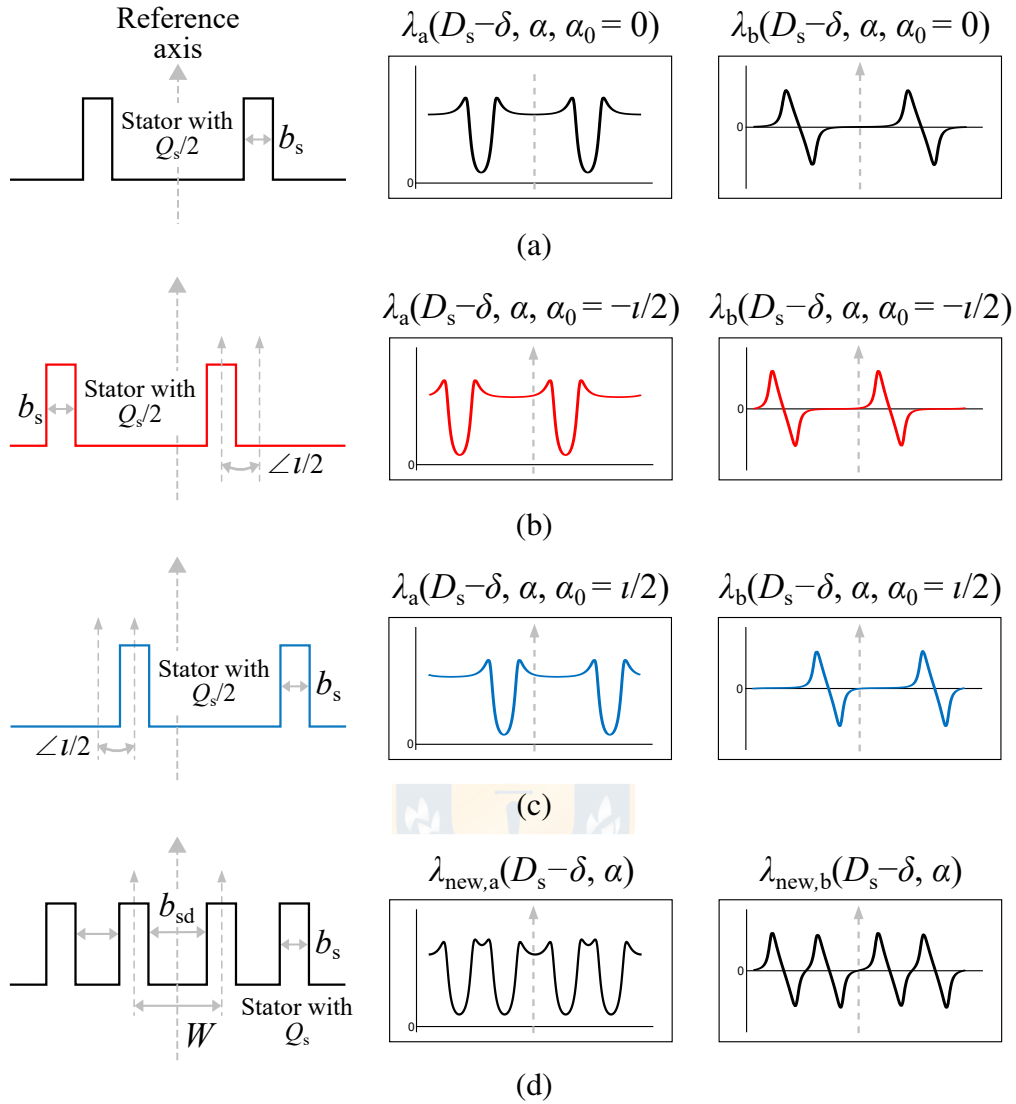


Figure 2.6: Sequence of the estimation of the permeance distribution in the air gap of a TCW PMSM with unequal teeth widths. The angle $\iota = 2\pi / (Q_s/2) - W$ corresponds to the angular displacement between two neighboring slots that carry different phase coils.

waveforms with reference angles equal to $\alpha_0 = -\iota/2$ and $\alpha_0 = \iota/2$, which refer to the slot positions of Figures 2.6b and c, respectively. The new permeance distribution waveforms have an offset from the initial symmetric stator, determined by the new reference angle that coincides with the axis of the tooth that carries a coil around itself. In this way, the asymmetrical position of adjacent slots can be considered.

- 4) By combining the Fourier coefficients of the waveforms derived from Figures 2.6b and c, we can find the overall real and imaginary components of the new permeance

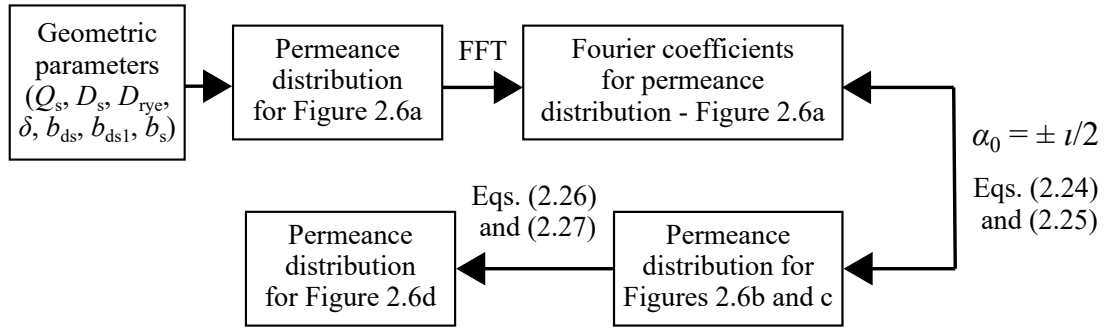


Figure 2.7: Diagram to obtain the permeance distribution in the air gap of a TCW PMSM with unequal teeth widths.

distribution in the air gap of the machine, which can be expressed as

$$\lambda_{\text{new,a}}(d, \alpha) = \lambda_a\left(d, \alpha, -\frac{\iota}{2}\right) \times \lambda_a\left(d, \alpha, \frac{\iota}{2}\right) \quad (2.24)$$

$$\lambda_{\text{new,b}}(d, \alpha) = \lambda_b\left(d, \alpha, -\frac{\iota}{2}\right) + \lambda_b\left(d, \alpha, \frac{\iota}{2}\right) \quad (2.25)$$

- 5) Equation (2.24) corresponds to the multiplication of the real components of the permeance distributions derived from Figures 2.6b and c, which are shifted by ι from each other, and Equation (2.25) corresponds to the sum of the imaginary components of the same permeance distributions.
- 6) Calculate new Fourier coefficients ($\lambda_{\text{new,av}}$ and $\lambda_{\text{new,bv}}$) from the results obtained in the previous step by using a discrete Fourier transform. The waveforms can be expressed in the form of a Fourier series as

$$\lambda_{\text{new,a}}(d, \alpha) = \sum_{v=0}^{N_\lambda} \lambda_{\text{new,av}}(d) \cos\left(v \frac{Q_s}{4} \alpha\right), \quad (2.26)$$

$$\lambda_{\text{new,b}}(d, \alpha) = \sum_{v=0}^{N_\lambda} \lambda_{\text{new,bv}}(d) \sin\left(v \frac{Q_s}{4} \alpha\right), \quad (2.27)$$

where the $1/4$ factor that multiplies the number of slots results from the new waveform period that considers the asymmetry (unequal teeth widths and two stator slots).

To obtain the new permeance with the RP model, the algorithm presented above is valid (not considering the imaginary part of the complex permeance).

The permeance distributions in the air gap obtained by the permeance models and the FEA at different stator tooth inner widths b_{ds} are shown in Figure 2.8. There is a good agreement between the CP model and the FEA results. In contrast, the RP model does not agree well with the CP model and the FEA. This is because the RP model does not accurately model the effect of slots.

As can be seen in Figure 2.8, the permeance distribution in the air gap of TCW PMSMs with unequal teeth widths can be obtained with the proposed method. The results indicate that adjusting the value of b_{ds} changes the spectrum of permeances (see Figure 2.8e), in which new harmonics occur and the values of the existing harmonics are modified.

2.4 Permanent magnet magnetic field

The normal and tangential components of the flux distribution in the air gap produced by PMs mounted on the surface of an inner rotor are given by [104]

$$B_{n,PM}(d, \alpha) = \sum_{v=1,3,5,\dots}^{\infty} K_v(d) f_{B_{n,PM}}(d) \cos(vp\alpha), \quad (2.28)$$

$$B_{t,PM}(d, \alpha) = \sum_{v=1,3,5,\dots}^{\infty} K_v(d) f_{B_{t,PM}}(d) \sin(vp\alpha), \quad (2.29)$$

where

$$K_v(d) = \begin{cases} \frac{\mu_0 M_{PMv}}{\mu_{r,PM}} \frac{vp}{(vp)^2 - 1} \frac{X_1}{Y} & vp \neq 1 \\ \frac{\mu_0 M_{PMv}}{2\mu_{r,PM}} \frac{X_2}{Y} & vp = 1 \end{cases}, \quad (2.30)$$

$$X_1 = \left[\left(vp - \frac{1}{vp} \right) \frac{M_{n,PMv}}{M_{PMv}} + \frac{1}{vp} - 1 \right] + 2 \left(\frac{D_{rye}}{D_r} \right)^{vp+1} - \left[\left(vp - \frac{1}{vp} \right) \frac{M_{n,PMv}}{M_{PMv}} + \frac{1}{vp} + 1 \right] \left(\frac{D_{rye}}{D_r} \right)^{2vp}, \quad (2.31)$$

$$X_2 = \left(2 \frac{M_{n,PM1}}{M_{PM1}} - 1 \right) \left(\frac{D_r}{D_s} \right)^2 - \left(2 \frac{M_{n,PM1}}{M_{PM1}} - 1 \right) \left(\frac{D_{rye}}{D_s} \right)^2 + \left(\frac{D_{rye}}{D_s} \right)^2 \ln \left(\frac{D_r}{D_{rye}} \right)^2, \quad (2.32)$$

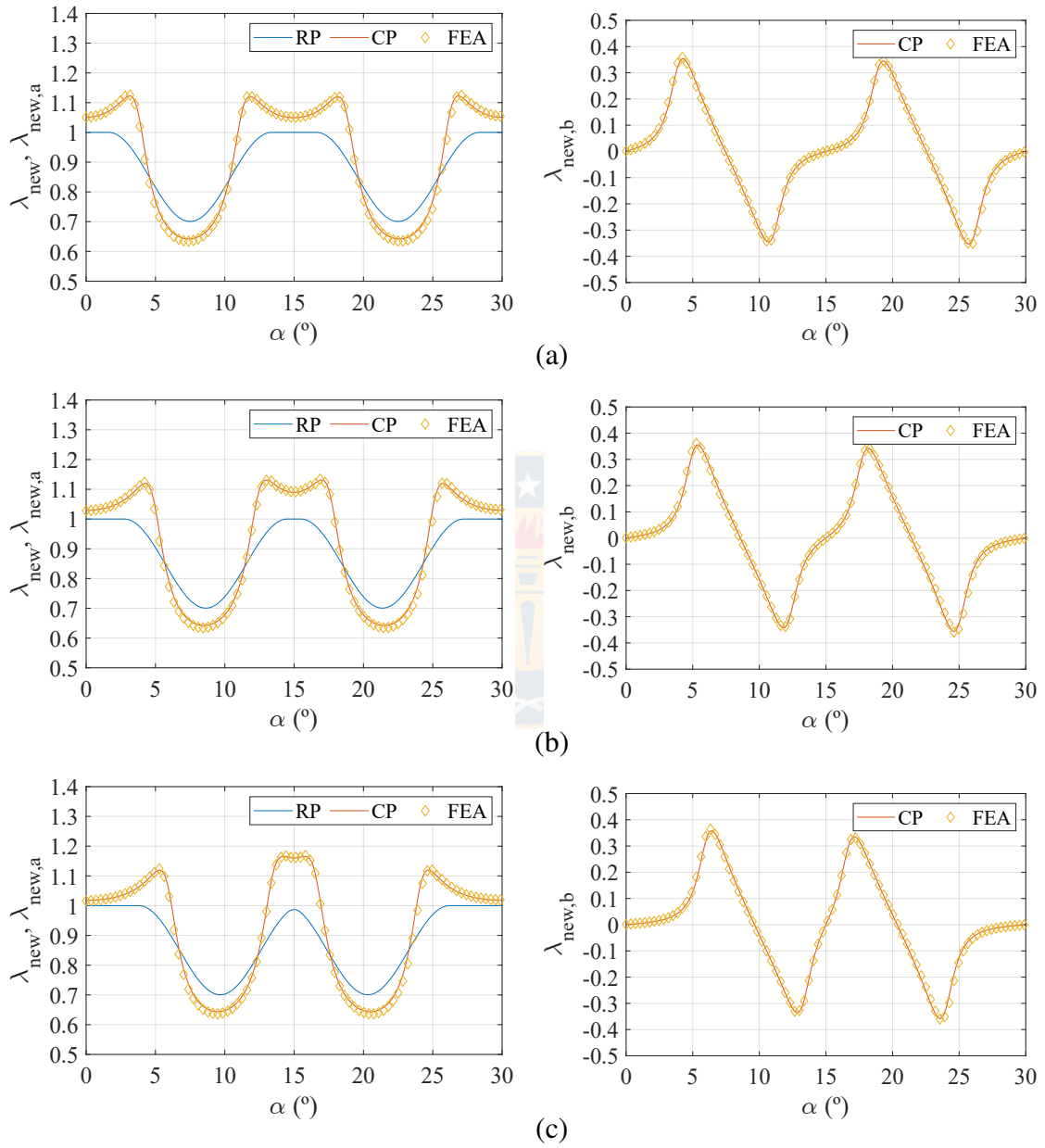


Figure 2.8: Permeance distribution in the air gap at different stator tooth inner widths: (a) $b_{ds} = b_{ds1}$, (b) $b_{ds} = 19$ mm, (c) $b_{ds} = 23$ mm, (d) $b_{ds} = 28$ mm, and (e) their spectra.

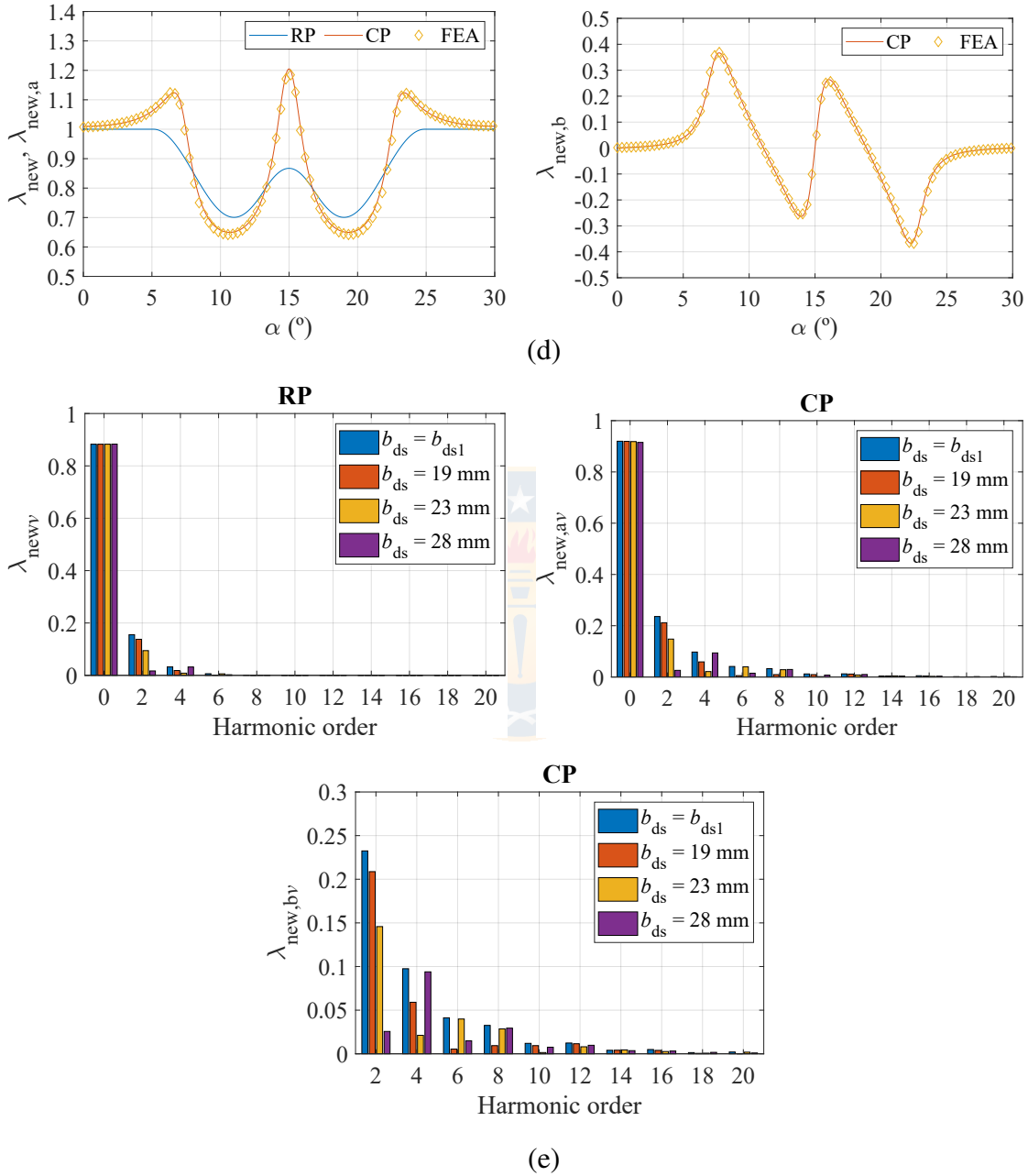


Figure 2.8: Permeance distribution in the air gap at different stator tooth inner widths: (a) $b_{ds} = b_{ds1}$, (b) $b_{ds} = 19$ mm, (c) $b_{ds} = 23$ mm, (d) $b_{ds} = 28$ mm, and (e) their spectra. (cont.)

$$Y = \frac{\mu_{r,PM} + 1}{\mu_{r,PM}} \left[1 - \left(\frac{D_{rye}}{D_s} \right)^{2vp} \right] - \frac{\mu_{r,PM} - 1}{\mu_{r,PM}} \left[\left(\frac{D_r}{D_s} \right)^{2vp} - \left(\frac{D_{rye}}{D_r} \right)^{2vp} \right], \quad (2.33)$$

$$f_{B_{n,PM}}(d) = \begin{cases} \left(\frac{d}{D_s} \right)^{vp-1} \left(\frac{D_r}{D_s} \right)^{vp+1} + \left(\frac{D_r}{d} \right)^{vp+1} & vp \neq 1 \\ 1 + \left(\frac{D_s}{d} \right)^2 & vp = 1 \end{cases}, \quad (2.34)$$

$$f_{B_{t,PM}}(d) = \begin{cases} -\left(\frac{d}{D_s} \right)^{vp-1} \left(\frac{D_r}{D_s} \right)^{vp+1} + \left(\frac{D_r}{d} \right)^{vp+1} & vp \neq 1 \\ -1 + \left(\frac{D_s}{d} \right)^2 & vp = 1 \end{cases}, \quad (2.35)$$

and the parallel magnetization of the PM is expressed as

$$M_{PMv} = M_{PM,nv} + vpM_{PM,tv} \quad (2.36)$$

$$M_{PM,nv} = \frac{B_{r,PM}}{\mu_0} \alpha_{PM} \left\{ \frac{\sin \left[(vp+1) \alpha_{PM} \frac{\pi}{2p} \right]}{(vp+1) \alpha_{PM} \frac{\pi}{2p}} + \frac{\sin \left[(vp-1) \alpha_{PM} \frac{\pi}{2p} \right]}{(vp-1) \alpha_{PM} \frac{\pi}{2p}} \right\}, \quad (2.37)$$

$$M_{PM,tv} = \frac{B_{r,PM}}{\mu_0} \alpha_{PM} \left\{ \frac{\sin \left[(vp+1) \alpha_{PM} \frac{\pi}{2p} \right]}{(vp+1) \alpha_{PM} \frac{\pi}{2p}} - \frac{\sin \left[(vp-1) \alpha_{PM} \frac{\pi}{2p} \right]}{(vp-1) \alpha_{PM} \frac{\pi}{2p}} \right\}, \quad (2.38)$$

where $B_{r,PM}$ is the remanence of the magnet, α_{PM} is the relative PM width, and when $vp = 1$, the second term of Equations (2.37) and (2.38) is replaced by 1.

Therefore, the normal and tangential no-load flux density components in a machine considering the slotting effect are calculated by [99]

$$B_{sn,PM}(d, \alpha, t) = B_{n,PM}(d, \alpha, t) \lambda_{new,a}(d, \alpha) + B_{t,PM}(d, \alpha, t) \lambda_{new,b}(d, \alpha), \quad (2.39)$$

$$B_{st,PM}(d, \alpha, t) = B_{t,PM}(d, \alpha, t) \lambda_{new,a}(d, \alpha) - B_{n,PM}(d, \alpha, t) \lambda_{new,b}(d, \alpha). \quad (2.40)$$

Figure 2.9 presents the waveforms of the no-load normal air gap flux density for different stator tooth inner widths b_{ds} . As shown in the figure, there are discrepancies between the air gap flux density obtained with the RP and CP distributions. However, the normal air gap flux densities obtained with the CP model and the FEA show a good agreement. This

is expected because the permeance results showed that the CP has a good match with the FEA and correctly models the slotting effect.

2.5 Induced voltage

The induced voltage or back-EMF is an important parameter of the PMSM. This parameter provides significant information on the performance of the machine and depends on the distribution shape and amplitude of the normal air gap magnetic field.

The flux linkage in the phase winding can be calculated as [99], [105]

$$\begin{aligned}\psi_{\text{ph}}(t) &= \psi_{\text{ph}}(t) = N_{\text{ph}} l \frac{D_s - \delta}{2} \int_{-W/2}^{W/2} B_{\text{sn,PM}}(d = D_s - \delta, \alpha, t) d\alpha \\ &= \sum_{v_1=1,3,5,\dots}^{\infty} N_{\text{ph}} l \frac{D_s - \delta}{2} k_{\text{sq}v_1} k_{\text{sov}v_1} (X + Y_1 + Y_2) \cos(v_1 p \Omega t),\end{aligned}\quad (2.41)$$

where

$$X = 2\lambda_{\text{new,a}0} B_{\text{sn,PM}v_1} \frac{k_{\text{pv}v_1}}{v_1 p}, \quad (2.42)$$

$$Y_1 = \sum_{v_2=1}^{N_\lambda} (B_{\text{sn,PM}v_1} \lambda_{\text{new,av}2} - B_{\text{st,PM}v_1} \lambda_{\text{new,bv}2}) \cdot \frac{\sin\left[\left(v_1 p + v_2 \frac{Q_s}{4}\right) \frac{W}{2}\right]}{v_1 p + v_2 \frac{Q_s}{4}}, \quad (2.43)$$

$$Y_2 = \sum_{v_2=1}^{N_\lambda} (B_{\text{sn,PM}v_1} \lambda_{\text{new,av}2} + B_{\text{st,PM}v_1} \lambda_{\text{new,bv}2}) \cdot \frac{\sin\left[\left(v_1 p - v_2 \frac{Q_s}{4}\right) \frac{W}{2}\right]}{v_1 p - v_2 \frac{Q_s}{4}}, \quad (2.44)$$

when $v_1 p = v_2 Q_s/4$, the term $(\sin[(v_1 p - v_2 Q_s/4) W/2] / (v_1 p - v_2 Q_s/4))$ should be replaced with $W/2$, and k_{sov} is the slot opening factor, which is expressed as [105]

$$k_{\text{sov}} = \frac{\sin\left(v \frac{\pi b_0}{2 \tau_p}\right)}{\left(v \frac{\pi b_0}{2 \tau_p}\right)}. \quad (2.45)$$

Therefore, the induced voltage per phase can be calculated from the derivative of the flux

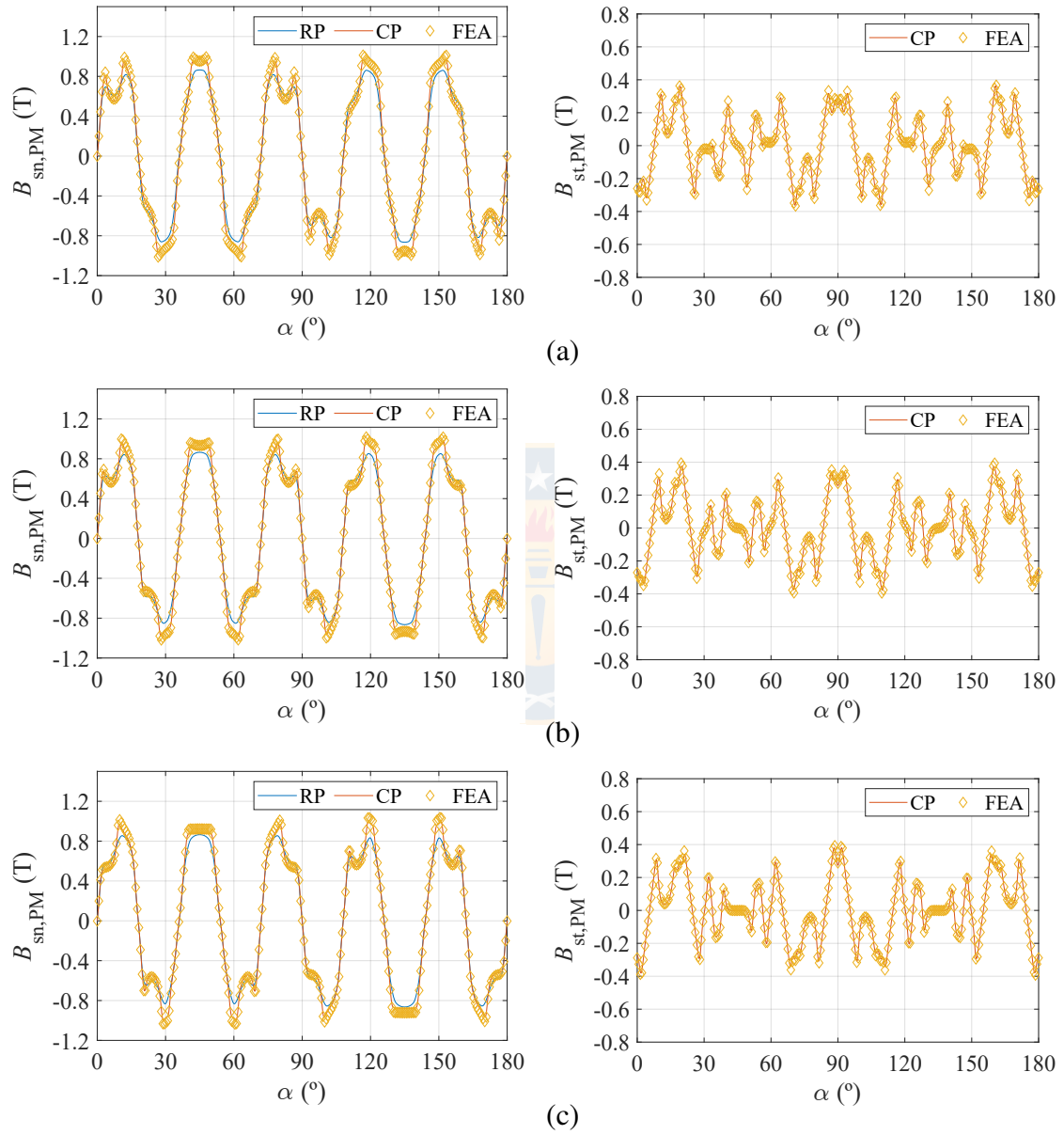


Figure 2.9: Air gap flux density distribution caused by PMs at different stator tooth inner widths: (a) $b_{ds} = b_{ds1}$, (b) $b_{ds} = 19$ mm, (c) $b_{ds} = 23$ mm, and (d) $b_{ds} = 28$ mm, and (e) their spectra.

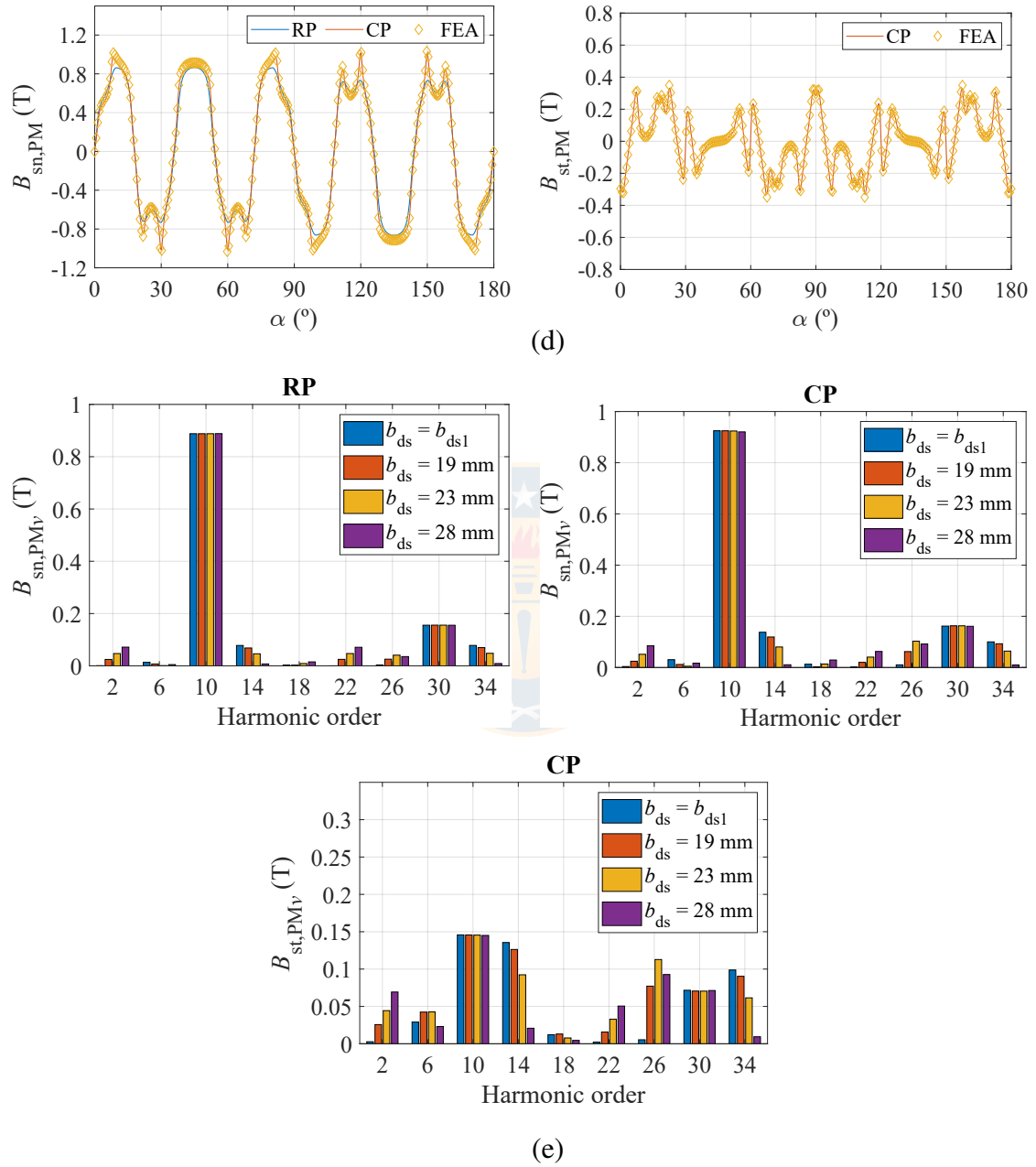


Figure 2.9: Air gap flux density distribution caused by PMs at different stator tooth inner widths: (a) $b_{ds} = b_{ds1}$, (b) $b_{ds} = 19$ mm, (c) $b_{ds} = 23$ mm, (d) $b_{ds} = 28$ mm, and (e) their spectra. (cont.)

linkage per pole as [99], [105]

$$\begin{aligned}
 e_{\text{ph}}(t) &= -\frac{d\psi_{\text{ph}}(t)}{dt} \\
 &= \sum_{v_1=1,3,5,\dots}^{\infty} N_{\text{ph}} l \frac{D_s - \delta}{2} k_{\text{sq}v_1} k_{\text{sov}_1} (Xv_1p + Y_1 + Y_2) \sin(v_1p\Omega t - \theta), \quad (2.46)
 \end{aligned}$$

where θ is zero for phase U, $-2\pi/3$ is for phase V, and $2\pi/3$ is for phase W.

Note that by analyzing Equation (2.46) it is possible to deduce that there are two magnetic fluxes: the base magnetic flux (the first term) and the additional magnetic flux resulting from the interaction between the permeance distribution and the air gap flux density produced by the PMs (the second term). When using closed slots, the additional magnetic flux is neglected, and the air gap flux density distribution is dependent on the flux density caused by the PM field. Therefore, the flux linkage per pole can be optimized based on the pitch factor. When using open slots, the magnetic flux is reduced by the effect of the slots. However, it is possible to increase the value of the flux linkage from the base and additional magnetic fluxes.

The no-load air gap flux density over the 24 slots and 20 poles PMSM with a scaled air gap flux density distribution over the stator tooth containing the coil at different stator tooth inner widths b_{ds} when the permanent magnet faces the stator tooth is presented in Figure 2.10. Note that when the value of b_{ds} is increased, the integration area of the magnetic flux increases (in yellow), including a greater amount of magnetic flux within the tooth region. However, when the coil pitch W is greater than the pole pitch τ_p , the base magnetic flux is reduced because of the opposite flux of the adjacent PM as shown in Figure 2.10d. Despite this, the additional magnetic flux could mitigate the opposite flux and translate the maximum value of the magnetic flux by a single tooth predicted by the pitch factor $W = \tau_p$, which implies $b_{\text{ds}} = 20$ mm. Therefore, it is possible to increase the flux linkage per phase and the induced voltage by adjusting the width of the teeth that carry a coil. The feasible values of b_{ds} are restricted to [106]

$$\frac{\pi D_s}{Q_s/2} \approx b_{\text{ds}} + 2b_s + b_{\text{ds}1}, \quad (2.47)$$

where $b_{\text{ds}1}$ is the width of the tooth that does not carry a coil. However, the performance and manufacturability of the machine has to be verified for each case individually.

The RMS back-EMF value as a function of the stator tooth inner width b_{ds} at the rated speed ($n_N = 80$ r/min) is illustrated in Figure 2.11. The results show a good agreement between the CP model and the FEA when the core permeability is assumed infinite. The RP model presents the same trend as the previous results, but its RMS values are lower

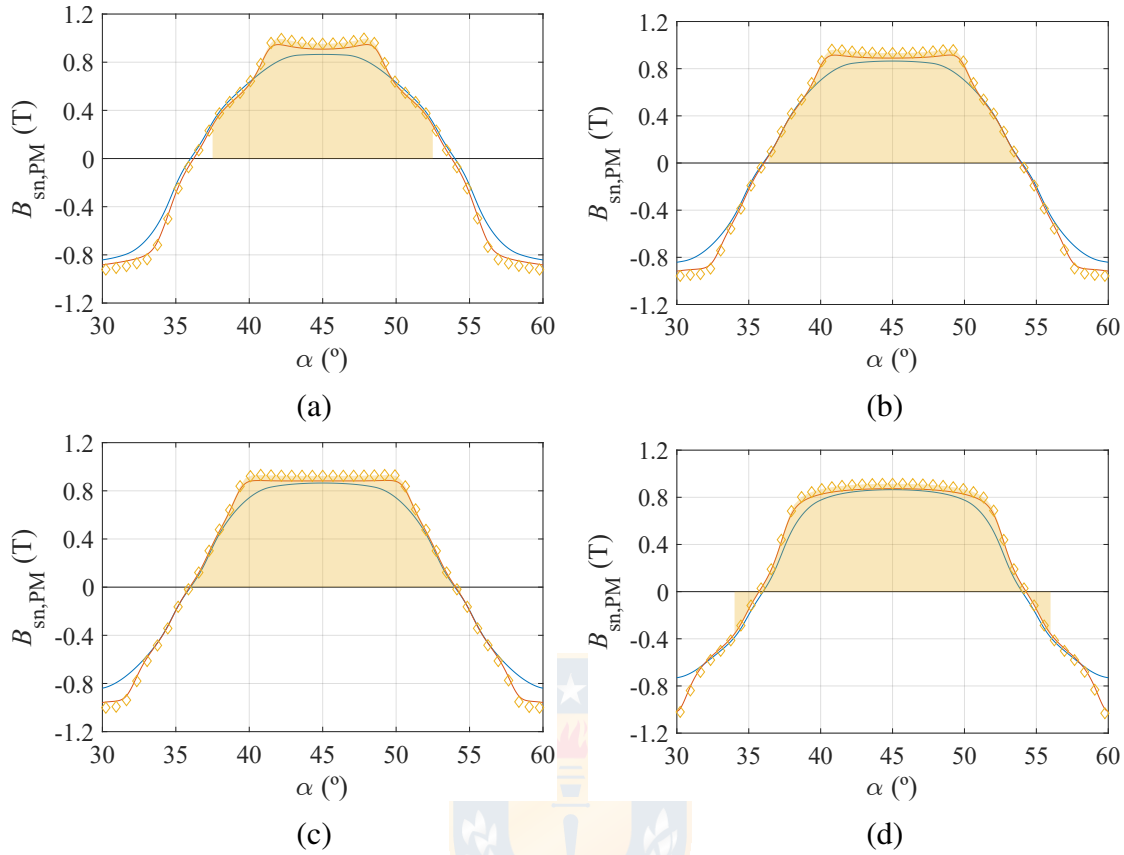


Figure 2.10: No-load normal air gap flux density waveform over the base machine with a scaled air gap flux density distribution over the stator tooth containing the coil at different teeth widths: (a) $b_{ds} = b_{ds1}$, (b) $b_{ds} = 19$ mm, (c) $b_{ds} = 23$ mm, and (d) $b_{ds} = 28$ mm.

than the FEA results. When the magnetic saturation is considered in the FEA, the RMS back-EMF decays faster once it reaches the maximum value ($b_{ds} = 23$ mm). This can be explained by the nonlinear behavior of the magnetic core material. The back-EMF can be adjusted at a higher value of b_{ds} with respect to the symmetric stator ($b_{ds} = b_{ds1}$).

The back-EMF waveforms for different values of b_{ds} at the rated speed ($n_N = 80$ r/min) computed by the FEM are depicted in Figure 2.12. It is pointed out that the waveforms are symmetrical, even though the arrangement of the slots is asymmetric. This can be explained by the use of the theory of the star of slots [107], [108].

The stars of slots for the combination of 24 slots and 20 poles for $b_{ds} = b_{ds1}$ and $b_{ds} > b_{ds1}$ are shown in Figure 2.13. When $b_{ds} = b_{ds1}$ (see Figure 2.13a), the angle between the phasors of two adjacent slots is the electrical angle β_s , which is equal to the mechanical angle multiplied by the number of pole pairs $\alpha_s p$. In this case, the mechanical angle α_s coincides with the coil pitch W as a result of the slot–pole combination. In the second case (see Figure 2.13b), the angle between the phasors of the same coil β_{s1} is different

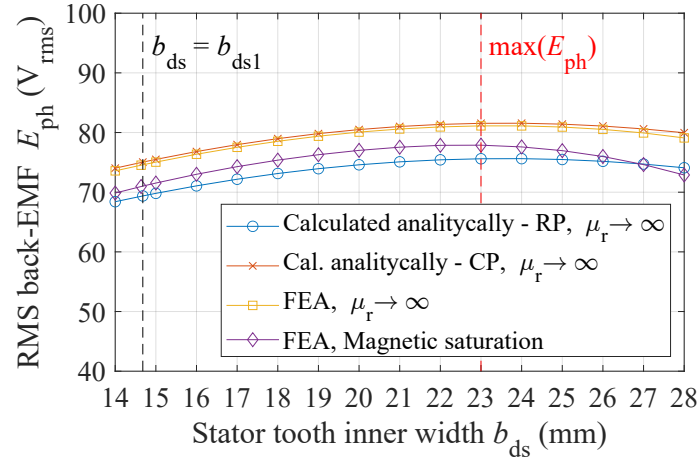


Figure 2.11: RMS back-EMF value at the rated speed calculated by the analytical and FEA models as a function of the stator tooth inner width b_{ds} .

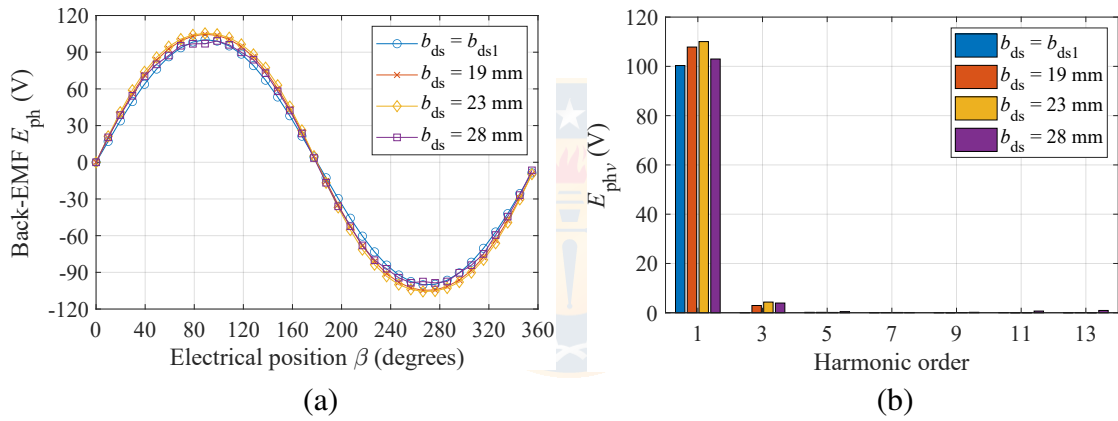


Figure 2.12: (a) Induced voltage waveforms at the rated speed for different stator tooth inner widths b_{ds} and (b) their spectra.

from the angle between the phasors of different coils β_{s2} . The sum of the angles β_{s1} and β_{s2} is constant and corresponds to $2\pi/(Q_s/2)$, which is equivalent to the angular displacement of the unequal teeth widths and two stator slot widths.

The induced voltage of each coil is represented by a phasor in the star of slots. The resulting three-phase induced voltage phasor diagrams for $b_{ds} = b_{ds1}$ and $b_{ds} > b_{ds1}$ are depicted in Figure 2.14, respectively, where the angles between the phases are $2\pi/3$ electrical degrees. It can be seen that the angle between the phasors of the different phases remains unchanged in both cases, which explains the symmetric induced voltage waveforms.

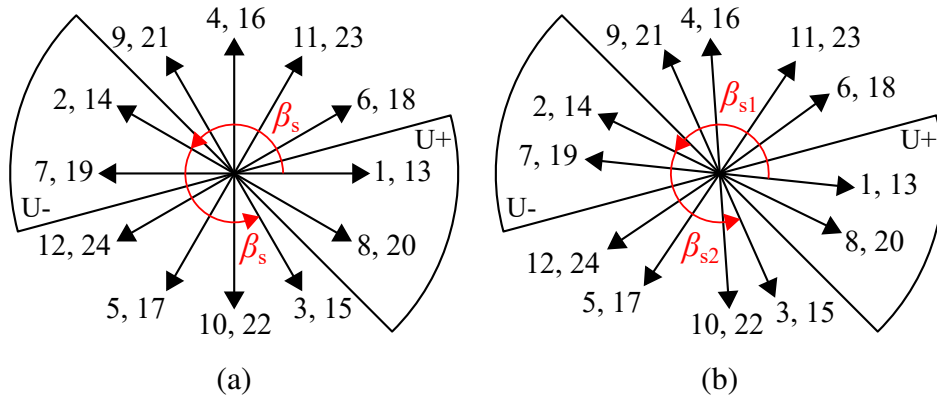


Figure 2.13: Stars of slots of a three-phase 24-slot 20-pole machine for (a) $b_{ds} = b_{ds1}$ and (b) $b_{ds} > b_{ds1}$.

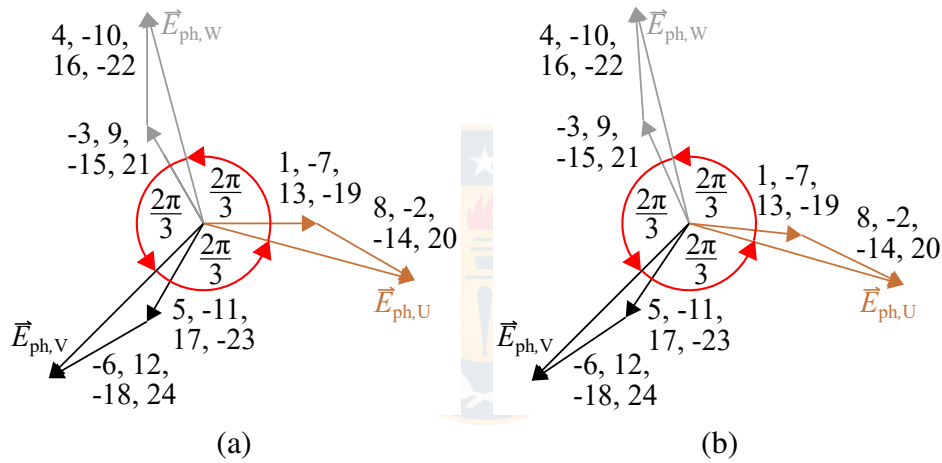


Figure 2.14: Three-phase induced voltage phasor diagram for (a) $b_{ds} = b_{ds1}$ and (b) $b_{ds} > b_{ds1}$.

2.6 Armature reaction field

The normal and tangential components of the magnetic flux density caused by the linear current density of the coil according to Figure 2.15 are expressed as [109], [110]

$$B_{n,AR}(d, \alpha, t) = i(t) \sum_{v_1=1}^{\infty} K_{n,ARv_1}(d) \cos(v_1 \alpha), \quad (2.48)$$

$$B_{t,AR}(d, \alpha, t) = i(t) \sum_{v_1=1}^{\infty} K_{t,ARv_1}(d) \sin(v_1 \alpha), \quad (2.49)$$

where

$$K_{n,ARv_1}(d) = -\frac{\mu_0 4 z_Q}{\pi a d} \left(\frac{D_s}{d}\right)^{v_1} \left(\frac{d^{2v_1} + D_r^{2v_1}}{D_s^{2v_1} - D_r^{2v_1}}\right) \frac{\sin\left(v_1 \frac{b_0}{D_s}\right)}{v_1 \frac{b_0}{D_s}} \sin\left(v_1 \frac{W}{2}\right), \quad (2.50)$$

$$K_{t,ARv_1}(d) = \frac{\mu_0 4 z_Q}{\pi a d} \left(\frac{D_s}{d}\right)^{v_1} \left(\frac{d^{2v_1} - D_r^{2v_1}}{D_s^{2v_1} - D_r^{2v_1}}\right) \frac{\sin\left(v_1 \frac{b_0}{D_s}\right)}{v_1 \frac{b_0}{D_s}} \sin\left(v_1 \frac{W}{2}\right), \quad (2.51)$$

i is the current flowing through the coil, z_Q is the number of conductors in a slot, and a is the number of parallel paths. Therefore, the normal and tangential components of the

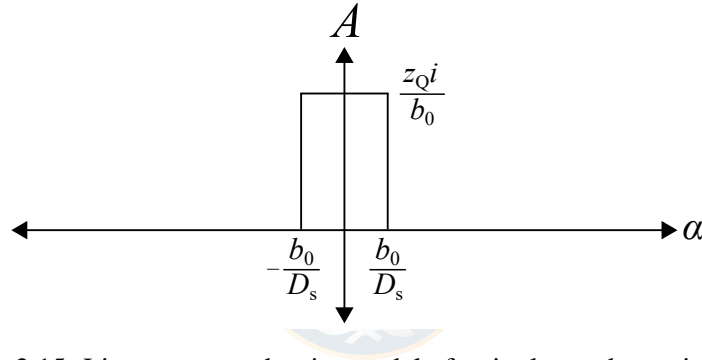


Figure 2.15: Linear current density model of a single conductor in a slot.

flux distribution produced by each phase X can be expressed as

$$B_{n,AR_X}(d, \alpha, t) = \sum_{v_1=1}^{\infty} i_{s,X}(t) K_{n,ARv_1} \left\{ \sum_{v_2=1}^{N_{s_X}} s_{Xv_2} \cos v_2 \left[\alpha - \frac{2\pi}{Q_s} (\alpha_{Xv_2} - 1) - \alpha_0 \right] \right\}, \quad (2.52)$$

$$B_{t,AR_X}(d, \alpha, t) = \sum_{v_1=1}^{\infty} i_{s,X}(t) K_{t,ARv_1} \left\{ \sum_{v_2=1}^{N_{s_X}} s_{Xv_2} \sin v_2 \left[\alpha - \frac{2\pi}{Q_s} (\alpha_{Xv_2} - 1) - \alpha_0 \right] \right\}, \quad (2.53)$$

where the subscript X is phase U, V, or W, s_{Xv_2} and α_{Xv_2} are the sign and position of the phasor per coil v_2 of phase X based on the star of slots theory, respectively, N_{s_X} is the number of elements of s_X and α_X , and α_0 is the reference angle. Therefore, the normal and tangential components of the flux distributions produced by the three-phase winding

can be obtained by linear superposition; thus

$$B_{n,AR}(d, \alpha, t) = B_{n,AR_U}(d, \alpha, t) + B_{n,AR_V}(d, \alpha, t) + B_{n,AR_W}(d, \alpha, t), \quad (2.54)$$

$$B_{t,AR}(d, \alpha, t) = B_{t,AR_U}(d, \alpha, t) + B_{t,AR_V}(d, \alpha, t) + B_{t,AR_W}(d, \alpha, t). \quad (2.55)$$

and considering the slotting effect, these can be written in a similar way as Equation (2.39) and (2.40) by replacing the PM flux densities by the armature reaction flux densities.

In the case for the SL PMSM with the combination of 24 slots and 20 poles, the vectors s_U , s_V , s_W and α_U , α_V , α_W are found from Figure 2.13; thus, they are defined by

$$s_U = \begin{pmatrix} +1 \\ -1 \\ +1 \\ -1 \end{pmatrix} \quad s_V = \begin{pmatrix} -1 \\ +1 \\ -1 \\ +1 \end{pmatrix} \quad s_W = \begin{pmatrix} +1 \\ -1 \\ +1 \\ -1 \end{pmatrix}, \quad (2.56)$$

$$\alpha_U = \begin{pmatrix} 1 \\ 7 \\ 13 \\ 19 \end{pmatrix} \quad \alpha_V = \begin{pmatrix} 3 \\ 9 \\ 15 \\ 21 \end{pmatrix} \quad \alpha_W = \begin{pmatrix} 5 \\ 11 \\ 17 \\ 23 \end{pmatrix}. \quad (2.57)$$

Figure 2.16 shows the air gap flux densities caused by the armature reaction at the rated current. As can be seen from the figure, there is a good agreement between the analytical results and the FEA. However, it is possible to notice discrepancies between the analytical results with the RP model and the FEA because the permeance model does not correctly model the slot edge effect.

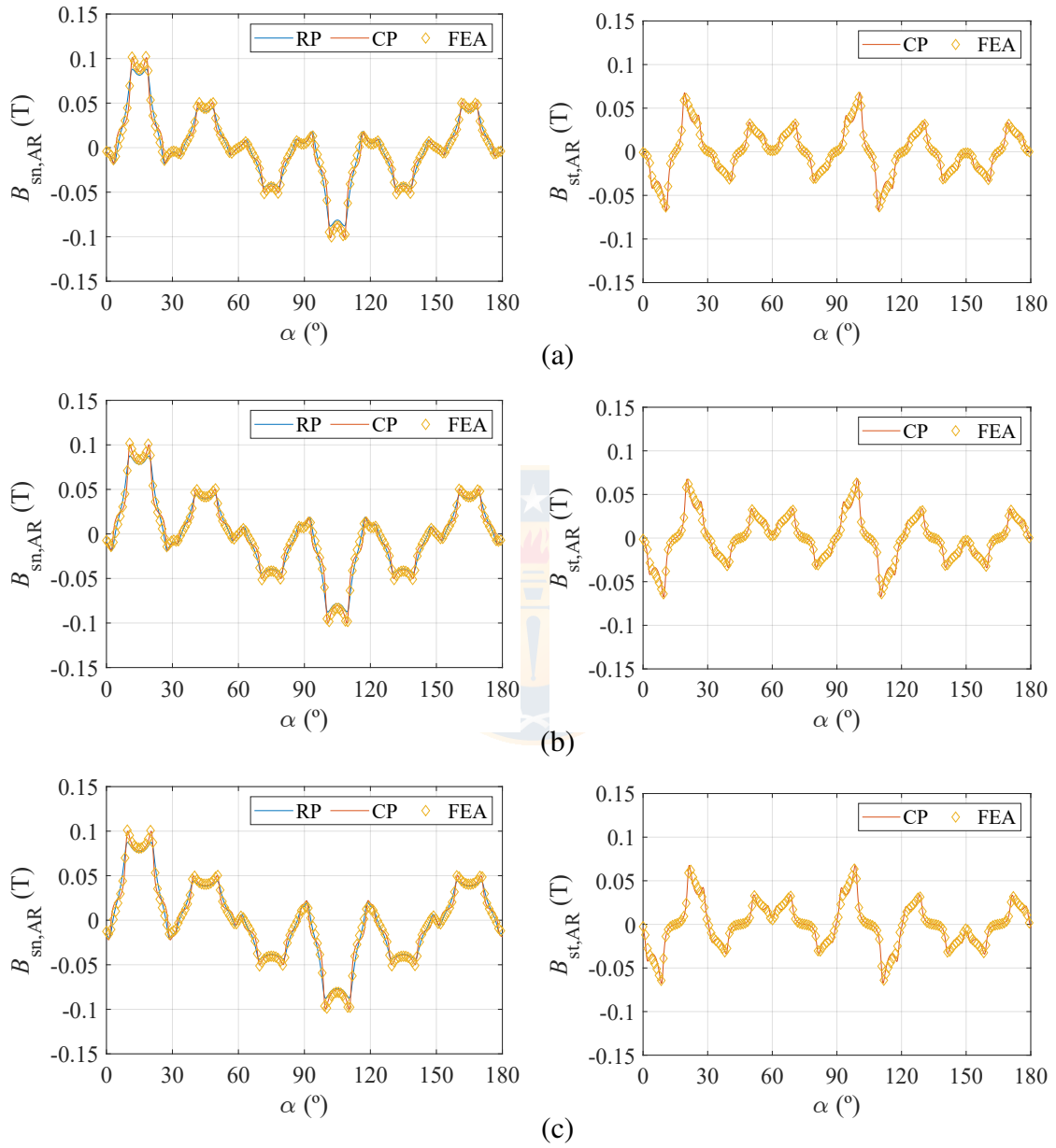


Figure 2.16: Air gap flux density distribution caused by the armature reaction at different stator tooth inner widths: (a) $b_{ds} = b_{ds1}$, (b) $b_{ds} = 19$ mm, (c) $b_{ds} = 23$ mm, (d) $b_{ds} = 28$ mm, and (e) their spectra.

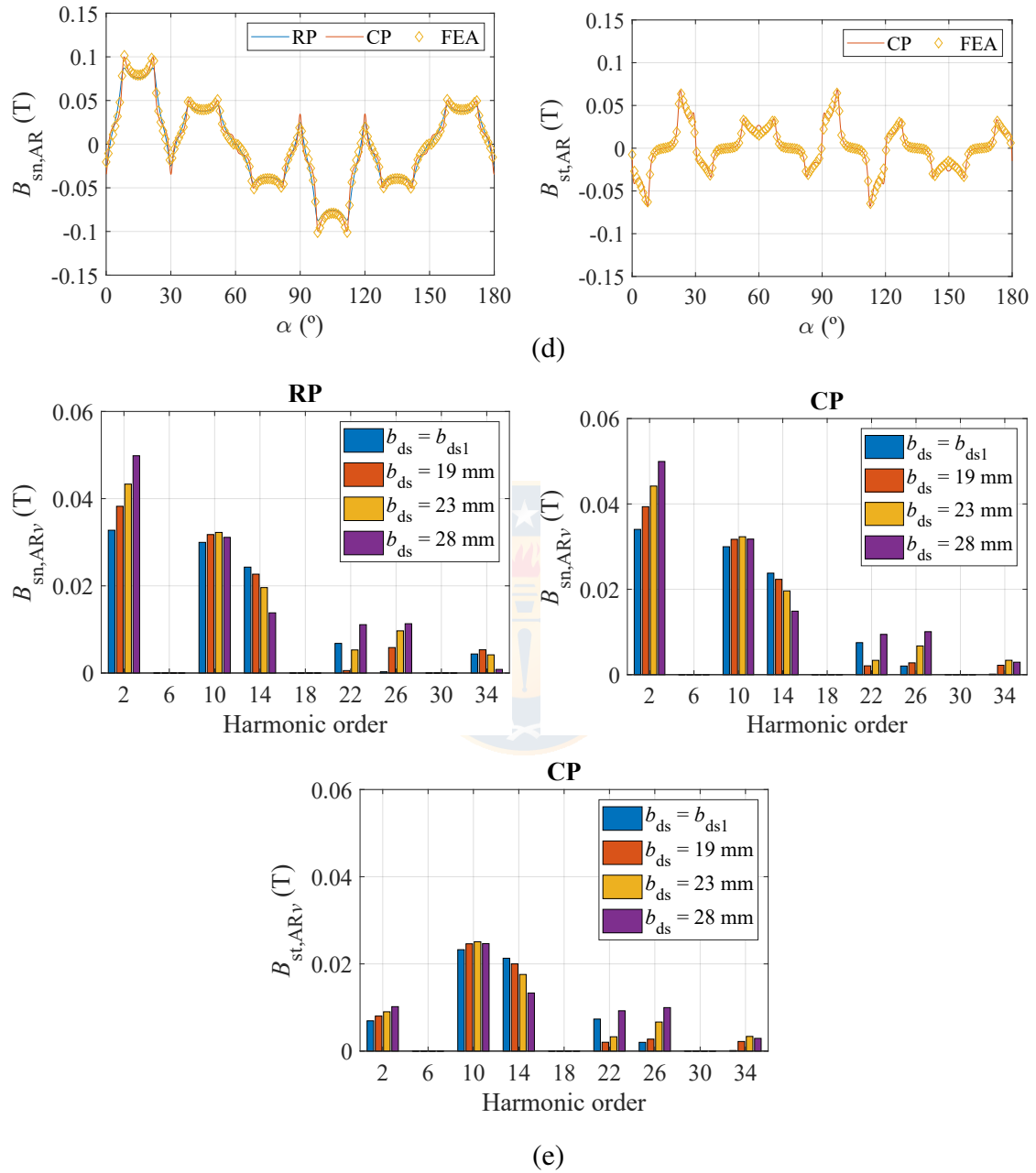


Figure 2.16: Air gap flux density distribution caused by the armature reaction at different stator tooth inner widths: (a) $b_{ds} = b_{ds1}$, (b) $b_{ds} = 19$ mm, (c) $b_{ds} = 23$ mm, (d) $b_{ds} = 28$ mm, and (e) their spectra. (cont.)

2.7 Current linkage and inductance analysis

Current linkage corresponds to the flux-producing ability of the linear current density produced by current in the slots, and this parameter is relevant in the TCW technology because TCWs have high contents of space harmonics in the current linkage waveform. Numerous studies have shown that the current linkage harmonics have an effect on the machine performance [67], [75]–[79], [111]. In this doctoral dissertation, current linkage analysis and the inductance of the machine are introduced in brief, focusing on the stator asymmetric structure.

Current linkage waveform is defined as [75]

$$\Theta(\alpha) = \int_0^{2\pi} A(\alpha) d\alpha, \quad (2.58)$$

where A is the linear current density, and α is the mechanical position.

The winding function is obtained in a similar way to the current linkage, with the difference that only one of the phases is active (by convention, phase U). It is a useful instrument to predict certain performance characteristics of the machine, e.g., mutual coupling between phases [76].

Figure 2.17 shows the winding functions for different stator tooth inner widths b_{ds} . As can be seen, there are slight differences that are not very noticeable. However, if the Fourier decomposition of the winding functions is applied, differences in the spectra can be observed. This first approach suggests that this asymmetric feature could negatively affect the performance of the machine.

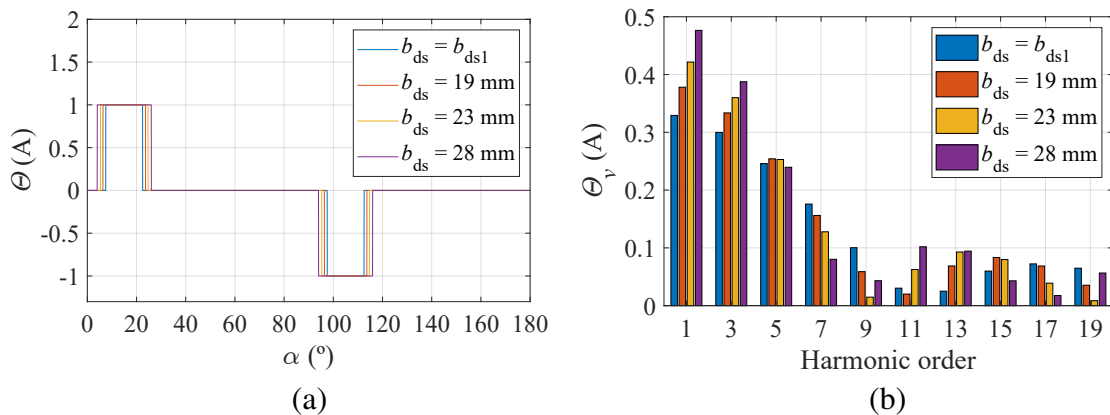


Figure 2.17: (a) Winding function ($b_0 \approx 0$ mm) at the rated speed for different stator tooth inner widths b_{ds} and (b) their spectra.

The mutual coupling factor m_c is calculated as [76]

$$m_c = \frac{\int_0^{2\pi} \Theta_U \Theta_V d\alpha}{\int_0^{2\pi} \Theta_U \Theta_U d\alpha}, \quad (2.59)$$

where Θ_U and Θ_V are the winding functions of phase U and V, respectively. For a symmetric machine with 24 slots and 20 poles, the mutual coupling factor m_c is equal to 0. When using unequal teeth widths (asymmetric stator), m_c is always zero. This can also be verified by the FEA. Figure 2.18 indicates the magnetic flux line when only phase U is supplied for the symmetric stator and having various b_{ds} values. As can be seen in the figure, the magnetic flux is linked only by the coils carrying current. Therefore, it is verified that the asymmetric does not affect the mutual coupling between phases.

Figure 2.19 shows the current linkage for different stator inner teeth widths b_{ds} . It is observed in their spectra that the harmonics amplitude (specifically the working harmonic and subharmonic) varies as a function of the teeth widths that carry coils; this is the reason why it is convenient to examine these harmonics in more detail. Figure 2.20 illustrates the behavior of the working harmonic $v = 5$ and the subharmonic $v = 1$ as a function of b_{ds} . The working harmonic amplitude increases with a higher tooth width carrying a coil until $b_{ds} = 20$ mm and then starts to decrease. This is explained by the fundamental pitch factor as its maximum value is reached when $W = \tau_p$ as mentioned in the previous section. The subharmonic amplitude increases almost linearly with a higher b_{ds} value, which might lead to extra eddy-current losses induced in the rotor. Despite this, it is possible to improve certain characteristics of the machine by using unequal teeth widths as investigated in previous sections. However, it should be considered that there could be an increase in rotor losses (e.g., rotor core and PM).

Another method of winding factor estimation is presented in [112]. It is shown that the harmonic winding factors can be calculated from the winding function by using Fourier decomposition. The harmonic winding factor can be computed as

$$k_{wv} = \frac{h_v}{w_v}, \quad (2.60)$$

where h_v is the v^{th} harmonic amplitude of the winding function, and w_v is the weight of the v^{th} harmonic that is given by

$$w_v = \frac{Q_s}{vm\pi}, \quad (2.61)$$

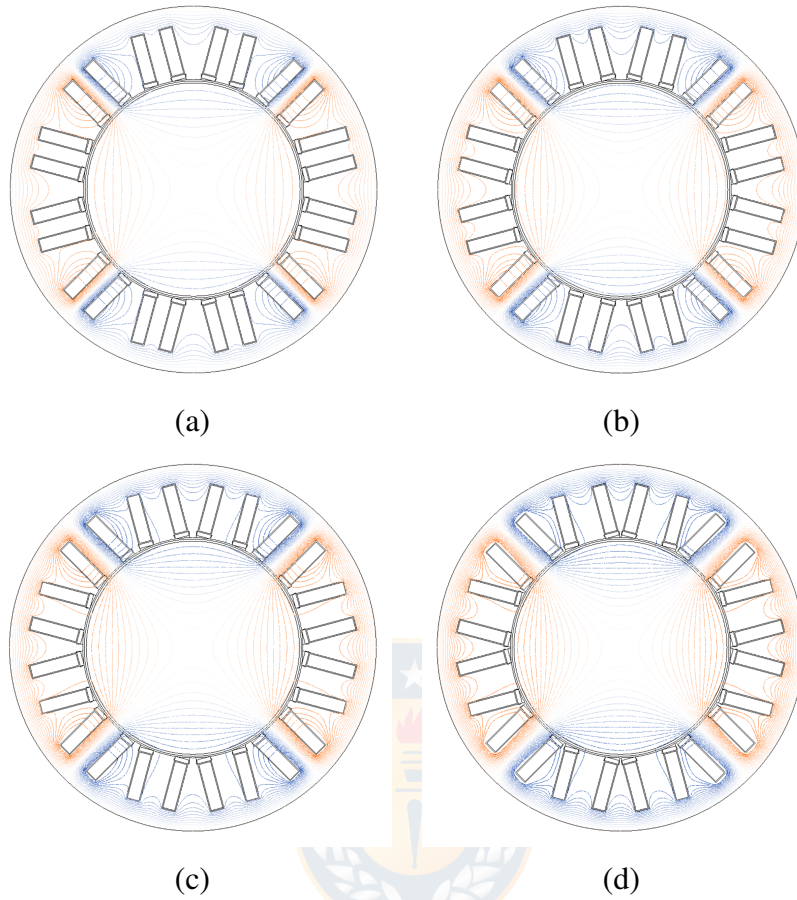


Figure 2.18: Flux plot when only phase U is supplied at different stator inner teeth widths: (a) $b_{ds} = b_{ds1}$, (b) $b_{ds} = 19$ mm, (c) $b_{ds} = 23$ mm, and (d) $b_{ds} = 28$ mm.

where m is the number of phases.

Figure 2.21 shows the spectra of the winding factors for different stator tooth inner widths b_{ds} . As illustrated in the figure, there are nonuniform winding factor distributions when $b_{ds} \neq b_{ds1}$ or $W \neq \tau_p = 20$ mm.

A quality index used in various studies is the air gap harmonic leakage σ_δ . This factor is related to the inductance of the machine and varies according to the slot–pole combination. The air gap harmonic leakage for the three-phase TCW is calculated by [8]

$$\sigma_\delta = \sum_{\substack{v=0 \\ v \neq 3,6,9,\dots \\ v \neq p}}^{+\infty} \left(\frac{k_{wv}}{vk_{wp}} \right)^2. \quad (2.62)$$

As previously discussed, the use of unequal teeth widths has an impact on the winding

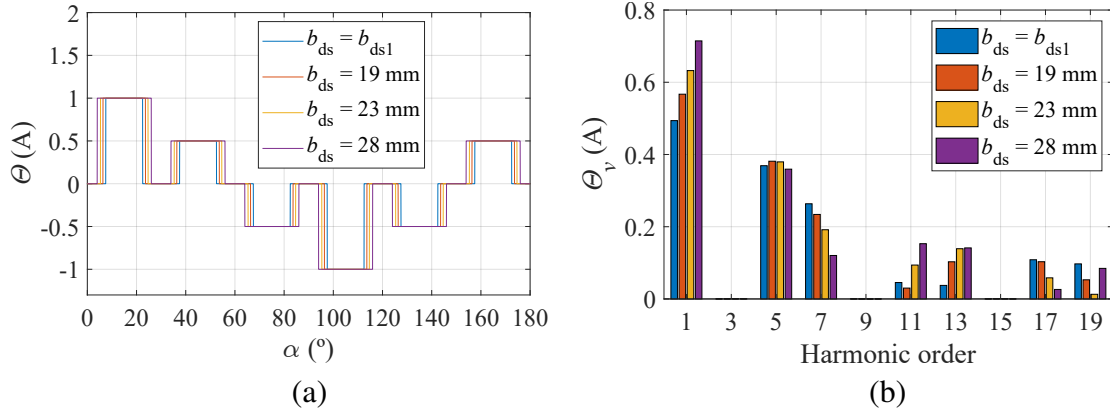


Figure 2.19: (a) Current linkage waveforms ($b_0 \approx 0$ mm) at different stator tooth inner widths b_{ds} and (b) their spectra.

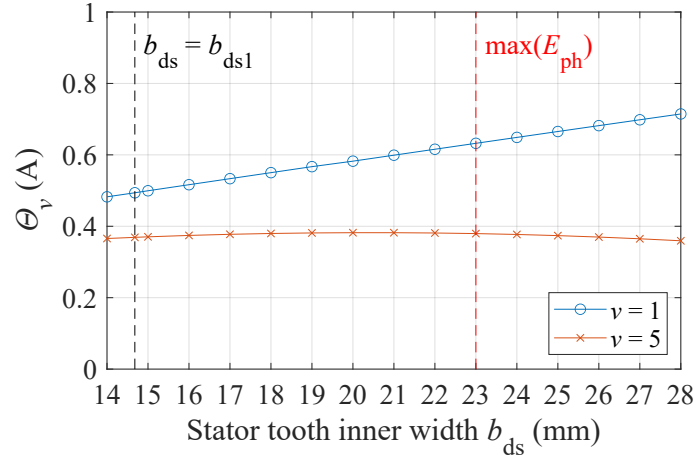


Figure 2.20: Current linkage working harmonic ($v = 5$) and subharmonic ($v = 1$) amplitude ($b_0 \approx 0$ mm) as a function of the stator tooth inner width b_{ds} .

factor, and thus, the air gap harmonic leakage is affected as shown by Equation (2.62). Figure 2.22 shows the air gap harmonic leakage σ_{δ} as a function of the stator tooth inner width b_{ds} . As can be seen in the figure, the air gap harmonic leakage σ_{δ} is not constant. This is explained by the behavior of the amplitude of the winding function harmonics when the value of the tooth width varies.

On the other hand, the synchronous inductance is a significant parameter of the PMSM because it is strongly related to the performance of the machine [76], [113], [114]. This parameter is given by

$$L_s = L_m + L_{\sigma}, \quad (2.63)$$

where L_m is the magnetizing inductance, and L_{σ} is the leakage inductance that is

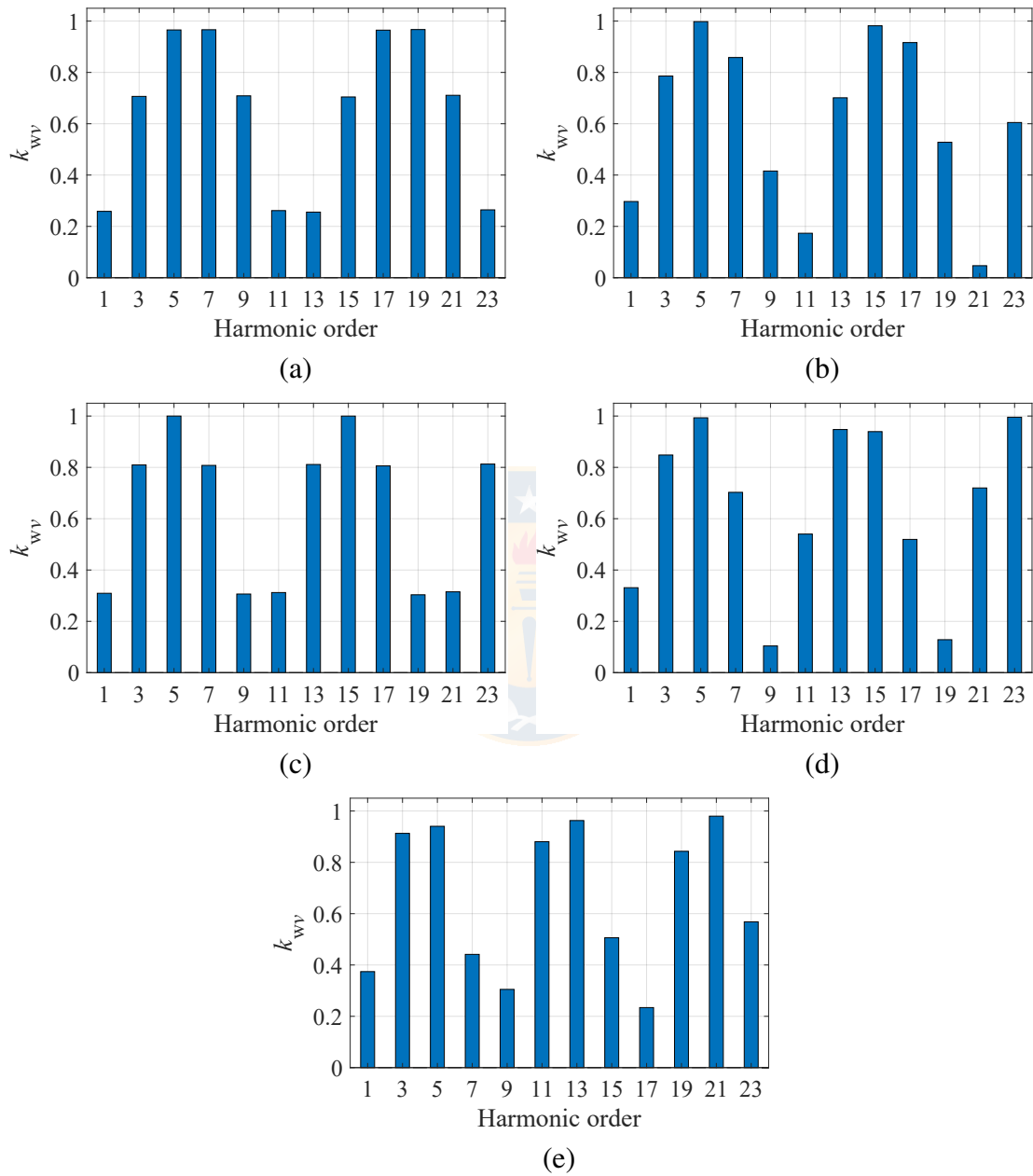


Figure 2.21: Spectra of the winding factors at different stator inner teeth widths: (a) $b_{ds} = b_{ds1}$, (b) $b_{ds} = 19$ mm, (c) $b_{ds} = 20$ mm, (d) $b_{ds} = 23$ mm, and (e) $b_{ds} = 28$ mm.

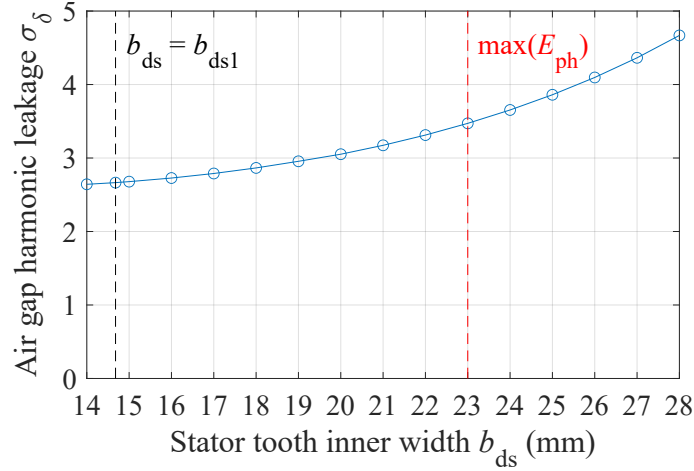


Figure 2.22: Air gap harmonic leakage ($b_0 \approx 0$ mm) as a function of the stator tooth inner width b_{ds} .

expressed as

$$L_{\sigma} = L_h + L_u + L_{tt} + L_{ew} + L_{sq}, \quad (2.64)$$

where L_h is the air gap harmonic leakage inductance, L_u is the slot leakage inductance, L_{tt} is the tooth tip leakage inductance, L_{ew} is the end winding leakage inductance, and L_{sq} is the skew leakage inductance. Equation (2.63) shows that the synchronous inductance is divided into two components. The first term is the magnetizing inductance L_m related to the torque production, and the second term is the leakage inductance L_{σ} that depends on several components that are not involved in the production of torque but that can affect the performance of the machine.

The magnetizing inductance can be written as

$$L_m = \mu_0 \frac{2m\tau_p}{\pi^2 p} \frac{l}{\delta_{ef}} (k_{wp} N_{ph})^2, \quad (2.65)$$

and the air gap harmonic leakage inductance as

$$L_h = \sigma_{\delta} L_m. \quad (2.66)$$

What Equations (2.65) and (2.66) have in common is that they are affected by the unequal teeth widths employed in a TCW PMSM. On the other hand, the magnetization inductance L_m depends on the fundamental winding factor that is modified by the asymmetric stator structure. The air gap harmonic leakage inductance, in turn, depends on the air gap harmonic leakage σ_{δ} that is altered by increasing the teeth widths that carry a coil, as shown in Figure 2.22. However, when taking into account the slot opening width ($b_0 \neq 0$), the air gap harmonic leakage will be reduced as investigated

in [115].

2.8 Torque analysis

The electromagnetic torque is an important parameter of a rotating electrical machine. In the case of the rotor surface PMSM, the shaft torque is generally divided into two components: the electromagnetic torque T_{em} and the cogging torque T_c [91]. The first component can be written as (neglecting the effect of variation of inductance)

$$T_{em}(\alpha) = \frac{dW_f(\alpha)}{d\alpha} = i_s \frac{d\psi_{PM}(\alpha)}{d\alpha}, \quad (2.67)$$

where W_f is the field energy with respect to the mechanical position α . As can be seen in Equation (2.67), this is produced by the interaction of the PMs and the current that flows in the stator winding. The second component is a pulsating torque that is produced by the interaction of the PMs and the stator slots, and it can be calculated as

$$T_c(\alpha) = -\frac{dW_c(\alpha)}{d\alpha}, \quad (2.68)$$

where W_c is the coenergy stored in the air gap with respect to the mechanical position α . The cogging torque T_c causes vibrations, noise, and braking torque [116], [117]. Therefore, it is an undesirable characteristic that can affect the normal operation of the machine and reduce its useful life.

The instantaneous torque (includes all torque components) can be calculated by integrating Maxwell's stress tensor along a circle with a constant diameter d within the air gap region as [118]

$$T(t) = \frac{d^2 l}{4\mu_0} \int_0^{2\pi} B_{sn,PM_AR}(d, \alpha, t) B_{st,PM_AR}(d, \alpha, t) d\alpha, \quad (2.69)$$

where B_{sn,PM_AR} and B_{st,PM_AR} are the normal and tangential components of the flux density produced by the PMs and the armature fields at diameter d , and l is the stator stack length. As can be seen in Equation (2.69), the interaction of flux densities affects the torque produced. In the previous sections, it was investigated that the variation of the tooth width carried by a coil affects the flux density distributions. Thus, it is expected that the torque will also be affected by unequal teeth widths.

Figure 2.23a presents the torque map as a function of the stator tooth inner width b_{ds} and the RMS stator current I_s . The results show that by increasing the tooth width, the electromagnetic torque increases slightly until $b_{ds} = 23$ mm and after that decreases because of the lower magnetic flux. After that, the stator current has to be increased to reach similar electromagnetic torque values. Thus, it is not advisable to choose values

higher than 23 mm for b_{ds} , as it reduces the torque capability and could increase the losses of the machine.

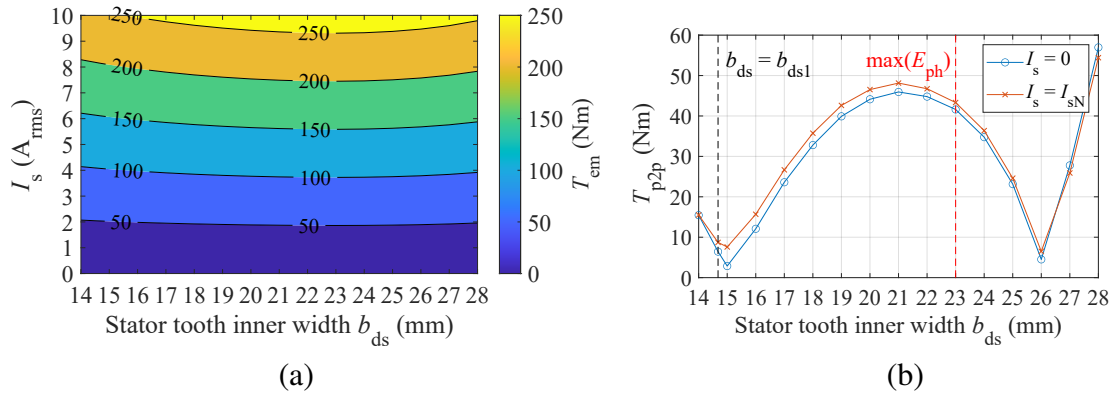


Figure 2.23: Torque performance of the nonskewed PMSM: (a) electromagnetic torque map and (b) cogging torque and torque ripple (peak-to-peak) as a function of the stator tooth inner width b_{ds} .

The torque ripple and cogging torque were evaluated as a function of the stator tooth inner width b_{ds} as shown in Figure 2.23b. The results indicate that the primary source of the torque ripple is the cogging torque. Figure 2.24 shows the cogging torque variation as a function of the stator tooth inner width b_{ds} and its spectra. As Figure 2.24b illustrates, the 6th-order cogging torque harmonic is the strongest harmonic component. However, the fundamental harmonic of the cogging torque in a 24-slot 20-pole PMSM is the 12th-order harmonic, which does not match. This is explained by the asymmetric stator shape.

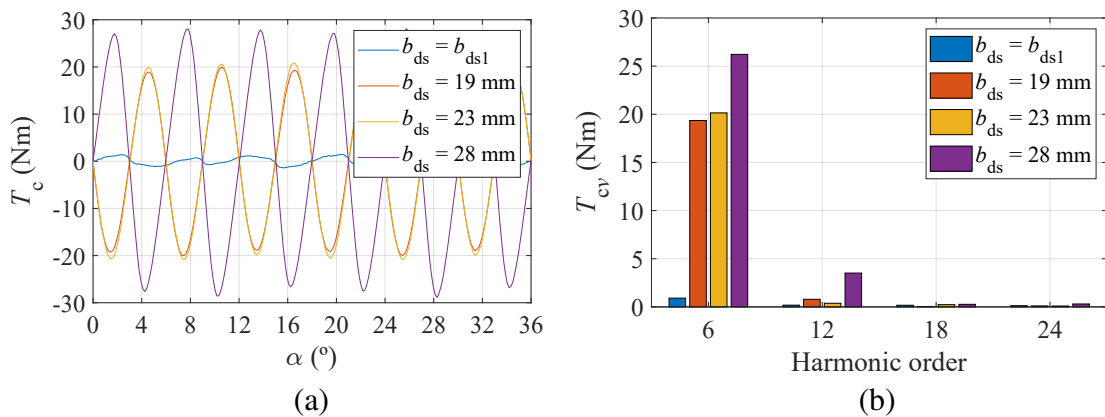


Figure 2.24: (a) Cogging torque variation over one electrical period at different stator tooth inner widths b_{ds} and (b) their spectra (nonskewed rotor).

To eliminate the particular harmonic caused by the asymmetric geometry of the stator, the continuous skew angle to be applied in the rotor or stator is provided by [119]

$$\gamma = \frac{2\pi}{\text{LCM}\left(\frac{Q_s}{2}, 2p\right)}. \quad (2.70)$$

The continuous skew angle to be applied in the 24 slots and 20 poles PMSM with unequal teeth widths is 6 mechanical degrees, which equals to 60 electrical degrees. Figure 2.25 shows the behavior of the torque performance of the skewed machine. It is observed that the electromagnetic torque is reduced in comparison with the nonskewed machine. The cogging torque and torque ripple are decreased because of the 6th-order harmonic reduction as shown in Figure 2.25b and Figure 2.26. However, as seen in Figure 2.26b, the higher order torque ripple harmonics (e.g., 12th) are not eliminated.

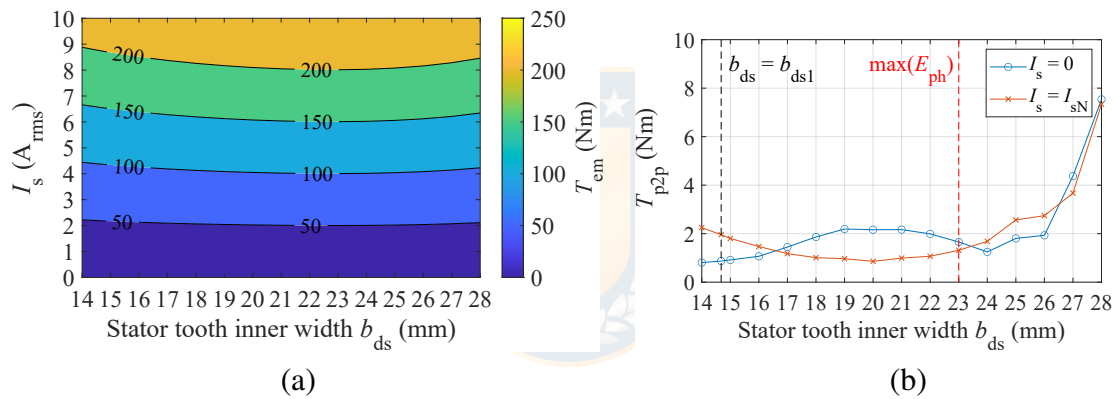


Figure 2.25: Torque performance of the skewed PMSM: (a) electromagnetic torque map and (b) cogging torque and torque ripple (peak-to-peak) as a function of the stator tooth inner width b_{ds} .

2.9 Summary

This chapter has presented an analytical model for a TCW PMSM with unequal teeth widths. The procedure is based on increasing the tooth width that carries coils, keeping the slot width and the machine size constant. The main idea of this asymmetry is to improve the electromagnetic characteristics of the machine by adjusting the coil pitch W . The stator geometry design uses open slots to facilitate manufacture and assembly of the preformed coils; therefore, the slotting effect was considered in the analytical calculations.

The analytical models based on permeance functions most commonly used in the field of electrical machine design were compared. It was found that the CP model has a good

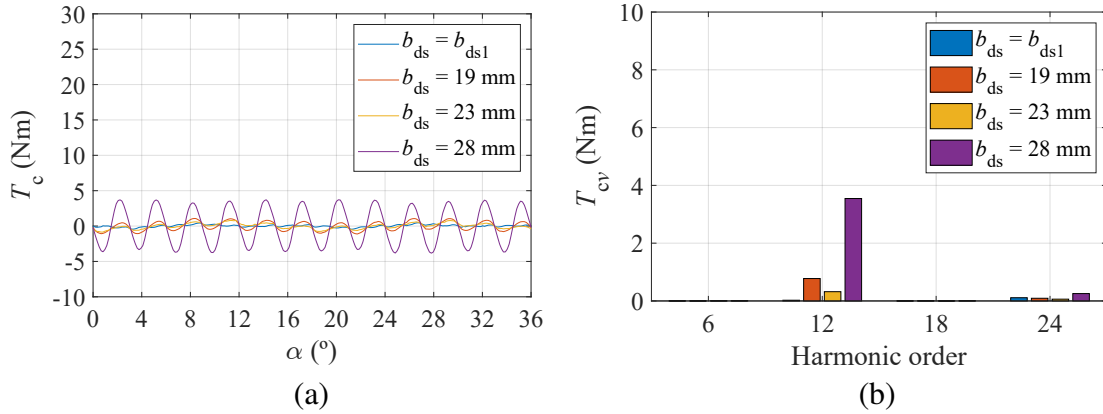


Figure 2.26: (a) Cogging torque variation over one electrical period at a different stator tooth inner width b_{ds} and (b) its spectra (skewed rotor).

agreement with the FEA results compared with the RP model when varying the tooth width. The air gap magnetic field distribution caused by the PMs and the armature reaction obtained with the CP model showed a good agreement with the FEA compared with the RP model. These results were to be expected because the CP model accurately models the effect of the slot in contrast to the RP model. However, the RP model is numerically easier to implement, while the CP model involves solving of more complex expressions. In calculating the induced voltage, the CP model showed a good match with the FEA results.

From the electromagnetic point of view, when increasing the tooth width compared with the original value (symmetric stator), there is an increase in the RMS back-EMF, which was expected. Furthermore, there is a noticeable influence on the calculation of the current linkage distribution and torque when unequal teeth widths are used. From the current linkage results, it was observed that there is an increase in the amplitude of the fundamental harmonic when the same slot current is applied, which is predicted as it is demonstrated by the increase in the induced voltage when increasing the teeth widths that carry a coil. However, the harmful subharmonic is also increased, which would negatively affect the rotor losses and the synchronous inductance. In the torque calculation, the useful torque is increased but the cogging torque and the torque ripple are dramatically affected, requiring the use of minimization techniques for these components. It should be noted that an increase in torque and induced voltage is observed up to $b_{ds} = 20$ mm when $b_0 \approx 0$ mm and up to $b_{ds} = 23$ mm when $b_0 \neq 0$ mm because of the slot opening factor. Therefore, the use of unequal teeth widths in the TCW PMSM is limited to a specific range of values.

3 Loss analysis

Correct computation of machine losses is important in the design and manufacture of an electrical machine. One of the main objectives in the electrical machine design is to minimize the losses of the machine over the whole working region of the machine so that the power consumed is as close to the output power as possible. However, losses are unavoidable. The losses of a PMSM can be divided into two components according to their origin: electromagnetic losses and mechanical losses [8]. The first mainly include winding Joule losses, core losses, and magnet losses, and the second cover the bearing losses, windage losses, and ventilator losses. In this doctoral dissertation, the focus is on electromagnetic losses. The rotational losses are calculated for the machine under study as presented in [8]. According to the results, they are too low (< 1 W), which is due to the low machine speed (≤ 80 r/min), even though the fluid in which the machine is surrounded is water. The resistive torque caused by the water shear drag (or drag torque) can be calculated by

$$T_d = \mu_w \frac{r S_r v}{\delta} = \mu_w \frac{r 2\pi r l \Omega r}{\delta}, \quad (3.1)$$

where r is the mean radius of the air gap, S_r is the rotor wetted area, v is the rotor surface linear speed, Ω is the rotor angular velocity, δ is the gap length, and μ_w is the dynamic viscosity of water 8.90×10^{-4} Pa · s. With the PMSM dimensions $D_r = 0.1971$ m, $l = 0.3$ m, $\delta = 0.0035$ m, and $\Omega = 8.36$ rad/s, $T_d = 0.004$ Nm and drag losses of $P_d = 0.0336$ W are obtained; therefore, the drag losses are neglected.

3.1 Winding Joule losses

The winding Joule losses are calculated by [8], [71]

$$P_{Cu} = k_R Q_s z_Q^2 \rho_{Cu} \left(\frac{l + l_w}{S_{slot} k_{Cu}} \right) I_s^2, \quad (3.2)$$

where k_R is the resistance factor, Q_s is the number of slots, z_Q is the number of conductors in one slot, l is the stator stack length, ρ_{Cu} is the copper resistivity at the operating temperature, k_{Cu} is the copper space factor, and l_w is the end winding length, provided by [120]

$$l_w \approx \frac{b_{ds} + W + b_s}{2}, \quad (3.3)$$

where b_s is the slot width and W is the coil pitch. As observed in Equation (3.3), the end winding length depends on the width of the stator teeth that carry a coil. Therefore, by increasing the stator tooth inner width b_{ds} , the winding Joule losses are increased. This is easy to verify by dividing the copper losses at $b_{ds,new}$ and the copper losses at $b_{ds,in}$

where $b_{ds,new} > b_{ds,in}$, and thus

$$\frac{P_{Cu,new}}{P_{Cu,in}} \approx \frac{l + l_{ew,in} + 2\Delta}{l + l_{ew,in}} \Rightarrow P_{Cu,new} \approx P_{Cu,in} + \frac{2\Delta}{l + l_{ew,in}} P_{Cu,in}, \quad (3.4)$$

where Δ is the increment of the tooth width ($b_{ds,new} - b_{ds,in}$).

Additional AC winding losses caused by the proximity effect are investigated in [121]. They can be incorporated into the calculation of the winding Joule losses; however, in this work, the fundamental stator frequency is low ($f_{sN} = 13\frac{1}{3}$ Hz), and thus, they can be neglected in this case.

3.2 Stator core losses

A typical method for calculating the laminated stator iron losses over an electric period is applied by using the following expression [12], [122]

$$P_{Fe} = \sum_{n=1}^N k_{Fe} \left(\begin{array}{l} k_h \hat{B}_n^2 f A_n l + k_{ec} \frac{1}{T} \int_0^T \left(\frac{dB_n}{dt} \right)^2 A_n l dt + \\ k_{exc} \frac{1}{T} \int_0^T \left(\frac{dB_n}{dt} \right)^{1.5} A_n l dt \end{array} \right), \quad (3.5)$$

where k_{Fe} is the iron space factor, k_h is the hysteresis loss coefficient, k_{ec} is the eddy-current loss coefficient, k_{exc} is the excess loss coefficient, f is the electrical frequency, A_n is the area of the n^{th} stator element, \hat{B}_n is the maximum flux density in the n^{th} stator element, B_n is the instantaneous flux density in the n^{th} stator element, and N is the number of elements in the stator core. The first term of Equation (3.5) corresponds to the static hysteresis losses of the laminated steel, the second term to the dynamic eddy-current losses, and the third term to the excess losses.

The procedure for calculating iron losses requires knowledge of the core loss coefficients. These coefficients can be estimated by fitting the material curves of the core loss density as a function of flux density at various frequencies [123], [124]. However, the 430SS core loss curves were not available during the development of this work. Therefore, a nonconventional method to compute the iron losses was used. To simplify the stator core loss calculation, the excess losses are neglected, and the eddy-current loss coefficient is calculated as [125], [126]

$$k_{ec} = \frac{d^2}{12\sigma_{Fe}}, \quad (3.6)$$

where d is the lamination thickness, and σ_{Fe} is the conductivity of the stator core material. The hysteresis losses can be estimated from the energy density of the stator elements. This can be accomplished by applying the Jiles–Atherton (JA) hysteresis

model [127], [128]. It is used to calculate minor and major hysteresis loops from the material tensor parameters based on the measured hysteresis loops. This approach is incorporated in the simulation software used in this study (Flux by Altair). Figure 3.1 depicts a flowchart that outlines the main steps to calculate the hysteresis losses in the stator.

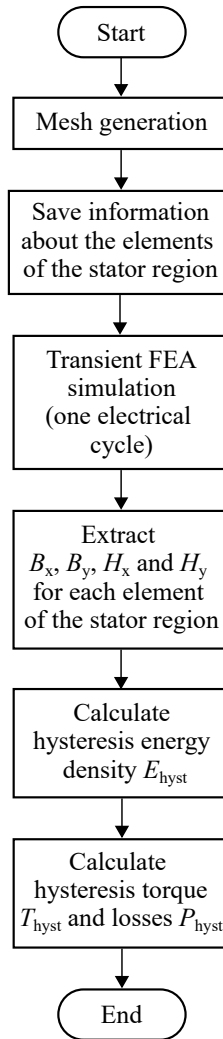


Figure 3.1: Flowchart of the procedure for calculating hysteresis torque and losses.

The hysteresis energy density for each element of the stator magnetic domain over one electrical cycle can be expressed as [125]

$$E_n = \oint H_{xn} dB_{xn} + \oint H_{yn} dB_{yn}, \quad (3.7)$$

where H_{xn} and H_{yn} are the x and y components of the magnetic field strength on the n^{th}

stator element, and B_{xn} and B_{yn} are the x and y components of flux density on the n^{th} stator element. The flux density, magnetic field strength, and position information of the stator nodes are extracted for each time step. The static hysteresis torque can be calculated as

$$T_{\text{hyst}} = \frac{p}{2\pi} k_{\text{Fe}} \sum_{n=1}^N E_n A_n l, \quad (3.8)$$

and the static hysteresis loss is given by

$$P_{\text{hyst}} = T_{\text{hyst}} \Omega. \quad (3.9)$$

The eddy-current losses can be computed with the second term of Equation (3.5) and Equation (3.6) based on the information that was extracted during the calculation of the hysteresis losses. The parameters related to the calculation of the eddy-current losses are provided by the steel manufacturer. The accuracy of the iron loss calculation depends on the mesh quality, which is presented in Figure 3.2 for the machine under study.

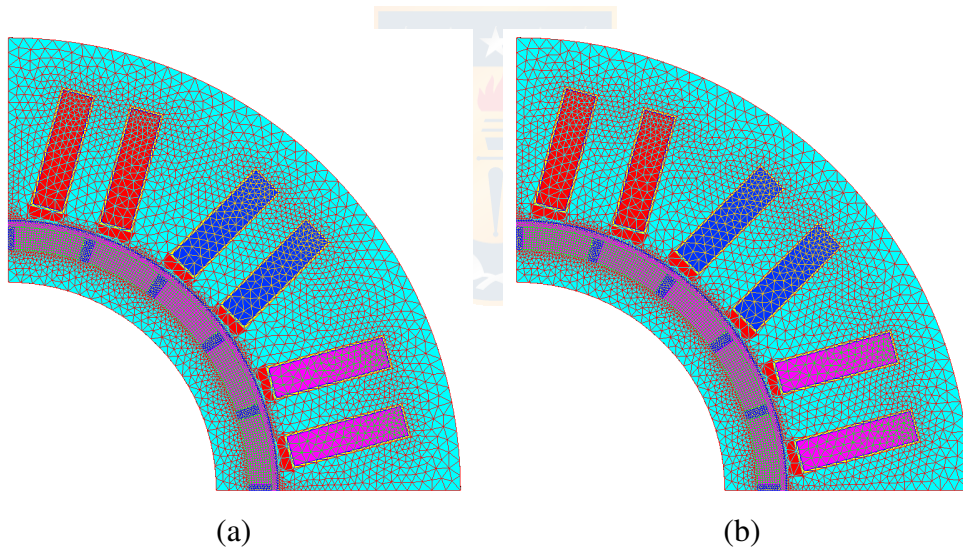


Figure 3.2: Mesh of the 24-slot 20-pole TCW PMSM for (a) $b_{ds} = b_{ds1}$ and (b) $b_{ds} = 19$ mm. The stator mesh adjusts for each value of b_{ds} .

The hysteresis torque is resistive torque that tries to retard the movement of the machine [129], [130]. To explain the origin of the hysteresis torque in a PMSM, a stator tooth and two magnets are considered, as illustrated in Figure 3.3. Initially, it is assumed that the magnetization of the stator tooth is opposite to that of the magnet facing it (see Figure 3.3a). When the rotor starts to rotate, the magnets begin to change their position and move away from the observed stator tooth (see Figure 3.3b). Then, the flux density in the tooth starts to decrease because of the away-moving first magnet and the closer-moving second magnet, but the direction of magnetization of the tooth is maintained because of the BH curve of the material. As a result, an attractive force

between the stator tooth and the first magnet is sustained, but there is also a repulsive force between the stator tooth and the second magnet, see Figure 3.3c. This phenomenon is repeated along the stator, generating as a result an opposite force with respect to the movement. This produces the hysteresis torque in a PMSM. As shown in Figure 3.3, the process of magnetization and demagnetization of the material depends on the hysteresis loop. Therefore, the energy dissipated as a result of this phenomenon will depend on the size of the area of the hysteresis loop. This means that if the coercive force of the hysteresis loop H_c is high, a significant hysteresis torque is expected.

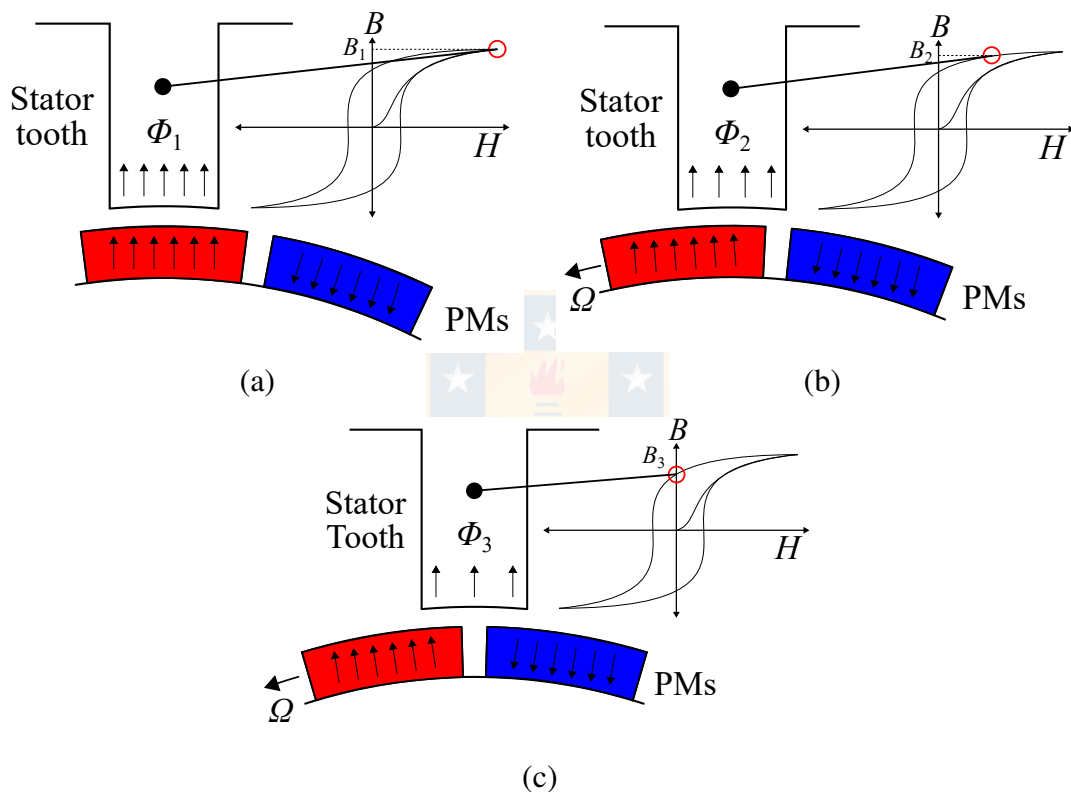


Figure 3.3: Hysteresis phenomenon. The flux density of the PM is fixed and the flux density in the tooth changes as the PMs rotate.

It should be kept in mind that if the hysteresis torque is large, it affects the overall output torque. In the previous chapter, the electromagnetic torque was calculated neglecting the hysteresis torque, the torques caused by eddy-currents, and the friction. Therefore, in this chapter, the performance analysis of the machine will take into account these resistive torques.

3.3 Rotor losses

The rotor losses in the TCW PMSM are mainly affected by the high spatial harmonic content of the current linkage waveform caused by the winding configuration and the

slotting effect. The current linkage harmonics move asynchronously with respect to the rotor, inducing currents in the conductive parts of the rotor [77], [131].

There are several ways to calculate rotor losses. In [13], a method to estimate the solid rotor core losses was presented. As shown, the rotor core losses depend mainly on the flux density caused by the armature reaction. Furthermore, it was mentioned that by applying a high number of poles, it is possible to reduce the rotor eddy-current losses compared with a smaller number of poles because of the reduced peak values of the flux density harmonics. In [132], an analytical model to predict the PM eddy-current losses was introduced. Similar to the study of rotor losses, PM eddy-current losses depend on the flux density distribution. In this doctoral dissertation, the rotor eddy-current losses were calculated in the FEA as [79]

$$P_{\text{rot}} = \int_V \frac{J^2}{\sigma} dV, \quad (3.10)$$

where J is the current density induced in the solid material, and σ is the material conductivity. In the case of the FEA software used in this work (Flux by Altair), the rotor losses can be calculated by selecting the rotor parts (PMs and rotor solid tube) as solid conductor regions with their corresponding conductivities with the possibility of including the effect of temperature. However, in the 2D FEM, the end effect is not directly included, which usually leads to higher estimated losses caused by the eddy currents [132].

3.4 Machine performance

The 24-slot 20-pole TCW PMSM is analyzed at different stator tooth inner widths b_{ds} . The RMS back-EMF at the rated speed and the RMS stator current in the rated load condition as a function of stator tooth inner width b_{ds} are presented in Figure 3.4. As can be seen in the figure, the RMS back-EMF increases until $b_{\text{ds}} = 23$ mm and then begins to decrease, whereas the behavior of the RMS stator current is the opposite. This behavior makes sense because the torque is kept constant and therefore, it is proportional to the product $E_{\text{ph}}I_{\text{s}}$.

Figure 3.5 shows the machine loss distribution and efficiency in the rated load condition as a function of the value of b_{ds} . When analyzing Figures 3.4 and 3.5, it is possible to conclude that it is not advisable to choose values higher than 23 mm for b_{ds} because machine losses begin to increase. However, there is no drastic efficiency drop caused by the low value of rotor losses as shown in Figure 3.5. Note that the rotor losses increase as the value of b_{ds} increases. This is explained by the harmful harmonic current linkage ($v = 1$), which increases as the value of b_{ds} increases. The copper losses and the stator core losses have a significant impact on the total machine losses. Winding losses are unavoidable because of the characteristics of the copper conductor used, and the stator iron losses depend on the magnetic properties of the core material. Table 3.1 shows a

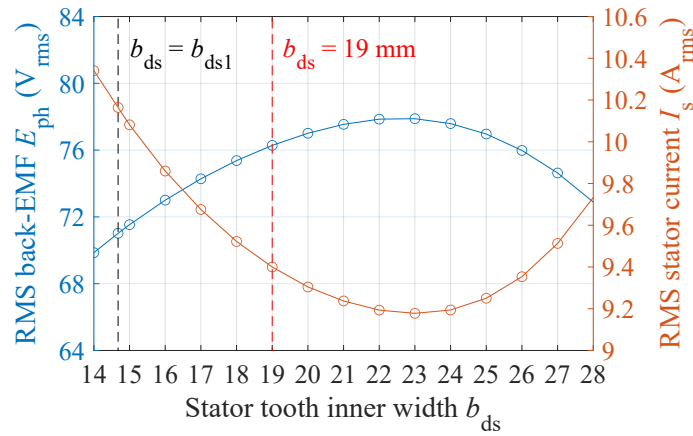


Figure 3.4: RMS back-EMF at the rated speed ($n_N = 80$ r/min) and RMS stator current value at the rated load ($T_N = 202$ Nm, $n_N = 80$ r/min) as a function of the stator tooth inner width b_{ds} .

comparison of the characteristics between the 430SS material (applied as 1 mm sheets) and traditional electrical steel, e.g. M400-50A, and Figure 3.6 shows their magnetization curves [133]. As it can be observed in Figure 3.6, the coercive force of the 430SS is 14 times that of electrical steel, leading to a large hysteresis loop area. As mentioned in the introduction of this doctoral dissertation, this is explained by the chemical composition of the 430SS. Unfortunately, this leads to the fact that the most important source of stator core losses is the hysteresis loss. The resistivity of the 430SS is higher than that of electrical steel, which does not allow significant eddy-current losses.

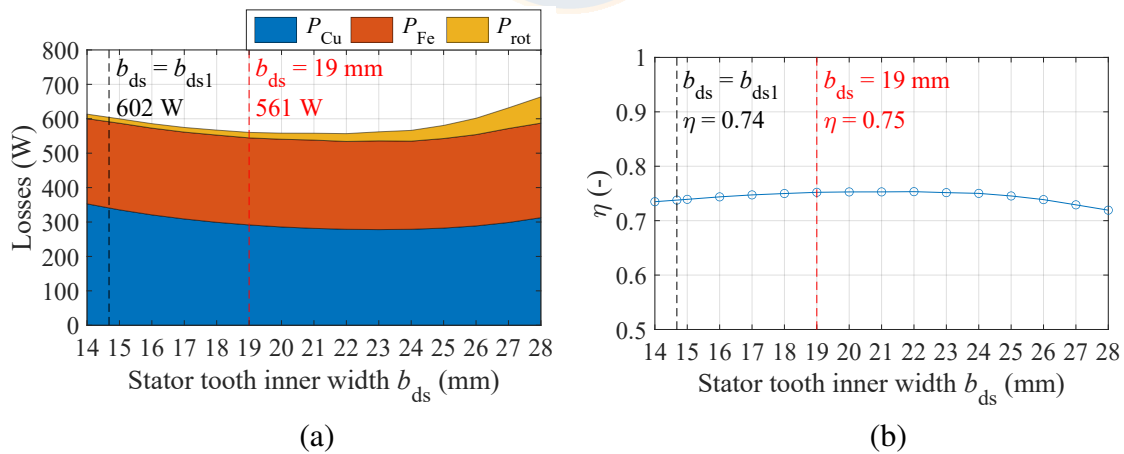


Figure 3.5: (a) Losses and (b) efficiency at the rated load as a function of the stator tooth inner width b_{ds} , where P_{Cu} are the copper losses, P_{Fe} are the laminated stator iron losses, and P_{rot} are the eddy-current losses in the solid rotor.

Table 3.2 shows the electromagnetic losses of the machine for $b_{ds} = b_{ds1}$ and $b_{ds} = 19$ mm. As shown in the table, the hysteresis losses in the no-load condition are high, and when compared in the load condition, an increase of approximately 5 to

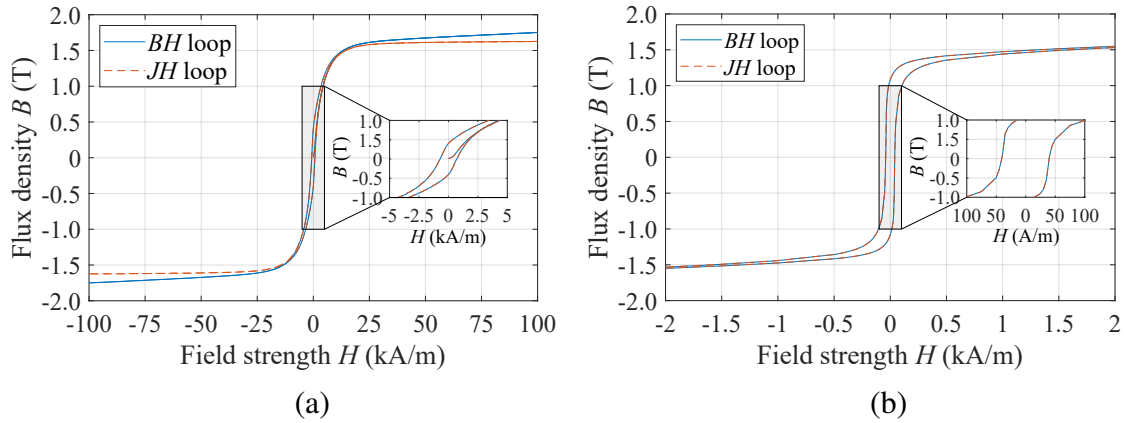


Figure 3.6: Magnetization curves of (a) 430SS and (b) M400-50A.

Table 3.1: Manufacturer data of the stator core materials.

Parameter	430SS	M400-50A
Flux density at 20 kA/m field strength (T)	1.58	2.00
Coercivity H_c (A/m)	708	50
Electrical resistivity ρ ($\mu\Omega\text{m}$)	60	42
Lamination thickness d (mm)	1.0	0.5
Density ρ (kg/m^3)	7750	7700

6% can be seen. This means that the magnetic field produced by the PMs mainly affects the hysteresis losses. Table 3.3 presents the hysteresis torque values for $b_{ds} = b_{ds1}$ and $b_{ds} = 19$ mm. As can be deduced, this corresponds to approximately 15% of the rated torque in all cases, which is high. The stator eddy-current losses, instead, are low. The PM eddy-current losses are too low because of the high electrical resistivity of the magnet and the extra low speed of the machine, which have little impact on the machine performance. It should be noted that there is a significant difference between the rotor losses in the no-load and load conditions. This is mainly explained by the armature reaction effect.

Figure 3.7 presents the core loss density for $b_{ds} = b_{ds1}$ and $b_{ds} = 19$ mm. As illustrated in the figure, the losses are highest in the wound teeth, but this area corresponds only to 1/4 of the stator region. Despite this, the core losses will remain high owing to the magnetic characteristics of the chosen material as shown in Table 3.2.

Table 3.2: No-load and rated load electromagnetic losses for $b_{ds} = b_{ds1}$ and $b_{ds} = 19$ mm.

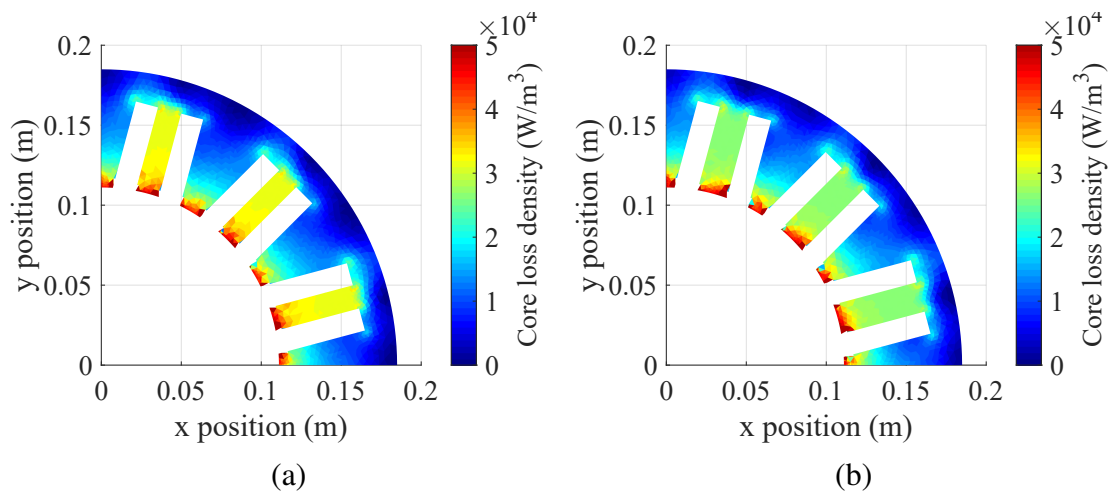
Parameter	$b_{ds} = b_{ds1}$	$b_{ds} = 19$ mm
Stator hysteresis loss ¹ (W)	234.1	235.3
Stator eddy-current loss ¹ (W)	3.6	3.5
Rotor losses ¹ (W)	1.9	2.6
PM eddy-current loss ¹ (W)	0.54	0.55
Stator winding losses ² (W)	342.0	291.0
Stator hysteresis loss ² (W)	247.9	249.2
Stator eddy-current loss ² (W)	3.8	3.7
Rotor losses ² (W)	13.0	16.0
PM eddy-current loss ² (W)	0.59	0.59

¹ $I_s = 0$ A_{rms}, 80 r/min

² $I_s = I_{sN}$, 80 r/min

Table 3.3: Stator hysteresis torque for $b_{ds} = b_{ds1}$ and $b_{ds} = 19$ mm.

Condition	$b_{ds} = b_{ds1}$	$b_{ds} = 19$ mm
$I_s = 0$ A _{rms} , $n = 80$ r/min	27.9 Nm	28.1 Nm
$I_s = I_{sN}$, $n = 80$ r/min	29.6 Nm	29.7 Nm

Figure 3.7: Core loss density distribution at the rated load for (a) $b_{ds} = b_{ds1}$ and (b) $b_{ds} = 19$ mm.

3.5 Summary

This chapter has presented an analysis of the performance when using unequal teeth widths. As described, the primary sources of machine losses are copper losses and stator core losses. The latter are due to the magnetic properties of the material used. The rotor losses, instead, are low compared with the stator losses and the copper and iron losses. They are mainly affected by the winding configuration used. This can be verified by the current linkage harmonics by varying the width of the tooth as discussed in Chapter II. Note that by varying the tooth width, the stator core losses are not significantly affected. However, the winding Joule losses are reduced because of the increase in the winding factor.



4 Prototype and measurements

4.1 Prototype manufacture description

The submersible PMSM was manufactured according to the application requirements specified in the introduction.

Figure 4.1 presents a view of the rotor parts of the machine. The rotor core was constructed from a solid S355 tube, and each magnet block per pole was axially divided into four segments. To eliminate the 6th-order harmonic of the cogging torque caused by the stator asymmetry, a two-step rotor skewing with a shift of 3° between the magnets was adopted. Therefore, by combining the rotor core structure and the division of the PMs, the rotor was easy to manufacture. The PMs were fixed in the rotor core surface, and then, the preformed fiberglass cover and the flanges were installed. The voids were filled with epoxy resin. Figure 4.2 shows the rotor assembled.

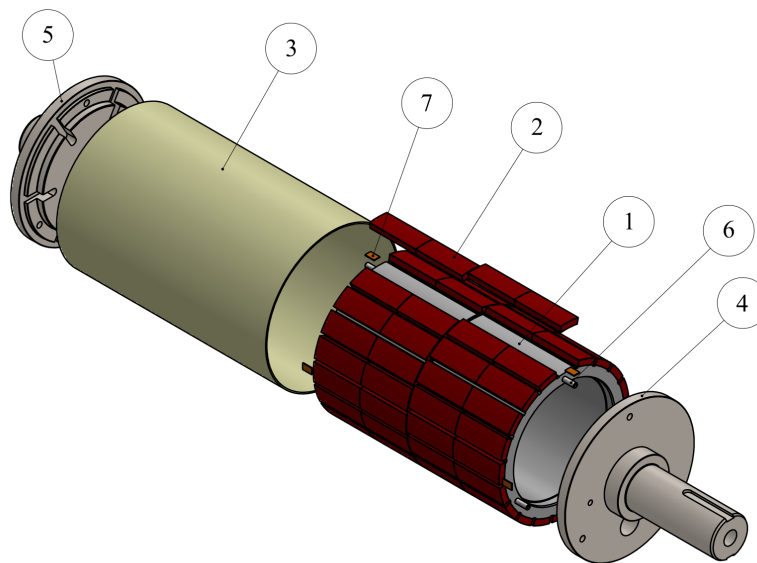


Figure 4.1: Exploded view of the rotor assembly: (1) tube, (2) PM, (3) cover, (4) drive end ring, (5) non-drive rotor end ring, (6) ring attachment screw bolts, and (7) wedge to center the fiberglass tube.

The stator core was made of 1-mm-thick 430SS sheets, as shown in Figure 4.3. Insulation between sheets was provided by a layer of epoxy glue between the sheets when the stack was formed. As shown in Figure 4.3, the stator slots are open, facilitating easy mounting of preformed coils. The insulated conductor material (cable) used in the coils was PVC-coated solid copper wire. The external diameter of the cable is 3.1 mm, and the diameter of the round copper wire is 2.0 mm (the copper cross-sectional area is 3.14 mm²). The rated operating voltage of the cable is 690 V at



Figure 4.2: Canned rotor of the prototype.

the maximum temperature of 60 °C [134]. The cable arrangement in the stator slot is shown in Figure 4.4a. The PVC insulation layer of the cable is relatively soft and can be easily deformed or cut when contacting with sharp objects. Thus, the use of preformed coils is advisable to guarantee the integrity of the coil insulation during its assembly in the stator slots. To ensure that there is enough space in the stator slot for the preformed coil, a 3D printed plastic model of the machine part was built, as presented in Figure 4.4b. The stator assembled is shown in Figure 4.5.

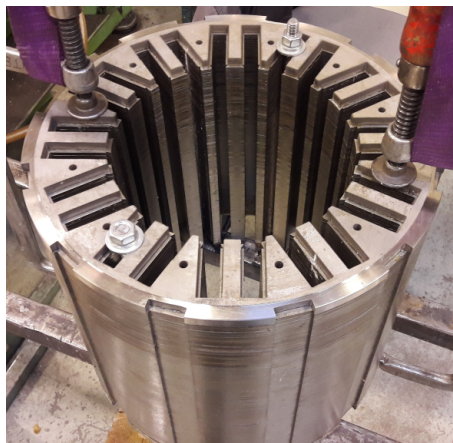


Figure 4.3: Stator stack laminations of the prototype.

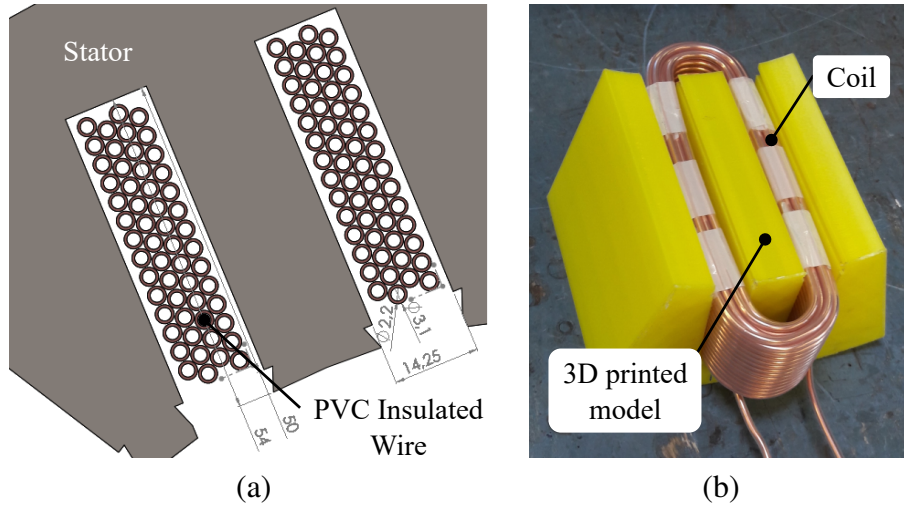


Figure 4.4: (a) Cable positions of one complete coil in the stator slots and (b) 3D printed model of part of the stator core with the coil inserted.



Figure 4.5: Prototype stator assembled. Glass-fibre slot keys guarantee the fixing of the coils. No impregnation was used for the winding.

4.2 Description of the test bench

The schematic and a photograph of the test bench are displayed in Figure 4.6. The prototype is coupled to an IM, which acts as a dynamometer. The IM and prototype are supplied by ABB ACS611 and ACS355 drives, respectively. An ACS355 converter is connected to an ACC611 converter through the DC link, and the grid feeds the latter. With this configuration, the grid only supplies the system losses to keep it operating. The layout of the test bench is vertical according to the requirements of the application. The measurement of torque and speed was performed with a Magtrol torque transducer coupled between the two machines. The current and voltage measurements in the prototype were carried out with a power analyzer (Yokogawa PZ4000).

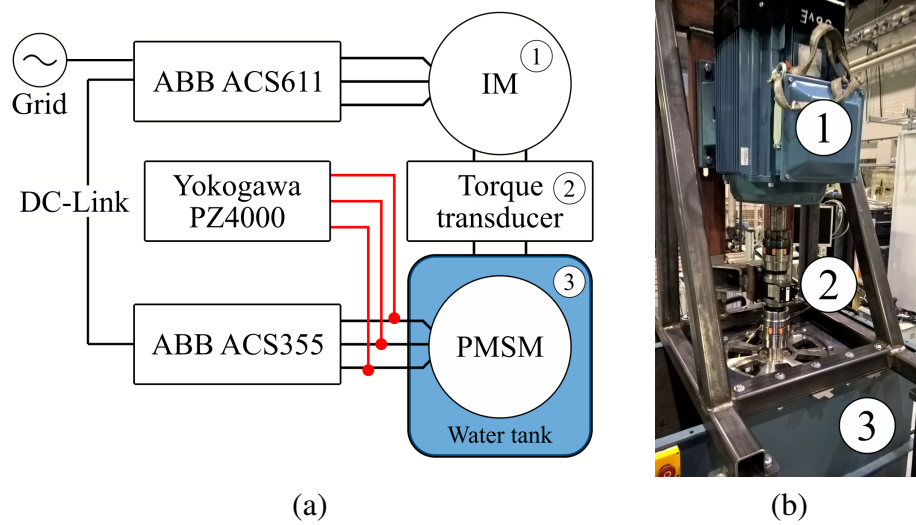


Figure 4.6: (a) Schematic and (b) photograph of the experimental setup. The numbers shown in the photograph denote the component indicated in the schematic.

The prototype was immersed in a container with water flowing at room temperature to observe the behavior of the machine in operation.

4.3 Prototype measurements

Initially, the prototype was driven by the IM at no load. Because of the unorthodox stator material, there is a constant resistive torque caused by hysteresis losses at any speed. The value of this obtained constant no-load torque was approximately 30 Nm, corresponding well to the sum of the stator static hysteresis torque and the friction torque. Therefore, the no-load loss of the machine as generator at the rated speed is approximately 251 W.

Furthermore, the line-to-line back-EMF was measured at the rated speed ($n_N = 80$ r/min), and it was compared with the simulated waveform, as depicted in Figure 4.7. The results show that the error (peak-to-peak voltage) between the FEA and the experimental test is around 4%, which is tolerable.

The machine prototype was tested at different levels of load and speed with the $i_d = 0$ control. A comparison between the computed and measured mechanical torque at the rated speed for different RMS stator currents is presented in Figure 4.8. As can be seen, there is a good agreement between the experimental and the FEA results. The efficiency map (constant-torque region) was obtained and compared with the simulation results, as presented in Figure 4.9. Note that the behavior of both maps is similar. The maximum value of efficiency is reached when the machine operates at its rated point. Table 4.1 exhibits the distribution of machine losses in this condition. The efficiency can be considered somewhat low, resulting from the very low operating speed,

high hysteresis loss, and copper loss. These losses comprise a significant proportion of the total losses.

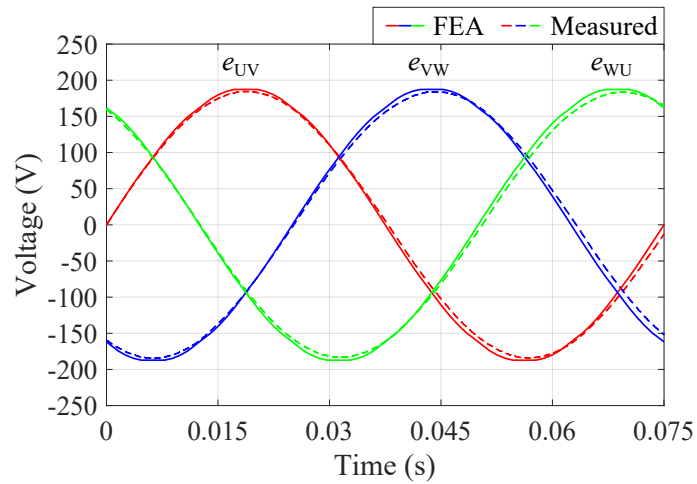


Figure 4.7: Comparison of the simulated and measured line-to-line back-EMF waveforms at the rated speed.

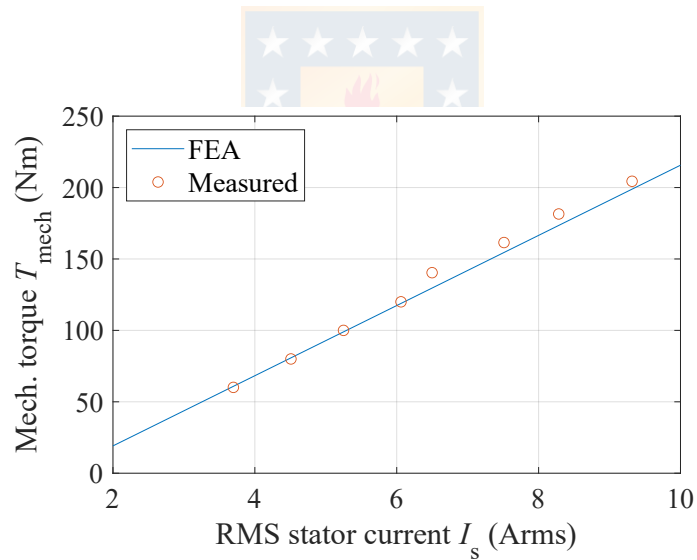


Figure 4.8: Simulated and measured mechanical torque at the rated speed as a function of RMS stator current.

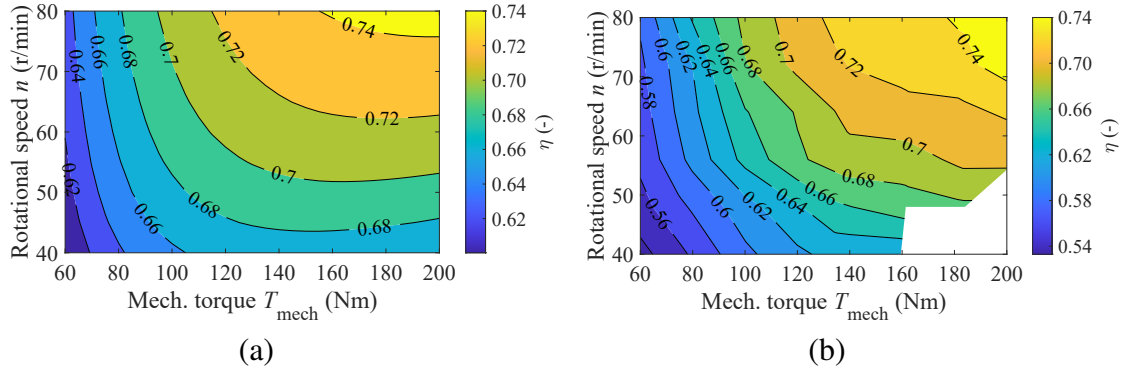


Figure 4.9: (a) Simulated and (b) measured efficiency maps.

Table 4.1: Machine losses at the rated point.

Parameter	Calculated	Measured
Copper losses (W)	291.0	291.0
Stator hysteresis losses (W)	252.9	-
Stator eddy-current losses (W)	3.7	-
Rotor losses (W)	16.0	-
PM losses (W)	0.59	-
Friction + additional losses (W)	34.0	-
Total losses (W)	594.4	592.0
Efficiency (-)	0.74	0.74

4.4 Summary

This chapter has presented some details of the manufacture of the submersible PMSM and the verification of the FEA results with experimental results. The machine was manufactured with the proposed materials, and contributions to its manufacture from the engineering point of view were presented.

The prototype was tested on a test bench inside a water tank to test its functionality, and measurements were carried out. It was found that its maximum efficiency in the operating range was 74%, with a good agreement with the FEA results. The back-EMF and losses computed with the FEA have a good agreement with the experimental tests; therefore, the asymmetry of the stator used and the method to calculate the iron losses proposed in this doctoral dissertation are validated.

5 Conclusion

The objective of this doctoral dissertation was to analyze the most important parameters that influence a submersible TCW PMSM manufactured of unorthodox stainless stator materials and with unequal stator teeth widths.

This work shows that the TCW PMSM with unequal teeth widths provides useful performance advantages in the case of a single-layer winding. The first advantage of this stator asymmetry is the increase in the back-EMF and the electromagnetic torque obtained by varying the width of the stator teeth that carry a coil. It is achieved by increasing the winding factor that depends on the coil pitch. The obtained back-EMF waveform is symmetrical, and the mutual coupling between phases remains unchanged. Therefore, the asymmetries in the single-layer-winding stator can be used without a significant effect on other machine characteristics. However, depending on the slot geometry, the torque quality can be affected by the appearance of undesirable torque harmonics that require the use of cogging torque minimization techniques, which, however, typically have to be used also in symmetrical teeth arrangements. Furthermore, this asymmetry is subject to limitations: the slot–pole combination, the number of winding layers, and dimensions. The most feasible case to achieve the maximum winding factor is a single-layer winding with a number of poles close to the number of slots, e.g., $2p = Q_s \pm 2$. Moreover, to achieve a higher back-EMF value and a higher electromagnetic torque and to avoid cogging torque, the slot opening width should be typically semi-closed with an optimized width. Naturally, the semi-closed slot arrangement complicates the manufacture of the machine and the use of preformed coils.

The use of unequal teeth widths in the machine under study increases the back-EMF—and the torque—by approximately 8% compared with the symmetrical stator; thus, at the rated torque, the copper losses are reduced by 15% as a result of the reduction in the stator current. Moreover, these improvements were achieved without altering the size of the machine.

The development of a 2D analytical model of the TCW PMSM with unequal teeth widths was presented in this work. It was compared with the 2D FEM, and a good agreement was reached. Furthermore, this model can be used for a fast TCW PMSM design with unequal tooth widths.

This work presented a stainless-core submersible PMSM. The stator core made of ferritic stainless steel proved to be functional in the submersible application and can be considered an alternative to traditional electrical steels in special cases. However, the high coercivity of the stainless steel material produces significant hysteresis torque and losses. A potential ferritic stainless steel with an acceptably low coercivity can resolve this drawback, having the area of the hysteresis loop as small as possible (less energy loss). This type of material would be very attractive for electrical machines operated in

harsh environments. From the analysis of the chemical composition of stainless steels carried out in this doctoral dissertation, 409 and 410 stainless steels can be potential materials with a low coercive force (~ 500 A/m) and high flux density saturation (~ 1.7 T).

A nonconventional method to calculate the hysteresis loss in a rotating electrical machine was implemented. According to the experimental results, there is a good agreement with the obtained results. The hysteresis model used in this doctoral dissertation is the Jiles–Atherton method. The model enables the calculation of minor and major hysteresis loops based on five parameters calculated from the hysteresis curves of the material. The main problem with this method is the accuracy of numerical integration and solving of the ordinary differential equations. The next step is to use a reliable equation-free hysteresis model.

The immersion of the wet machine in water where the water penetrates even into the electromagnetic active elements can improve the thermal characteristics of the machine, which can increase its load capacity and useful lifetime. In this machine, the water flows through the air gap; thus, the fluid is confined between the rotor and the stator. This means that turbulent Taylor vortices could occur. Therefore, friction losses caused by the water and the rotor will be produced. In this work, these losses were neglected because of the low speed of the machine. However, it is recommended to study this phenomenon in medium- to high-speed machines, and also its impacts on the thermal characteristics of the machine should be investigated.

The submersible machine under study was manufactured and tested in a water tank. The water was flowing in the tank, and its temperature was kept constant at about the ambient temperature. The test bench was designed according to the requirements of the application, and the measurements show a good agreement with the FEA results. Furthermore, the machine has been operating since 2018 in a submersible application for which it was designed, thus proving it to be functional.

References

- [1] P. Oxley, J. Goodell, and R. Molt, “Magnetic properties of stainless steels at room and cryogenic temperatures,” *Journal of Magnetism and Magnetic Materials*, vol. 321, no. 14, pp. 2107–2114, 2009.
- [2] P. Waide and C. U. Brunner, “Energy-Efficiency Policy Opportunities for Electric Motor-Driven Systems,” *IEA Energy Papers*, no. 7, 2011. [Online]. Available: <https://www.oecd-ilibrary.org/content/paper/5kkg52gb9gjd-en>
- [3] H. Ritchie and M. Roser, “Energy,” *Our World in Data*, 2020. [Online]. Available: <https://ourworldindata.org/energy>
- [4] F. J. T. E. Ferreira and A. T. d. Almeida, “Reducing Energy Costs in Electric-Motor-Driven Systems: Savings Through Output Power Reduction and Energy Regeneration,” *IEEE Industry Applications Magazine*, vol. 24, no. 1, pp. 84–97, 2018.
- [5] J. Pyrhönen, V. Hrabovcová, and R. S. Semken, *Electrical Machine Drives Control: An Introduction*. John Wiley & Sons, Ltd, 2016.
- [6] F. J. T. E. Ferreira, G. Baoming, and A. T. d. Almeida, “Reliability and Operation of High-Efficiency Induction Motors,” *IEEE Transactions on Industry Applications*, vol. 52, no. 6, pp. 4628–4637, 2016.
- [7] R. Rajabi Moghaddam, “Synchronous Reluctance Machine (SynRM) in Variable Speed Drives (VSD) Applications,” PhD Thesis, KTH, Electrical Machines and Power Electronics, 2011.
- [8] J. Pyrhönen, T. Jokinen, and V. Hrabovcová, *Design of Rotating Electrical Machines, 2nd Edition*. John Wiley & Sons, Ltd, 2014.
- [9] M. A. Rahman, “History of Interior Permanent Magnet Motors,” *IEEE Industry Applications Magazine*, vol. 19, no. 1, pp. 10–15, 2013.
- [10] R. McCallum, L. Lewis, R. Skomski, M. Kramer, and I. Anderson, “Practical Aspects of Modern and Future Permanent Magnets,” *Annual Review of Materials Research*, vol. 44, no. 1, pp. 451–477, 2014.
- [11] P. Sekerak, V. Hrabovcova, J. Pyrhönen, L. Kalamen, P. Rafajdus, and M. Onufer, “Comparison of Synchronous Motors With Different Permanent Magnet and Winding Types,” *IEEE Transactions on Magnetics*, vol. 49, no. 3, pp. 1256–1263, 2013.
- [12] I. Petrov and J. Pyrhönen, “Performance of Low-Cost Permanent Magnet Material in PM Synchronous Machines,” *IEEE Transactions on Industrial Electronics*, vol. 60, no. 6, pp. 2131–2138, 2013.

- [13] I. Petrov, M. Niemelä, P. Ponomarev, and J. Pyrhönen, "Rotor Surface Ferrite Permanent Magnets in Electrical Machines: Advantages and Limitations," *IEEE Transactions on Industrial Electronics*, vol. 64, no. 7, pp. 5314–5322, 2017.
- [14] O. Keysan, A. S. McDonald, and M. Mueller, "A Direct Drive Permanent Magnet Generator Design for a Tidal Current Turbine (SeaGen)," in *2011 IEEE International Electric Machines Drives Conference (IEMDC)*, pp. 224–229, 2011.
- [15] A. D. Gerlando, G. Foglia, M. F. Iacchetti, and R. Perini, "Axial Flux PM Machines With Concentrated Armature Windings: Design Analysis and Test Validation of Wind Energy Generators," *IEEE Transactions on Industrial Electronics*, vol. 58, no. 9, pp. 3795–3805, 2011.
- [16] J. Nerg, M. Rilla, V. Ruuskanen, J. Pyrhönen, and S. Ruotsalainen, "Direct-Driven Interior Magnet Permanent-Magnet Synchronous Motors for a Full Electric Sports Car," *IEEE Transactions on Industrial Electronics*, vol. 61, no. 8, pp. 4286–4294, 2014.
- [17] P. Lindh, J. Montonen, P. Immonen, J. A. Tapia, and J. Pyrhönen, "Design of a Traction Motor With Tooth-Coil Windings and Embedded Magnets," *IEEE Transactions on Industrial Electronics*, vol. 61, no. 8, pp. 4306–4314, 2014.
- [18] P. Lindh, I. Petrov, P. Immonen, J. Pyrhönen, M. Niemelä, J. Anttila, M. Paakkinen, and E. Scherman, "Performance of a Direct-Liquid-Cooled Motor in an Electric Bus Under Different Load Cycles," *IEEE Access*, vol. 7, pp. 86 897–86 905, 2019.
- [19] K. T. Chau, C. C. Chan, and C. Liu, "Overview of Permanent-Magnet Brushless Drives for Electric and Hybrid Electric Vehicles," *IEEE Transactions on Industrial Electronics*, vol. 55, no. 6, pp. 2246–2257, 2008.
- [20] M. J. Melfi, S. Evon, and R. McElveen, "Induction Versus Permanent Magnet Motors," *IEEE Industry Applications Magazine*, vol. 15, no. 6, pp. 28–35, 2009.
- [21] L. Jian, G. Xu, C. C. Mi, K. T. Chau, and C. C. Chan, "Analytical Method for Magnetic Field Calculation in a Low-Speed Permanent-Magnet Harmonic Machine," *IEEE Transactions on Energy Conversion*, vol. 26, no. 3, pp. 862–870, 2011.
- [22] M. Cheng, W. Hua, J. Zhang, and W. Zhao, "Overview of Stator-Permanent Magnet Brushless Machines," *IEEE Transactions on Industrial Electronics*, vol. 58, no. 11, pp. 5087–5101, 2011.
- [23] A. Boglietti, A. M. El-Refaie, O. Drubel, A. M. Omekanda, N. Bianchi, E. B. Agamloh, M. Popescu, A. D. Gerlando, and J. B. Bartolo, "Electrical Machine Topologies: Hottest Topics in the Electrical Machine Research Community," *IEEE Industrial Electronics Magazine*, vol. 8, no. 2, pp. 18–30, 2014.

- [24] Y. Yang and M. Peng, "A Surface-Mounted Permanent-Magnet Motor With Sinusoidal Pulsewidth-Modulation-Shaped Magnets," *IEEE Transactions on Magnetics*, vol. 55, no. 1, pp. 1–8, 2019.
- [25] F. Meier, "Permanent-Magnet Synchronous Machines with Non-Overlapping Concentrated Windings for Low-Speed Direct-Drive Applications," PhD Thesis, KTH, Electrical Machines and Power Electronics, 2008.
- [26] C. Gerada and K. J. Bradley, "Integrated PM Machine Design for an Aircraft EMA," *IEEE Transactions on Industrial Electronics*, vol. 55, no. 9, pp. 3300–3306, 2008.
- [27] X. Li, K. T. Chau, M. Cheng, B. Kim, and R. D. Lorenz, "Performance Analysis of a Flux-Concentrating Field-Modulated Permanent-Magnet Machine for Direct-Drive Applications," *IEEE Transactions on Magnetics*, vol. 51, no. 5, pp. 1–11, 2015.
- [28] D. McMillan and G. W. Ault, "Techno-Economic Comparison of Operational Aspects for Direct Drive and Gearbox-Driven Wind Turbines," *IEEE Transactions on Energy Conversion*, vol. 25, no. 1, pp. 191–198, 2010.
- [29] F. Blaabjerg, H. Liu, and P. C. Loh, "Marine energy generation systems and related monitoring and control," *IEEE Instrumentation Measurement Magazine*, vol. 17, no. 2, pp. 27–32, 2014.
- [30] S. Benelghali, M. E. H. Benbouzid, and J. F. Charpentier, "Generator Systems for Marine Current Turbine Applications: A Comparative Study," *IEEE Journal of Oceanic Engineering*, vol. 37, no. 3, pp. 554–563, 2012.
- [31] Y. Li, "On the definition of the power coefficient of tidal current turbines and efficiency of tidal current turbine farms," *Renewable Energy*, vol. 68, pp. 868–875, 2014.
- [32] F. Islam, K. Mamun, and M. Amanullah, *Smart Energy Grid Design for Island Countries: Challenges and Opportunities*, ser. Green Energy and Technology. Springer International Publishing, 2017.
- [33] R. Pawlowicz, "Key Physical Variables in the Ocean: Temperature, Salinity, and Density," *Nature Education Knowledge*, vol. 4, no. 4, 2013.
- [34] H. Chen, T. Tang, N. Aït-Ahmed, M. E. H. Benbouzid, M. Machmoum, and M. E. Zaïm, "Attraction, Challenge and Current Status of Marine Current Energy," *IEEE Access*, vol. 6, pp. 12 665–12 685, 2018.
- [35] D. H. Muhsen, T. Khatib, and F. Nagi, "A review of photovoltaic water pumping system designing methods, control strategies and field performance," *Renewable and Sustainable Energy Reviews*, vol. 68, pp. 70–86, 2017.

- [36] V. K. A. Shankar, S. Umashankar, S. Paramasivam, and N. Hanigovszki, "A comprehensive review on energy efficiency enhancement initiatives in centrifugal pumping system," *Applied Energy*, vol. 181, pp. 495–513, 2016.
- [37] T. Marcic, B. Stumberger, and G. Stumberger, "Comparison of Induction Motor and Line-Start IPM Synchronous Motor Performance in a Variable-Speed Drive," *IEEE Transactions on Industry Applications*, vol. 48, no. 6, pp. 2341–2352, 2012.
- [38] T. R. Brinner, R. H. McCoy, and T. Kopecky, "Induction Versus Permanent-Magnet Motors for Electric Submersible Pump Field and Laboratory Comparisons," *IEEE Transactions on Industry Applications*, vol. 50, no. 1, pp. 174–181, 2014.
- [39] G. Pellegrino, A. Vagati, B. Boazzo, and P. Guglielmi, "Comparison of Induction and PM Synchronous Motor Drives for EV Application Including Design Examples," *IEEE Transactions on Industry Applications*, vol. 48, no. 6, pp. 2322–2332, 2012.
- [40] A. T. d. Almeida, F. J. T. E. Ferreira, and G. Baoming, "Beyond Induction Motors-Technology Trends to Move Up Efficiency," *IEEE Transactions on Industry Applications*, vol. 50, no. 3, pp. 2103–2114, 2014.
- [41] M. N. Ibrahim, H. Rezk, M. Al-Dhaifallah, and P. Sergeant, "Solar Array Fed Synchronous Reluctance Motor Driven Water Pump: An Improved Performance Under Partial Shading Conditions," *IEEE Access*, vol. 7, pp. 77 100–77 115, 2019.
- [42] S. Sashidhar and B. G. Fernandes, "A Novel Ferrite SMDS Spoke-Type BLDC Motor for PV Bore-Well Submersible Water Pumps," *IEEE Transactions on Industrial Electronics*, vol. 64, no. 1, pp. 104–114, 2017.
- [43] Q. Yu, S. Chu, W. Li, L. Tian, X. Wang, and Y. Cheng, "Electromagnetic Shielding Analysis of a Canned Permanent Magnet Motor," *IEEE Transactions on Industrial Electronics*, vol. 67, no. 10, pp. 8123–8130, 2020.
- [44] F. Wani, H. Polinder, J. Dong, and A. Yadav, "Comparing Different Materials for Rotor-Can in Flooded Generators," in *2018 XIII International Conference on Electrical Machines (ICEM)*, pp. 2572–2578, 2018.
- [45] M. Cheng, D. Tikang, G. Zhisheng, and C. Dawei, "Novel full through-flow submersible pump," C.N. Patent 201521462U, jul 7, 2019. [Online]. Available: <https://www.google.com/patents/CN201521462U>
- [46] A. Krings, M. Cossale, A. Tenconi, J. Souldard, A. Cavagnino, and A. Boglietti, "Magnetic Materials Used in Electrical Machines: A Comparison and Selection Guide for Early Machine Design," *IEEE Industry Applications Magazine*, vol. 23, no. 6, pp. 21–28, 2017.

- [47] T. Judendorfer, J. Fletcher, N. Hassanain, M. Mueller, and M. Muhr, "Challenges to Machine Windings used in Electrical Generators in Wave and Tidal Power Plants," in *2009 IEEE Conference on Electrical Insulation and Dielectric Phenomena*, pp. 238–241, 2009.
- [48] C. Riba Romeva, *Selección de materiales en el diseño de máquinas*. Edicions UPC, 2008.
- [49] H. M. Cobb, *The History of Stainless Steel*. Materials Park, OH: ASM International, 2010.
- [50] Y. Yu, S. Shironita, K. Souma, and M. Umeda, "Effect of chromium content on the corrosion resistance of ferritic stainless steels in sulfuric acid solution," *Heliyon*, vol. 4, no. 11, p. e00958, 2018.
- [51] A. Krings, A. Boglietti, A. Cavagnino, and S. Sprague, "Soft Magnetic Material Status and Trends in Electric Machines," *IEEE Transactions on Industrial Electronics*, vol. 64, no. 3, pp. 2405–2414, 2017.
- [52] L. Ma, F. Wiame, V. Maurice, and P. Marcus, "Origin of nanoscale heterogeneity in the surface oxide film protecting stainless steel against corrosion," *npj Materials Degradation*, vol. 3, no. 1, Dec. 2019, publisher: Springer Science and Business Media LLC.
- [53] Y. Hayakawa, "Electrical Steels," in *Reference Module in Materials Science and Materials Engineering*. Elsevier, 2020.
- [54] B. Janjic, A. Binder, V. Bischof, and G. Ludwig, "Design of PM integrated motor-drive system for axial pumps," in *2007 European Conference on Power Electronics and Applications*, pp. 1–10, 2007.
- [55] Q. Yu, X. Wang, and Y. Cheng, "Electromagnetic Calculation and Characteristic Analysis of Can Effect of a Canned Permanent Magnet Motor," *IEEE Transactions on Magnetics*, vol. 52, no. 12, pp. 1–6, 2016.
- [56] J. Pyrhönen, J. Nerg, P. Kurronen, J. Puranen, and M. Haavisto, "Permanent Magnet Technology in Wind Power Generators," in *The XIX International Conference on Electrical Machines - ICEM 2010*, pp. 1–6, 2010.
- [57] M. Katter, L. Zapf, R. Blank, W. Fernengel, and W. Rodewald, "Corrosion mechanism of RE-Fe-Co-Cu-Ga-Al-B magnets," *IEEE Transactions on Magnetics*, vol. 37, no. 4, pp. 2474–2476, 2001.
- [58] M. Drak and L. Dobrzanski, "Corrosion of Nd-Fe-B permanent magnets," *Journal of Achievements in Materials and Manufacturing Engineering*, vol. 20, no. 1-2, pp. 239–242, 2007.

- [59] E. Isotahdon, “Corrosion Losses, Mechanisms and Protection Strategies for Sintered Nd-Fe-B Magnets,” PhD Thesis, Tampere University of Technology, 2017.
- [60] Bunting, “Alnico Magnet Coatings,” Accessed Apr. 07, 2021. [Online]. Available: <https://e-magnetsuk.com/alnico-magnets/coatings/>
- [61] Eclipse Magnetics Ltd, “Ferrite Magnets/Ceramic Magnets Datasheet,” Accessed Apr. 07, 2021. [Online]. Available: https://www.eclipsemagnetics.com/site/assets/files/2418/ferrite_ceramic_datasheet.pdf
- [62] Eclipse Magnetics Ltd, “Samarium Cobalt Magnets, SmCo Magnets Datasheet,” Accessed Apr. 07, 2021. [Online]. Available: http://www.eclipsemagnetics.cn/media/wysiwyg/datasheets/magnet_materials_and_assemblies/samarium_cobalt_magnets_datasheet.pdf
- [63] Magnet Expert Ltd, “Corrosion resistance in permanent magnets,” Accessed Apr. 07, 2021. [Online]. Available: <https://www.magnetexpert.com/technical-advice-i685/corrosion-resistance-in-permanent-magnets-i684>
- [64] LORD Corp, “CoolTherm® SC-6711/6732 Silicone Encapsulant,” Accessed Apr. 07, 2021. [Online]. Available: https://files.lord.com/pdf/44/DS3572_CoolThermSC-6711.pdf
- [65] A. Shimamura, Y. Hotta, H. Hyuga, M. Hotta, and K. Hirao, “Improving the thermal conductivity of epoxy composites using a combustion-synthesized aggregated β -Si₃N₄ filler with randomly oriented grains,” *Scientific Reports*, vol. 10, no. 1, p. 14926, Dec. 2020.
- [66] X. J. Li, J. Yang, B. Q. Yan, and X. Zheng, “Insulated Cable Temperature Calculation and Numerical Simulation,” *MATEC Web Conf.*, vol. 175, p. 03014, 2018.
- [67] N. Bianchi, S. Bolognani, and M. D. Pre, “Magnetic Loading of Fractional-Slot Three-Phase PM Motors With Nonoverlapped Coils,” *IEEE Transactions on Industry Applications*, vol. 44, no. 5, pp. 1513–1521, 2008.
- [68] A. M. EL-Refaie, “Fractional-Slot Concentrated-Windings Synchronous Permanent Magnet Machines: Opportunities and Challenges,” *IEEE Transactions on Industrial Electronics*, vol. 57, no. 1, pp. 107–121, 2010.
- [69] A. El-Refaie, “Fractional-Slot Concentrated-Windings: A Paradigm Shift in Electrical Machines,” in *2013 IEEE Workshop on Electrical Machines Design, Control and Diagnosis (WEMDCD)*, pp. 24–32, 2013.

- [70] E. Fornasiero, L. Alberti, N. Bianchi, and S. Bolognani, "Considerations on Selecting Fractional-Slot Nonoverlapped Coil Windings," *IEEE Transactions on Industry Applications*, vol. 49, no. 3, pp. 1316–1324, 2013.
- [71] G. Li, Z. Zhu, M. P. Foster, D. A. Stone, and H. Zhan, "Modular Permanent-Magnet Machines With Alternate Teeth Having Tooth Tips," *IEEE Transactions on Industrial Electronics*, vol. 62, no. 10, pp. 6120–6130, 2015.
- [72] N. J. Baker, D. J. B. Smith, M. C. Kulan, and S. Turvey, "Design and Performance of a Segmented Stator Permanent Magnet Alternator for Aerospace," *IEEE Transactions on Energy Conversion*, vol. 33, no. 1, pp. 40–48, 2018.
- [73] I. Petrov, C. Di, P. Lindh, M. Niemelä, A. Repo, and J. Pyrhönen, "Fault-Tolerant Modular Stator Concentrated Winding Permanent Magnet Machine," *IEEE Access*, vol. 8, pp. 7806–7816, 2020.
- [74] E. Carraro and N. Bianchi, "Design and comparison of interior permanent magnet synchronous motors with non-uniform airgap and conventional rotor for electric vehicle applications," *IET Electric Power Applications*, vol. 8, no. 6, pp. 240–249, Jul. 2014.
- [75] P. Ponomarev, P. Lindh, and J. Pyrhönen, "Effect of Slot-and-Pole Combination on the Leakage Inductance and the Performance of Tooth-Coil Permanent-Magnet Synchronous Machines," *IEEE Transactions on Industrial Electronics*, vol. 60, no. 10, pp. 4310–4317, 2013.
- [76] P. Ponomarev, Y. Alexandrova, I. Petrov, P. Lindh, E. Lomonova, and J. Pyrhönen, "Inductance Calculation of Tooth-Coil Permanent-Magnet Synchronous Machines," *IEEE Transactions on Industrial Electronics*, vol. 61, no. 11, pp. 5966–5973, 2014.
- [77] N. Bianchi, S. Bolognani, and E. Fornasiero, "An Overview of Rotor Losses Determination in Three-Phase Fractional-Slot PM Machines," *IEEE Transactions on Industry Applications*, vol. 46, no. 6, pp. 2338–2345, 2010.
- [78] N. Bianchi, L. Alberti, and M. Barcaro, "Design and Tests of a Four-Layer Fractional-Slot Interior Permanent-Magnet Motor," *IEEE Transactions on Industry Applications*, vol. 52, no. 3, pp. 2234–2240, 2016.
- [79] N. Bianchi, D. Durello, and A. Fasolo, "Relationship Between Rotor Losses and Size of Permanent-Magnet Machines," *IEEE Transactions on Industry Applications*, vol. 49, no. 5, pp. 2015–2023, 2013.
- [80] D. Ishak, Z. Q. Zhu, and D. Howe, "Permanent-Magnet Brushless Machines With Unequal Tooth Widths and Similar Slot and Pole Numbers," *IEEE Transactions on Industry Applications*, vol. 41, no. 2, pp. 584–590, 2005.

- [81] I. Petrov, P. Ponomarev, Y. Alexandrova, and J. Pyrhönen, "Unequal Teeth Widths for Torque Ripple Reduction in Permanent Magnet Synchronous Machines With Fractional-Slot Non-Overlapping Windings," *IEEE Transactions on Magnetics*, vol. 51, no. 2, pp. 1–9, 2015.
- [82] I. Petrov, P. Ponomarev, and J. Pyrhönen, "Asymmetrical Geometries in Electrical Machines," *International Review of Electrical Engineering (IREE)*, vol. 11, no. 1, 2016.
- [83] X. Zeng, L. Quan, X. Zhu, L. Xu, and F. Liu, "Investigation of an Asymmetrical Rotor Hybrid Permanent Magnet Motor for Approaching Maximum Output Torque," *IEEE Transactions on Applied Superconductivity*, vol. 29, no. 2, pp. 1–4, 2019.
- [84] A. Tessarolo, M. Mezzarobba, and N. Barbini, "Improved Four-Layer Winding Design for a 12-Slot 10-Pole Permanent Magnet Machine Using Unequal Tooth Coils," in *IECON 2016 - 42nd Annual Conference of the IEEE Industrial Electronics Society*, pp. 1686–1691, 2016.
- [85] G. J. Li and Z. Q. Zhu, "Analytical Modeling of Modular and Unequal Tooth Width Surface-Mounted Permanent Magnet Machines," *IEEE Transactions on Magnetics*, vol. 51, no. 9, pp. 1–9, 2015.
- [86] A. A. Adly and A. Huzayyin, "The impact of demagnetization on the feasibility of permanent magnet synchronous motors in industry applications," *Journal of Advanced Research*, vol. 17, pp. 103–108, 2019.
- [87] G. Pellegrino, A. Vagati, P. Guglielmi, and B. Boazzo, "Performance Comparison Between Surface-Mounted and Interior PM Motor Drives for Electric Vehicle Application," *IEEE Transactions on Industrial Electronics*, vol. 59, no. 2, pp. 803–811, 2012.
- [88] L. Chong and M. F. Rahman, "Saliency ratio derivation and optimisation for an interior permanent magnet machine with concentrated windings using finite-element analysis," *IET Electric Power Applications*, vol. 4, no. 4, pp. 249–258(9), Apr. 2010.
- [89] T. Aho, V. Sihvo, J. Nerg, and J. Pyrhönen, "Rotor Materials for Medium-Speed Solid-Rotor Induction Motors," in *Proceedings of IEEE International Electric Machines and Drives Conference, IEMDC 2007*, vol. 1, pp. 525–530, 2007.
- [90] X. Chen, J. Hu, K. Chen, and Z. Peng, "Modeling of electromagnetic torque considering saturation and magnetic field harmonics in permanent magnet synchronous motor for HEV," *Simulation Modelling Practice and Theory*, vol. 66, pp. 212–225, 2016.

- [91] S. G. Min, G. Bramerdorfer, and B. Sarlioglu, "Analytical Modeling and Optimization for Electromagnetic Performances of Fractional-Slot PM Brushless Machines," *IEEE Transactions on Industrial Electronics*, vol. 65, no. 5, 2018.
- [92] A. M. EL-Refaie and T. M. Jahns, "Optimal Flux Weakening in Surface PM Machines Using Fractional-Slot Concentrated Windings," *IEEE Transactions on Industry Applications*, vol. 41, no. 3, 2005.
- [93] E. Carraro, N. Bianchi, S. Zhang, and M. Koch, "Design and Performance Comparison of Fractional Slot Concentrated Winding Spoke Type Synchronous Motors With Different Slot-Pole Combinations," *IEEE Transactions on Industry Applications*, vol. 54, no. 3, pp. 2276–2284, 2018.
- [94] W. Jara, "Axial Flux Permanent Magnet Machines - Development of Optimal Design Strategies," PhD Thesis, Lappeenranta University of Technology LUT, 2016.
- [95] Z. Q. Zhu and D. Howe, "Instantaneous Magnetic Field Distribution in Brushless Permanent Magnet DC Motors, Part III: Effect of stator slotting," *IEEE Transactions on Magnetics*, vol. 29, no. 1, pp. 143–151, 1993.
- [96] H. Mahmoud, N. Bianchi, G. Bacco, and N. Chiodetto, "Nonlinear Analytical Computation of the Magnetic Field in Reluctance Synchronous Machines," *IEEE Transactions on Industry Applications*, vol. 53, no. 6, pp. 5373–5382, 2017.
- [97] C. Madariaga, W. Jara, J. Tapia, J. Riedemann, G. Bramerdorfer, P. Castro, and B. Sarlioglu, "Analytical Model and Sensitivity Analysis of Tooth-Coil-Winding Permanent Magnet Synchronous Machine with Modular U-Shape Stator," in *2019 IEEE Energy Conversion Congress and Exposition (ECCE)*, pp. 1761–1768, 2019.
- [98] M. Choi and B. Kim, "Calculation of PM Vernier Motors Using an Improved Air-Gap Permeance Function," *IEEE Transactions on Magnetics*, vol. 55, no. 6, pp. 1–5, 2019.
- [99] D. Zarko, D. Ban, and T. A. Lipo, "Analytical Calculation of Magnetic Field Distribution in the Slotted Air Gap of a Surface Permanent-Magnet Motor Using Complex Relative Air-Gap Permeance," *IEEE Transactions on Magnetics*, vol. 42, no. 7, pp. 1828–1837, 2006.
- [100] T. A. Driscoll, "Schwarz-Christoffel Toolbox User's Guide: Version 2.3," University of Delaware, Newark, DE 19716, Tech. Rep., 2005. [Online]. Available: <http://www.math.udel.edu/~driscoll/SC/guide.pdf>
- [101] T. C. O'Connell and P. T. Krein, "A Schwarz–Christoffel-Based Analytical Method for Electric Machine Field Analysis," *IEEE Transactions on Energy Conversion*, vol. 24, no. 3, pp. 565–577, 2009.

- [102] K. Abbaszadeh and F. R. Alam, "On-Load Field Component Separation in Surface-Mounted Permanent-Magnet Motors Using an Improved Conformal Mapping Method," *IEEE Transactions on Magnetics*, vol. 52, no. 2, pp. 1–12, 2016.
- [103] C. Tang, M. Shen, Y. Fang, and P.-D. Pfister, "Comparison of Subdomain, Complex Permeance, and Relative Permeance Models for a Wide Family of Permanent-Magnet Machines," *IEEE Transactions on Magnetics*, vol. 57, no. 2, pp. 1–5, 2021.
- [104] Z. Q. Zhu, D. Howe, and C. C. Chan, "Improved Analytical Model for Predicting the Magnetic Field Distribution in Brushless Permanent-Magnet Machines," *IEEE Transactions on Magnetics*, vol. 38, no. 1, pp. 229–238, 2002.
- [105] S. G. Min and B. Sarlioglu, "Analytical Calculation of Back EMF Waveform for Linear PM Motors in Slotted and Slotless Structures," *IEEE Transactions on Magnetics*, vol. 53, no. 12, pp. 1–10, 2017.
- [106] J. A. Tapia, J. Pyrhönen, J. Puranen, P. Lindh, and S. Nyman, "Optimal Design of Large Permanent Magnet Synchronous Generators," *IEEE Transactions on Magnetics*, vol. 49, no. 1, pp. 642–650, 2013.
- [107] N. Bianchi and M. Dai Pré, "Use of the star of slots in designing fractional-slot single-layer synchronous motors," *IEE Proceedings: Electric Power Applications*, vol. 153, no. 3, pp. 459–466, 2006.
- [108] I. Abdennadher and A. Masmoudi, "Star of slots-based graphical assessment of the back-EMF of fractional-slot PM synchronous machines," in *10th International Multi-Conferences on Systems, Signals Devices 2013 (SSD13)*, pp. 1–8, 2013.
- [109] Z. Q. Zhu and D. Howe, "Instantaneous Magnetic Field Distribution in Brushless Permanent Magnet DC Motors, Part II: Armature-Reaction Field," *IEEE Transactions on Magnetics*, vol. 29, no. 1, pp. 136–142, 1993.
- [110] C. Ma, Q. Li, H. Lu, Y. Liu, and H. Gao, "Analytical model for armature reaction of outer rotor brushless permanent magnet DC motor," *IET Electric Power Applications*, vol. 12, no. 5, pp. 651–657, 2018.
- [111] P. Ponomarev, I. Petrov, and J. Pyrhönen, "Influence of Travelling Current Linkage Harmonics on Inductance Variation, Torque Ripple and Sensorless Capability of Tooth-Coil Permanent-Magnet Synchronous Machines," *IEEE Transactions on Magnetics*, vol. 50, no. 1, pp. 1–8, 2014.
- [112] P. Ponomarev, "Tooth-Coil Permanent Magnet Synchronous Machine Design for Special Applications," PhD Thesis, Lappeenranta University of Technology LUT, 2013.

- [113] J. Montonen, “Integrated hub gear motor for heavy-duty off-road working machines - interdisciplinary design,” PhD Thesis, Lappeenranta University of Technology LUT, 2017.
- [114] C. Madariaga, W. Jara, J. A. Tapia, J. Pyrhönen, P. Lindh, and J. A. Riedemann, “Closed-Form Solution for the Slot Leakage Inductance of Tooth-Coil-Winding Permanent Magnet Machines,” *IEEE Transactions on Energy Conversion*, vol. 34, no. 3, pp. 1572–1580, 2019.
- [115] P. Ponomarev and J. Pyrhönen, “Current Linkage Harmonics and Air-Gap Harmonic Leakage Inductance of Tooth Coil Permanent-Magnet Synchronous Machines,” in *IECON 2013 - 39th Annual Conference of the IEEE Industrial Electronics Society*, pp. 2703–2708, 2013.
- [116] L. Zhu, S. Z. Jiang, Z. Q. Zhu, and C. C. Chan, “Analytical Methods for Minimizing Cogging Torque in Permanent-Magnet Machines,” *IEEE Transactions on Magnetics*, vol. 45, no. 4, pp. 2023–2031, 2009.
- [117] Z. Goryca, S. Różowicz, A. Różowicz, A. Pakosz, M. Leško, and H. Wachta, “Impact of Selected Methods of Cogging Torque Reduction in Multipolar Permanent-Magnet Machines,” *Energies*, vol. 13, no. 22, 2020.
- [118] D. Zarko, D. Ban, and T. A. Lipo, “Analytical Solution for Electromagnetic Torque in Surface Permanent-Magnet Motors Using Conformal Mapping,” *IEEE Transactions on Magnetics*, vol. 45, no. 7, pp. 2943–2954, 2009.
- [119] X. Ge, Z. Q. Zhu, G. Kemp, D. Moule, and C. Williams, “Optimal Step-Skew Methods for Cogging Torque Reduction Accounting for Three-Dimensional Effect of Interior Permanent Magnet Machines,” *IEEE Transactions on Energy Conversion*, vol. 32, no. 1, pp. 222–232, 2017.
- [120] A. M. El-Refaie, T. M. Jahns, and D. W. Novotny, “Analysis of Surface Permanent Magnet Machines With Fractional-Slot Concentrated Windings,” *IEEE Transactions on Energy Conversion*, vol. 21, no. 1, pp. 34–43, 2006.
- [121] I. Petrov, M. Polikarpova, P. Ponomarev, P. Lindh, and J. Pyrhönen, “Investigation of Additional AC Losses in Tooth-Coil Winding PMSM With High Electrical Frequency,” in *2016 XXII International Conference on Electrical Machines (ICEM)*, pp. 1841–1846, 2016.
- [122] A. Krings and J. Soulard, “Overview and Comparison of Iron Loss Models for Electrical Machines,” *Journal of Electrical Engineering*, vol. 10, no. 3, pp. 162–169, 2010, publisher: KTH, Electrical Energy Conversion.
- [123] D. M. Ionel, M. Popescu, M. I. McGilp, T. J. E. Miller, S. J. Dellinger, and R. J. Heideman, “Computation of Core Losses in Electrical Machines Using Improved

- Models for Laminated Steel,” *IEEE Transactions on Industry Applications*, vol. 43, no. 6, pp. 1554–1564, 2007.
- [124] G. Novak, J. Kokošar, A. Nagode, and D. S. Petrovič, “Core-Loss Prediction for Non-Oriented Electrical Steels Based on the Steinmetz Equation Using Fixed Coefficients With a Wide Frequency Range of Validity,” *IEEE Transactions on Magnetics*, vol. 51, no. 4, pp. 1–7, 2015.
- [125] D. Lin, P. Zhou, W. N. Fu, Z. Badics, and Z. J. Cendes, “A Dynamic Core Loss Model for Soft Ferromagnetic and Power Ferrite Materials in Transient Finite Element Analysis,” *IEEE Transactions on Magnetics*, vol. 40, no. 2, pp. 1318–1321, 2004.
- [126] D. Kowal, P. Sergeant, L. Dupré, and L. Vandenbossche, “Comparison of Iron Loss Models for Electrical Machines With Different Frequency Domain and Time Domain Methods for Excess Loss Prediction,” *IEEE Transactions on Magnetics*, vol. 51, no. 1, pp. 1–10, 2015.
- [127] R. Du and P. Robertson, “Dynamic Jiles–Atherton Model for Determining the Magnetic Power Loss at High Frequency in Permanent Magnet Machines,” *IEEE Transactions on Magnetics*, vol. 51, no. 6, pp. 1–10, 2015.
- [128] S. Hussain and D. A. Lowther, “The Modified Jiles–Atherton Model for the Accurate Prediction of Iron Losses,” *IEEE Transactions on Magnetics*, vol. 53, no. 6, pp. 1–4, 2017.
- [129] J. Lee, Y. Kim, S. Rhyu, I. Jung, S. Chai, and J. Hong, “Hysteresis Torque Analysis of Permanent Magnet Motors Using Preisach Model,” *IEEE Transactions on Magnetics*, vol. 48, no. 2, pp. 935–938, 2012.
- [130] S. Hwang, M. Lim, and J. Hong, “Hysteresis Torque Estimation Method Based on Iron-Loss Analysis for Permanent Magnet Synchronous Motor,” *IEEE Transactions on Magnetics*, vol. 52, no. 7, pp. 1–4, 2016.
- [131] H. V. Xuan, D. Lahaye, H. Polinder, and J. A. Ferreira, “Influence of Stator Slotting on the Performance of Permanent-Magnet Machines With Concentrated Windings,” *IEEE Transactions on Magnetics*, vol. 49, no. 2, pp. 929–938, 2013.
- [132] A. Masmoudi and A. Masmoudi, “3-D Analytical Model With the End Effect Dedicated to the Prediction of PM Eddy-Current Loss in FSPMMs,” *IEEE Transactions on Magnetics*, vol. 51, no. 4, pp. 1–11, 2015.
- [133] Modelica Association, “M400_50a,” Accessed Apr. 13, 2021. [Online]. Available: https://doc.modelica.org/Modelica3.2.3/Resources/helpWSM/Modelica/Modelica.Magnetic.FluxTubes.Material.HysteresisTableData.M400_50A.html

- [134] Norddeutsche Seekabelwerke GmbH & Co. KG. "Plastic-Insulated Winding Wires", Nov, 2001. [Online]. Available: http://stenbacka.swg.kotisivustot.fi/wp-content/uploads/sites/3/2016/07/muovieristetyt_kaamilangat.pdf

